

ABSTRACT

Title of Dissertation: PREDICTING THE MAGNETIC FIELD
 OF THE THREE-METER SPHERICAL
 COUETTE EXPERIMENT

Sarah Cassie Burnett
Doctor of Philosophy, 2021

Dissertation Directed by: Professor Daniel Lathrop
 Department of Physics

The magnetohydrodynamics of Earth have been explored at the University of Maryland and the Institute of Geosciences in Grenoble, France through experiments, numerical models, and machine learning. The interaction between Earth's magnetic fields and its outer core is emulated in a laboratory using the three-meter spherical Couette device filled with liquid sodium driven by two independently rotating concentric shells and an external dipole magnetic field. Recently, the experiment has undergone modifications to increase the helical flows in the poloidal direction to bring it closer to the convection-driven geodynamo flows of Earth. The experiment has 31 surface Hall probes measuring sparsely the external magnetic field. The numerical model, XSHELLS, solves the coupled Navier-Stokes and induction equations numerically to give a full picture of the internal velocity and magnetic field, however, it cannot resolve all the turbulence. In this thesis we aim to improve the prediction of magnetic fields in the experiment by performing studies both on experimental data and simulation data. First, we analyze the simulation data to assess the viability of

using the measured external magnetic field to represent the internal dynamics of the velocity and magnetic field. These simulations also elucidate the internal behavior of the experiment for the first time. Next, we compare the experimental magnetic field measurements with the extrapolated surface magnetic field measurements in simulations using principal component analysis by matching all parameters but the level of turbulence. Our goal is to see if (i) the eigenvectors corresponding to the largest eigenvalues are comparable and (ii) how then the surface measurements of the simulation couple with the internal measurements, which are not accessible in the experiment. Next, we perform several machine learning techniques to see the feasibility of using the current probe setup to predict the magnetic fields in time. In the second to last chapter, we assess the potential locations for magnetic field measurements. These studies provide insight on the measurements required to predict Earth's magnetic field.

PREDICTING THE MAGNETIC FIELD OF THE
THREE-METER SPHERICAL COUETTE EXPERIMENT

by

Sarah Cassie Burnett

Dissertation submitted to the Faculty of the Graduate School of the
University of Maryland, College Park in partial fulfillment
of the requirements for the degree of
Doctor of Philosophy
2021

Advisory Committee:
Professor Daniel Lathrop, Co-Chair/Advisor
Professor Kayo Ide, Co-Chair/Advisor
Professor Maria Cameron
Professor Brian Hunt
Professor Vedran Lekić

© Copyright by
Sarah Cassie Burnett
2021

Acknowledgments

First I want to acknowledge my committee and advisors. I admire them both as people and world-class scientists. I have learned so much from them during my time at Maryland. I want to thank Masha Cameron for both her support as professor and as a fellow mom. Brian Hunt and Ved Lekić for their clear and thought-out explanations to difficult concepts. Daniel Lathrop for being there whenever. Even when I didn't know how much I needed it. Kayo Ide for challenging me to be my best researcher.

I'd like to recognize the three-meter team (Nolan Ballew, Don Martin, Heidi Myers, Artur Perevalov, and Ruben Rojas) and those affiliated (Ankit Barik and Santiago Triana). It has been great working with a team of talented, fellow mad scientists on the massive three-meter experiment.

I would also like to acknowledge the team at ISTerre in Grenoble. I had never left the country before my study abroad, and they welcomed me graciously. I particularly want to thank Henri-Claude Nataf for his advice on research and assistance getting settled in. I thank Nathanaël Schaeffer for all his help and discussions, any day and night. Also, welcoming me into his home to eat fondue with his family and play Pandemic (little did we know...)

I want to thank my friends. Particularly Brandon Alexander, Sarthak Chandra, Jaideep Pathak, and Ayushi Saxena. Our friendship and shared enthusiasm for

math and dynamical systems influenced me to be a better teacher and scientist. I appreciate that I can always count on y'all to talk with about academics and life.

Thank you, baby John Paul for letting me sleep sometimes. Finally, my husband who I value so much. Your support and patience through the long process of graduate school gave me the perseverance to finish.

I gratefully acknowledge the support of the National Science Foundation Graduate Research Fellowship Program (DGE-1322106) and the Grant (EAR-1417148).

Table of Contents

Table of Contents	iv
List of Tables	vi
List of Figures	vii
List of Abbreviations	ix
Chapter 1: Introduction	1
1.1 Background	1
1.1.1 Geodynamo	2
1.1.2 Magnetohydrodynamic Spherical Couette Device	10
1.2 The Three-Meter Diameter Sodium-Filled Spherical Couette Experiment	11
1.2.1 Comparison in parameters (Earth, simulations, experiment)	19
1.3 Objective and Contributions	21
Chapter 2: Numerical Simulations	24
2.1 Objectives	24
2.2 XSHELLS: the rotating spherical fluid simulation	24
2.3 Modifications to the model for 3m	27
2.4 Simulation parameters	34
2.5 Fluctuation Studies of simulation runs	36
2.5.1 Time series analysis	37
2.5.2 Discussion	40
2.6 Radial correlation studies of simulation runs	41
2.6.1 Discussion	47
Chapter 3: Principal component analysis of mechanical MHD simulations and experiments	49
3.1 Objectives	49
3.2 Spherical harmonic basis functions	50
3.3 Principal component analysis	52
3.3.1 Approach	54
3.4 PCA studies on the 3-meter system	56
3.4.1 Extrapolated magnetic field of the simulation	57
3.4.2 Comparison of experiment and simulation at hall probe locations	72

Chapter 4: New probe locations	80
4.1 Objective	80
4.2 Linear regression	81
4.3 Information theory	83
4.4 Distance functions	90
4.5 Approach	92
4.6 Conclusion	95
Chapter 5: Machine Learning	97
5.1 Objective	97
5.2 Theory	97
5.2.1 The algorithm for reservoir computing	99
5.2.2 The algorithm for LSTM networks	102
5.3 Results	105
5.3.1 Reservoir computing	105
5.3.2 LSTM	110
5.4 Conclusion	114
Chapter 6: Conclusions and potential future work	116
6.1 Conclusion	116
6.2 Potential work	118
6.2.1 Coupled PCA	118
6.2.2 Data assimilation	119
6.2.3 Machine Learning	121
Bibliography	122

List of Tables

1.1	Table of nondimensional parameters	15
1.2	Table of dimensional parameters	16
1.3	Table of comparison in parameters	19
2.1	Simulation parameters: $Ek = 3 \cdot 10^{-7}$	34
2.2	Simulation parameters: $Le = 0.0026$	34
2.3	Simulation parameters: $\Lambda = 0.055$	34
4.1	Means from single probe tests	94
4.2	Maximum value and locations from single probe tests	95

List of Figures

1.1	Dynamo action: Ω -effect and α -effect diagram	4
1.2	Map of magnetic observatories on Earth	7
1.3	Map of Swarm satellite data coverage on Earth	8
1.4	The three-meter experiment	12
1.5	Diagram of the spherical shell and the coordinate system	14
1.6	Regime diagram	21
2.1	Ring current diagram	28
2.2	Schematic of the magnetic field on a shell due to ring current	31
2.3	External applied field	32
2.4	Meridian slice of fluctuations of the velocity field	39
2.5	Meridian slice of fluctuations of the magnetic field	39
2.6	Radial shell a r_o auto-correlations for $Ro = -0.5$	43
2.7	Radial shell correlations with depth for $Ro = -1.75$	44
2.8	Radial shell correlations with depth for $Ro = -0.5$	45
2.9	Radial shell correlations with depth for $Ro = 1.75$	46
3.1	The radial component of the spherical harmonics on a shell.	51
3.2	Eigenvalues and variance of $Ro = -1.75$	59
3.3	Simulation and Experimental Data of $Ro = -1.75$, $\Lambda = 0.055$, $Ek = 3.3 \cdot 10^{-6}$: Spectra of first eigenvector.	60
3.4	Simulation eigenvectors corresponding to the largest 6 eigenvalues for $Ro = -1.75$, $\Lambda = 0.055$, $Ek = 3.3 \cdot 10^{-6}$	61
3.5	Simulation projection strength map: $Ro = -1.75$	62
3.6	Eigenvalues and variance of $Ro = -0.5$	63
3.7	Simulation and Experimental Data of $Ro = -.5$, $\Lambda = 0.055$, $Ek = 3.3 \cdot 10^{-7}$: Spectra of first eigenvector.	64
3.8	Simulation eigenvectors corresponding to the largest 6 eigenvalues for $Ro = -.5$, $\Lambda = 0.055$, $Ek = 3.3 \cdot 10^{-7}$	65
3.9	Simulation projection strength map: $Ro = -0.5$	66
3.10	Eigenvalues and variance of $Ro = 1.75$	67
3.11	Simulation and Experimental Data of $Ro = 1.75$, $\Lambda = 0.055$, $Ek = 3.3 \cdot 10^{-6}$: Spectra of first eigenvector.	68
3.12	Simulation eigenvectors corresponding to the largest 6 eigenvalues for $Ro = 1.75$, $\Lambda = 0.055$, $Ek = 3.3 \cdot 10^{-6}$	69
3.13	Simulation projection strength map: $Ro = 1.75$	70

3.14	Mean magnetic field for $Ro = -1.75$	73
3.15	Simulation vs. experiment projection strength map: $Ro = -1.75$. . .	74
3.16	Mean magnetic field for $Ro = -0.5$	75
3.17	Simulation vs. experiment projection strength map: $Ro = -0.5$. . .	76
3.18	Mean magnetic field for $Ro = 1.75$	77
3.19	Simulation vs. experiment projection strength map: $Ro = 1.75$	78
4.1	Non-overlapping magnetic field distributions	89
4.2	Effects of non-overlapping distributions on distance measures	90
4.3	Suggested probes locations by team members and affiliates.	93
5.1	RNN diagram	98
5.2	The training phase of RC.	100
5.3	The prediction phase of RC.	101
5.4	Single layer RNN	102
5.5	LSTM diagram	103
5.6	Reservoir computing trial parameters	106
5.7	Hall probe data and RC prediction in time.	107
5.8	Single hall probe and RC prediction in time.	108
5.9	Gauss coefficients and RC prediction in time.	109
5.10	G_ℓ^m and RC prediction in time.	110
5.11	Hall probe data and LSTM prediction in time.	111
5.12	Single hall probe and LSTM prediction in time.	112
5.13	Gauss coefficients and LSTM prediction in time.	113
5.14	G_ℓ^m and RC prediction in time.	114

List of Abbreviations

a	distance of the coil from the z-axis
A	random sparse D_r by D_r matrix
A_φ	azimuthal component of the magnetic vector potential
b	bias
b	magnetic vector field
$\bar{\mathbf{b}}$	time average of the magnetic vector field
$\tilde{\mathbf{b}}$	ensemble spread of the magnetic vector field
B_o	intensity of the imposed magnetic field at the equator of r_o
B_P	poloidal magnetic field component
B_T	toroidal magnetic field component
$C(t)$	LSTM cell state
C	covariance matrix
CMB	core-mantle boundary
d	number of snapshots in a time series of data
D	dimensionality of the data
D_r	dimensionality of the reservoir
$\Delta\Omega$	angular velocity difference between the inner and outer shells
Δt	time step
DTS	Derviche Tourneur sodium experiment
Ek	the Ekman number
Em	magnetic Ekman number
η	magnetic diffusivity of liquid sodium
EOF	empirical orthogonal function
f	rotation rate
g	Gauss coefficient vector
g_ℓ^m	the projection strength of a vector onto the (ℓ, m)-spherical harmonic basis vector
$G_\ell^{m,c}$	scalar Gauss coefficient corresponding to the cosine term in Y_m^ℓ
$G_\ell^{m,s}$	scalar Gauss coefficient corresponding to the sine term in Y_m^ℓ

$h(t)$	hidden layer
H	entropy
HPC	High Performance Computing
$i(t)$	hidden layer
I	current applied through the coils
IREAP	Institute for Research in Electronics and Applied Physics
JS	Jensen-Shannon
K	a 31 by 24 matrix of spherical harmonic basis vectors
KL	Kullback-Leibler
L	characteristic length (here r_o)
\mathbf{L}	are the left singular vectors
ℓ	spherical harmonic degree
$\vec{\ell}$	a left eigenvector
λ	largest eigenvalue of \mathbf{A} scaling factor
Λ	Elsasser number
LSTM	Long short-term memory
m	spherical harmonic order/azimuthal wavenumber
$m(\cdot)$	pointwise mean of probabilities
μ	the magnetic permeability constant
MHD	magnetohydrodynamic
N	number of snapshots in time
n_{bl}	number of inner and outer boundary layers
NN	neural networks
ν	liquid sodium viscosity
Ω	angular velocity of a shell
$p(\cdot)$	true probability distribution
P	a point P
p^*	reduced pressure absorbing all potential forces
$P_\ell^m(\cos \theta)$	Schmidt semi-normalized associated Legendre polynomials
\mathcal{P}	Gauss coefficients fo the poloidal magnetic field
$(\mathcal{P}_m^\ell)_{\text{imposed}}$	imposed poloidal magnetic field coefficient

$\hat{\varphi}$	azimuthal directional unit vector
PCA	Principal Component Analysis
Pm	magnetic Prandtl number
$q(\cdot)$	model probability distribution
r	radius or radial coordinate (as subscript)
r_i	inner shell radius
r_o	outer shell radius
\hat{r}	radial directional unit vector
\mathbf{R}	the right singular vectors of X
RC	reservoir computing
Re	Reynolds number
Rm	magnetic Reynolds number
RNN	recurrent neural network
ρ	the fluid density
Ro	Rossby number
RV	Random Variable
$s(t)$	hidden layer
SHTns	Spherical Harmonic Transform (by Nathanaël Schaeffer)
σ	sigmoid activation function
Σ	the eigenvalues of X
SV	Geomagnetic secular variation
SVD	singular value decomposition
T	characteristic time (here τ)
T_p	training period
τ	rotation time
\mathcal{T}	Gauss coefficients for the toroidal magnetic field
TC	tangent cylinder
TV	total variation
$\hat{\theta}$	polar directional unit vector
θ_c	colatitude
3D	three-dimensional
3m	Three-meter experiment
\mathbf{u}	full 3D velocity vector field
U	characteristic velocity (here u_{rms})
U_u	toroidal velocity field component

$U_{\mathcal{V}}$	poloidal velocity field component
\mathcal{U}	Gauss coefficients fo the toroidal velocity field
\mathcal{V}	Gauss coefficients fo the poloidal velocity field
w	weights
\mathbf{W}	diagonal 31 by 31 covariance matrix
$W1$	Wasserstein distance
$x(t)$	input of the feed-forward network
\mathbf{x}	location of a point in Cartesian coordinates
\mathbf{X}	normalized ensemble spread $d \times D$ matrix
XSHELLS	a HPC C++ code for the rotating Navier-Stokes equation in spherical shells
\mathbf{y}	output of the feed-forward network
$Y_{\ell}^m(\theta, \varphi)$	Schmidt semi-normalized Legendre polynomials times exponential or sine/cosine term

Chapter 1: Introduction

1.1 Background

Earth's magnetic field protects the ozone layer from solar winds. Over the past two centuries Earth's magnetic field has reduced by 5% [1], raising interest in better understanding, and possibly predicting, its dynamics. It has been accepted in the 20th century that celestial bodies, like Earth and the sun, can attribute their self-sustaining magnetic fields to dynamo action, a phenomenon that involves positive reinforcement of the magnetic field through its interaction with a turbulent, conductive fluid. Limited by the inaccessibility of Earth's interior, Earth scientists are only able to capture surface measurements of the magnetic field. From seismic waves they deduce the interior contains a solid inner core surrounded by a liquid outer core. Earth's geodynamo is generated by thermochemical convection in the liquid iron outer core, a region bounded by the inner boundary of the crystalline mantle and the solid inner core. The interaction that occurs between the magnetic field and turbulent velocity field leads to this self-sustaining dynamo action. While knowledge of Earth's magnetic field has advanced substantially through observations of geologic data and better computers, new approaches are needed to gain sufficient understanding for prediction. These include laboratory experiments that model

Earth's core dynamics, satellite observations, numerical modeling, data assimilation, machine learning, and information theory.

1.1.1 Geodynamo

The existence of Earth's core was first confirmed by the geologist Richard Oldman in 1906 through seismic P and S waves. Measurements of the core-mantle boundary (CMB) followed in 1912 by Beno Gutenberg who achieved within a few kilometers of the current CMB depth. Soon after came the discovery of a solid inner core within a liquid outer core in 1936 by Inge Lehman. Part of the behavior and composition of the terrestrial interior can be understood by the process of secular cooling, where Earth loses heat to the surrounding space. Heat is transported by radiation, conduction, and convection with the CMB controlling the rate at which heat is lost. Based on the remains of protoplanets found in the form of chondritic meteorites and composition of the sun, it is believed the core is mostly iron [2]. A suitable candidate for the core composition is an Fe-Ni alloy, though experiments have confirmed that mixing in lighter elements results in a better match to the seismically-observed properties of the core. These lighter elements include but are not limited to oxygen, silicon, and sulfur [3], and more controversially, magnesium [4]. The main evidence for lighter elements is how they fit the density and velocity determined by seismology [2, 5]. The conditions of the core have a significant impact on the fluid dynamics. While the inner core is cooling it is crystallizing at the inner core boundary, solidifying heavy elements and releasing lighter elements into the

liquid outer core. Buoyant elements escape into the core by the exothermic process. The release of lighter elements due to secular cooling, also known as compositional convection, is responsible for most of the thermochemical convection that drives the fluid motion [6].

Separate from convection is the effect of Earth's rotation on the fluid dynamics. Taylor-Proudman theorem states that spherical shells steadily rotating with a high angular velocity will organize steady homogeneous flows into uniform columnar structures parallel to the axis of rotation [7]. The two-dimensional flow structure is geostrophic which means there is a balance between the buoyancy force and Coriolis force. It creates a tangent cylinder (TC) parallel to the rotation axis, with a diameter matching that of the inner core, and can maintain the structure if there exists an equal balance of pressure gradient and Coriolis forces. The core composition and condition also have significant impacts on the magnetohydrodynamics (MHDs). Better computers for ab initio simulations and more accurate tools for experimental measurements improve on the accuracy of properties of the material that constitutes Earth's core. In the past 10 years, first-principles calculations and diamond-anvil cell experiments suggest that the thermal conductivity is 2-3 times the thermal conductivity [4] that has been commonly used in geodynamo numerical models.

Rotation combined with convection redirects fluid in the column structures through helicity, or vortices that move perpendicular to the bulk flow, the TC in this case, making the fluid flow only approximately geostrophic. The present magnetic field and fluid motion induce electrical currents which generate a magnetic field that

will also interact with the fluid. Due to the ongoing helical motion, the magnetic field generated by dynamo action is dipolar. The process can be explained by the Ω -effect and α -effect of the magnetic field seen in Fig. 1.1

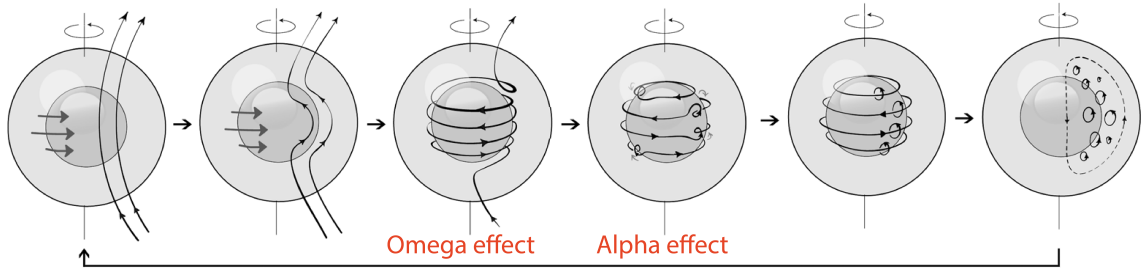


Figure 1.1: The poloidal magnetic field changes direction as it is stretched and flows with the toroidal velocity of the fluid in an action known as the Ω -effect. The influence of the velocity field (stretching and twisting of the magnetic field) converts kinetic energy into magnetic energy. Turbulence leads to the formation of helical motions causing loops to form orthogonal to the toroidal field in an event known as the α -effect. The new direction of the magnetic field then reinforces and even amplifies the original magnetic field in the poloidal direction. This iterative process is known as self-sustaining dynamo action. Modified diagram from [8].

1.1.1.1 Simulations

The discovery of the solid inner core surrounded by a liquid outer core led to one of the first dynamo models in 1946 by Walter Elsasser [9, 10]. His model was formulated as a kinematic dynamo problem which is a dynamo sustained by supplying a steady velocity field. In his model, convection within the conductive liquid outer core positively reinforced the present magnetic field through electromagnetic induction compensating the ohmic dissipation. His model also introduced the poloidal and toroidal geometries used in contemporary simulations (see Sec. 2.6 for further details and equations). The generation of the magnetic field \mathbf{b} by a conductive fluid moving at some velocity \mathbf{u} can be computed by using the induction

equation, which combines Maxwell's equations in a moving conductor with Ohm's Law. Both Elsasser [10] and Batchelor [11] suggested the form of the induction equation,

$$\frac{\partial \mathbf{b}}{\partial t} = \frac{1}{4\pi\kappa} \nabla^2 \mathbf{b} - (\mathbf{u} \cdot \nabla) \mathbf{b} + (\mathbf{b} \cdot \nabla) \mathbf{u}, \quad (1.1)$$

where κ is the electrical conductivity and t is time, to explain the interplay between the velocity and magnetic fields. The first term on the right describes diffusion of the magnetic field. In the absence of the velocity field ($\mathbf{u} = 0$), the magnetic field diffuses and decays. The middle term describes the advection of the field with the fluid motion. The last term describes the rate of stretching of the magnetic field lines. If the latter two terms are sufficiently large they will overcome the diffusion leading to an increase in the magnetic field and, thus, a dynamo. The stretching and twisting process is described schematically in Fig. 1.1.

In 1956, the Bullard-Gellman formalism [12] was derived to find an analytic solution (up to $\ell_{\max} = 4$) for a self-excited dynamo in a steady fluid. Bullard & Gellman discovered a set of selection rules that determined the azimuthal wavenumbers of an induced magnetic field due to the interaction between a present magnetic field and velocity field. In their work they also discuss numerical methods and verify their solutions up to $\ell_{\max} = 4$.

The understanding of the dynamics of the geodynamo began with the assumption of a steady velocity field in order to find analytical solutions. It was further developed by the advancement of computers, making numerical solutions practical. The full 3D MHD system of equations is based on conservation laws and consists

of the Navier-Stokes equations, the induction equation, and the heat and compositional transport equations. In 1995, the introduction of more powerful computing tools allowed for the testing of numerical models of the geodynamo [13, 14]. Simulations have become more realistic as new attributes of the core have been discovered in recent years, such as the heat flux pattern imposed by Earth’s mantle [15]. Numerical methods for geodynamos can be found in several sources [16, 17, 18, 19]. The methods for solving a geodynamo will be omitted here. We will return to see numerical methods in Sec. 2.2 for solving for the full 3D velocity and magnetic field in the rotating experiment subject to the conditions, parameters, and geometry near matching the physical experiment.

1.1.1.2 Available Observations

There are several forms of data that inform us about the geodynamo. The magnetic field near Earth’s crust is observed by airplane and ship surveys, giving small, local magnetic field measurements. Global magnetic field measurements are captured by observatories and satellites. Larger scale observations are the most useful for prediction and validations of numerical models. Almost two centuries of magnetic field data has been captured since the construction of the first observatory in 1832. Friedrich Gauss and Wilhelm Weber began measurements of the intensity of the magnetic field and its horizontal component. Newer observatories measure the magnetic field intensity in vector components of geographic north, geographic east, and downward (i.e. towards the center of Earth) and are cataloged by the

organizations such as INTERMAGNET. Since Sputnik 3 in 1957, several satellite missions measuring the Earth’s magnetic field have been launched. Since 2013, the most notable Swarm A satellite captures the vector magnetic field and the total strength/intensity of the magnetic field using an absolute scalar magnetometer as well as the observed altitude. The coverage of the Swarm Alpha satellite (one of three spacecrafts) can be seen in Fig. 1.3.

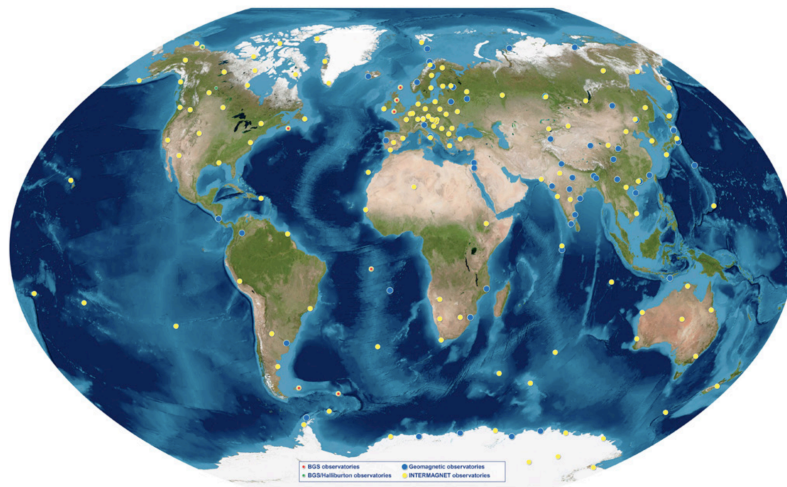


Figure 1.2: Hammer projection of the magnetic observatories provided by the British Geological Survey (BGS) 2019 Geomagnetism Review [20]. The yellow markers are contributions from the International Real-time Magnetic Observatory Network [21], the red markers are BGS observatories, the green markers are BGS/Halliburton(Canada) joint observatories, and the blue markers are for other geomagnetic observatories.

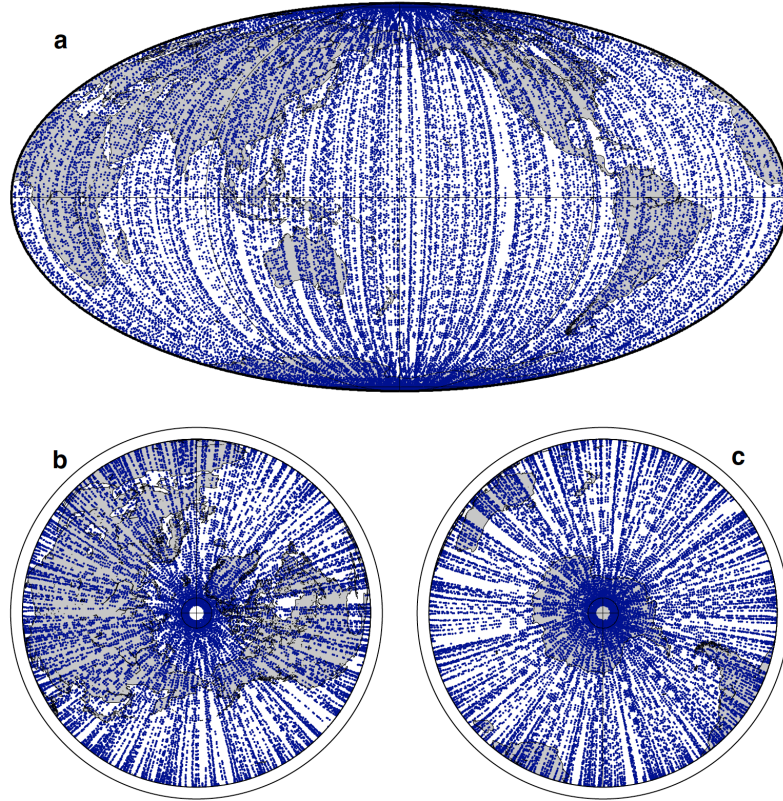


Figure 1.3: Different views of Swarm A satellite Absolute Scalar Magnetometer coverage distribution on Earth. (a) Hammer projection (b) North pole view (c) South pole view. [22]

1.1.1.3 Prediction Problem in Geodynamos

Studying Earth directly has its disadvantages. Although inferences from seismic data have established the 1D structure of Earth [23], constraining the temperature and compositional variations remains a challenge. For example, the estimates of the viscosity of the liquid outer core vary by a few orders of magnitude, because they depend strongly on estimates of core's temperature and composition. Carrying out fully-resolved simulations at the estimated parameters of the highly turbulent system is not currently feasible. When computers can achieve the necessary memory and speed there will still have to be estimations for the unknowns of Earth's

conditions and makeup.

Another limitation to prediction is the sparsity of data that has been collected. The data obtained by observatories is sparse and unevenly distributed with observations primarily over land masses, particularly Europe (see Fig. 1.2). The spatially sparse 200 years of magnetic field data available is short relative to timescales of geodynamo processes. For reference, one measure of Earth's timescale is the diffusive dipole decay which is $\sim 10^5$ years. The spatial distribution of satellite and observatory data can capture spherical harmonics up to degree 13 or 14 [24]. Paleomagnetic observations exist as far back as 4 billion years [25] but they are too sparse in time and space for training machine learning tools or validating current prediction methods. Temporal resolution is on the order of 100 years [26]. Sanchez et al. resolved archaeomagnetic field data up to degree 3 from 1200 BC to 0 AD, degree 4 from 0 AD to 1000 AD, and degree 5 from 1000 AD onwards by binning measurements in 40 year intervals [27]. Satellites are able to cover data over seas, however, because of their placement between the ionosphere and magnetosphere, there is the challenge of i) differentiating between the core's magnetic field and external magnetic field from space and ii) the movement of satellites with respect to Earth makes it difficult to distinguish between spatial and temporal variations in magnetic field.

The International Geomagnetic Reference Field (IGRF) is a community-based model of the main magnetic field and a secular variation estimate. Geomagnetic secular variation (SV) are changes in the Earth's magnetic field on timescales of a year or more, such as a drop in intensity or movement of the magnetic poles. IGRF

predicts 5 years out, up to spherical harmonic degree 13, and is updated every 5 years. Beyond that, a dynamo model is required, using the initial condition of the IGRF [22, 28]. Full 3D models used in a data assimilation framework [22, 29, 30], improve on the IGRF prediction. In most recent studies, data assimilation (Ensemble Kalman Filtering (EnKF)) allows for forecasting the magnetic field evolution over the next 50 years after assimilating the observations from 1840 to 2020 with the ensembles from a dynamo model [30].

1.1.2 Magnetohydrodynamic Spherical Couette Device

The sparsity in data (both spatially and temporally) and the uncertainty in the geodynamo model due to estimates of Earth’s composition motivate another form of study: Magnetohydrodynamic Spherical Couette experiments. Laboratory experiments designed to better understand Earth’s magnetic field emulate the geometry and other physical properties of our planet’s core. This includes the University of Maryland (UMD) 3-meter (3m) experiment, the data from which is a core element of this thesis. The timescales in the experiment are shorter so we can obtain a sufficient amount of data to represent the dynamics in time. The diffusive dipole decay is about a couple seconds —so a relatively significant amount of data can be obtained within a PhD. Another advantage the experiment has over Earth is we know the composition of the interior. We also know the conditions since the experiment runs at a constant temperature with a steady driving force. While experiments contribute to our understanding of Earth’s magnetic field in various ways, they are also limited

by the impracticability of capturing interior data as measurements can be dangerous and unfeasible. Meanwhile, a full 3D numerical model could not practically resolve all the features of this turbulent system and might miss some of the information. The more turbulent the system dynamics, the more demanding the simulation is in storage and time. This thesis analyzes both experimental data and 3D direct numerical simulations in the parameter space closest to the 3m experiment.

1.2 The Three-Meter Diameter Sodium-Filled Spherical Couette Experiment

This project will focus on the data of the 3m experiment [31, 32] which consists of a stainless-steel outer spherical shell concentric with a spherical inner core, as seen in Fig. 1.4. The outer sphere is 2.92 m in diameter with a 2.52 cm shell and the inner sphere is 0.97 m in diameter. Both the inner sphere and the outer sphere can rotate independently. There is an approximately one-meter cavity between them which is filled with metallic liquid sodium. The liquid is held roughly at a constant temperature by oil passing through pipes wrapped about the outside of the outer sphere. The experiment was originally set up with one electromagnet (solenoid loops wrapped concentric to the outer shell) around the equator [31, 32]. Now, there are two electromagnets situated above and below the plane of the equator with circular loops parallel to the equator, imposing an approximately dipole magnetic field (see Fig. 1.4). In 2020, baffles were added to the inner sphere to increase helicity. The data used in this thesis is with the two electromagnets and without baffles.

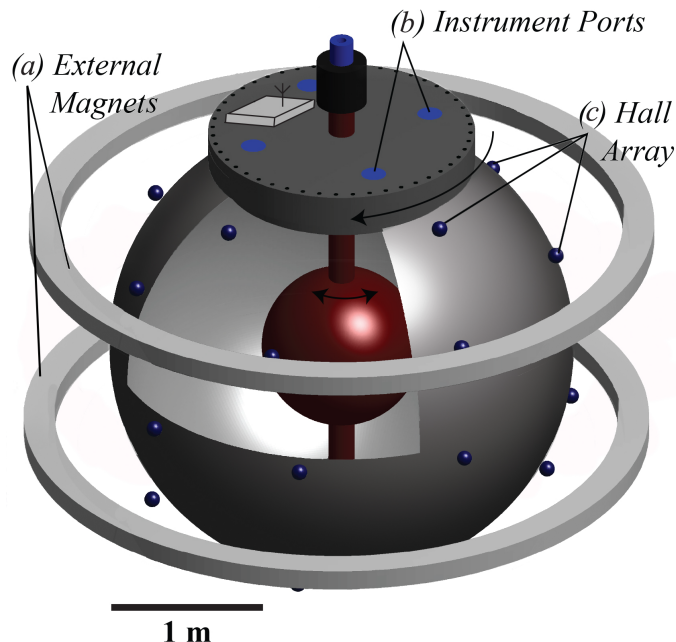


Figure 1.4: Schematics of the 3-meter diameter spherical Couette experiment with the inner sphere and shaft in red and outer shell in gray. Measurements of the magnetic field are taken from the 31 Hall probes on the surface and from 2 inserted into the interior.

The 3m experiment is the successor to several experiments in Prof. Daniel Lathrop’s complex dynamics lab at UMD. The 30 cm diameter experiment [33] was one of the first spherical containers. It was stationary and originally had impellers instead of an inner core. It also had baffles to redirect motion into the poloidal direction. Adding an inner sphere (with and without baffles) to the 30 cm did not lead to dynamo action. The lack of necessary instability can be attributed to an insufficiently high magnetic Reynolds number (see Table 1.1 for definition). Therefore, the team opted for a bigger design. The second largest, 60 cm diameter experiment, originally was made to be a rotating convection experiment by including a cooled inner sphere locked to the outer sphere [34]. The convective dynamics would be dictated by the same set of governing equations as Earth (with temperature bound-

ary conditions that differ). The experiment was modified to allow for independent rotation of the shells. The independent rotation of the inner sphere meant removing the cooled inner sphere and any significant role of convection. The spherical Couette produces a higher magnetic Reynolds number than the laboratory convection-driven flow.

Around the same time that the Maryland team was constructing their first experiments, the Derviche Tourneur sodium experiment (DTS) was created at the Earth Sciences Institute at the Grenoble Alpes University. The 42 cm experiment contains a 14.8 cm inner core. Sodium is heated uniformly and injected into the annulus between the shells. A permanent magnet lies within the copper inner core and supplies a magnetic field through the sodium that is dipole oriented along the axis of rotation [35]. Due to its smaller size, it was not designed to generate dynamos but serve as a prototype for future, larger Earth-like mechanical experiments like the 3m.

All experiments described above emulate the geometry of the ratio of the inner core to the CMB. That is, all that contain inner cores have the ratio of inner to outer radius (r_i/r_o) close to 1/3. One deviation from Earth's geometry that we note is the inner sphere is fixed on a mechanical shaft. All experiments are filled with sodium. Sodium has a high electrical conductivity and can be heated to liquid not far from room temperature. Sodium is practical to use in a rotating experiment as it is lighter than other metals like mercury or gallium. Sodium is also relatively cheap and not toxic. Lastly, sodium is highly reactive to water. Both geodynamo teams collaborate and take extensive measures to ensure the safety of the projects.

1.2.0.1 The Physical Model

This thesis focuses on modeling the spherical Couette flow of liquid sodium between two counter rotating shells and its interaction with an applied dipole magnetic field. The dynamical system can be described by the induction equation (in a different form than Eq. (1.1)) and the Navier-Stokes equation for incompressible fluids.

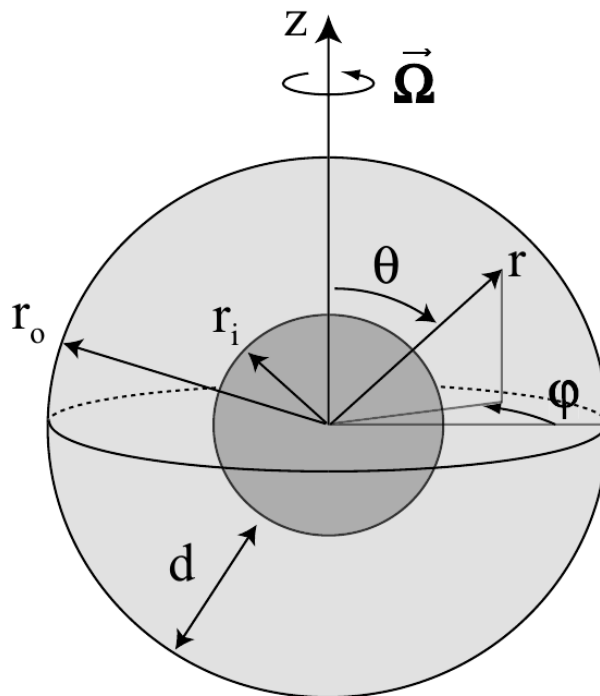


Figure 1.5: Diagram of the spherical shell and the coordinate system^a.

^aImage from: <https://magic-sph.github.io/equations.html>

Let \mathbf{u} and \mathbf{b} be the full 3D velocity field and magnetic field, respectively. Given the solenoidal conditions $\nabla \cdot \mathbf{b} = 0$ and $\nabla \cdot \mathbf{u} = 0$, the governing equations in

nondimensional form are

$$\partial_t \mathbf{b} = \nabla \times (\mathbf{u} \times \mathbf{b}) + \frac{Em}{|Ro|} \Delta \mathbf{b} \quad (1.2)$$

$$\partial_t \mathbf{u} + \frac{2}{Ro} \hat{\mathbf{z}} \times \mathbf{u} + (\nabla \times \mathbf{u}) \times \mathbf{u} = -\nabla p^* + \frac{Ek}{|Ro|} \Delta \mathbf{u} + \frac{\Lambda Em}{Ro^2} (\nabla \times \mathbf{b}) \times \mathbf{b}. \quad (1.3)$$

where p^* is a reduced pressure absorbing all potential forces. The directional unit vector $\hat{\mathbf{z}}$ can be seen oriented in Fig. 1.5. Table 1.1 is a table of some of the significant nondimensional numbers. Table 1.2 is a table of the important dimensional numbers with units.

Parameter	Definition
Ekman number	$Ek = \nu / (r_o^2 \Omega_o)$
Reynolds number	$Re = UL / \nu$
magnetic Ekman number	$Em = \eta / (r_o^2 \Omega_o)$
magnetic Reynolds number	$Rm = UL / \eta$
Rossby number	$Ro = (\Omega_i - \Omega_o) / \Omega_o$
magnetic Prandtl number	$Pm = \nu / \eta$
Elssasser number	$\Lambda = B_o^2 / (\mu \rho \eta \Omega_o)$

Table 1.1: Table of common nondimensional parameters for magnetohydrodynamic systems on rotating spherical shells.

The nondimensional numbers in Table 1.1 have important physical significance. The Ekman number is the balance of the dissipative viscous forces and the Coriolis force from rotation. Nearly the inverse of Ek is the Reynolds number which characterizes the ratio of advection terms to viscous terms in Eq. (1.3) and universally represents the level of turbulence in a fluids system. The magnetic Ekman and magnetic Reynolds numbers are the magnetic equivalent to their fluid flow counterparts. They represent the importance of diffusion of the magnetic field with respect

Symbol	Definition	Units
ν	liquid sodium viscosity	m^2/s
r_o	outer shell inner radius	m
η	liquid sodium magnetic diffusivity	m^2/s
Ω_o	angular velocity of the outer shell	s^{-1}
Ω_i	angular velocity of the inner shell	s^{-1}
f	rotation rate	s^{-1}
τ	rotation time ($1/f$)	s
ρ	liquid sodium density	kg/m^3
μ	magnetic permeability of vacuum	N/A^2
L	characteristic length (here r_o)	m
U	characteristic velocity (here u_{rms})	m/s
T	characteristic time (here τ)	s

Table 1.2: Table of common physical parameters with units for magnetohydrodynamic systems on rotating spherical shells.

to advection and vice versa, respectively. The Rossby number is defined as the differential rotation between the inner and outer spherical shells normalized by the outer shell angular velocity. It is the main driving force of the turbulence in the rotating experiment. The Ro has the most significant role in the dynamical state of the 3m experiment which will be discussed more in Sec. 1.2.1.1. The magnetic Prandtl number is particular to MHD flow as it is the ratio between viscous and ohmic dissipation. The Elsasser number is a way of characterizing the magnetic field strength under the influence of rotation. Denoted Λ , it is the ratio between the Lorentz and the Coriolis forces.

Equations (1.3) & (1.2) are in the reference frame rotating with the outer sphere, therefore the no-slip boundary condition applied to the velocity field is $\mathbf{u}(r = r_o) = 0$ at the outer shell and $\mathbf{u}(r = r_i) = r \sin \theta \hat{\varphi}$ at the inner shell. See Fig. 1.5 for a diagram of the mentioned boundary condition parameters. The magnetic field is that of an electrical insulator outside of the domain, and there is a conductivity jump

between the liquid sodium to the material of the inner and outer shells. Equations (1.3) & (1.2) with the boundary conditions are solved by representing \mathbf{u} and \mathbf{b} in terms of their spherical harmonic decomposition and using the numerical methods discussed in Sec. 2.2.

1.2.0.2 Available Simulations

There are numerous numerical simulations of the spherical Couette experiment. Here, we will focus on the MHD versions, particularly those without a steady flow field like the early kinematic dynamos of Bullard and Gellman's work [12]. Full 3D spherical MHD and dynamo models incorporate the Navier-Stokes equation with the Lorentz force and use the numerical techniques of Gilman [36] and Glatzmaier [16]. Details of the simulation will be discussed in Chapter 2. Simulations of the MHD spherical Couette experiment are closely related to convection driven dynamo simulations. For example, Matsui [37] uses his dynamo model [38] but replaces buoyancy forces with mechanical forcing from the differentially rotating boundaries. Matsui's simulations compare the inertial modes of the simulation with the 3m experiment when it had a single coil at the equator. The DTS experiment is simulated using XSHELLS in [39, 40, 41, 42]. It is more common to find general MHD simulations with spherical shells and a dipole magnetic field such as the following simulation studies [43, 44, 45, 46, 47]. Recent experimental upgrades on 3m were inspired by the simulations of Finke and Tilgner where they add outward forcing from the inner sphere [48]. In the experiment, the force takes the form of

baffles. Ideally, the baffles will create helicity, adding magnetic field in the poloidal direction and generating a dynamo. This list of simulations here is incomplete. Spherical Couette and geodynamo flows can be simulated with open access codes: MagIC¹ and XSHELLS².

1.2.0.3 Available Observations (of the 3m Experiment)

The experimental data, which will be used in Chapters 3 and 5, is the radial-component of the magnetic field at the 31 Hall probes on the outer shell as indicated in dark blue in Fig. 1.4. They are taken at a rate of 256 measurements per second. This data is considered temporally-dense and very spatially-sparse. It is pre-processed (unbiased) so that the magnetic field intrinsic to the probe's function is removed. From here, the magnetic field can be analyzed as 31 points in time or these measurements can be projected onto a natural basis for the system such as the spherical harmonics (see Sec 3.2 for more details).

Other measurements that are not used in the thesis are two magnetic probes in contact with the sodium measuring in the cylindrical-radial direction and in the cylindrical-azimuthal direction. There are also three dynamic pressure probes and one kinematic pressure probe. The torque on the inner sphere is measured using a strain gauge in between the motor and the shaft. Additionally, my teammates are able to measure the torque applied to the outer sphere from the necessary power required to keep the outer sphere moving at a constant rate. In this set-up, it is

¹Can be found here: <https://magic-sph.github.io/>

²Can be found here: <https://bitbucket.org/nschaeff/xshells/src/master/>

important to note that measurements cannot be made directly of the velocity field or the internal magnetic field. There have been attempts at acoustic velocimetry both in simulations [49] and on the experiment. However, passing a signal through the roughly inch-thick stainless-steel and then recording a returned signal from the liquid sodium has not yet been achieved in practice. Also, additional modes could be excited by the mechanical noise of the experiment.

1.2.1 Comparison in parameters (Earth, simulations, experiment)

Table 1.3 is a reference table for comparison of Earth parameters and what geodynamo simulations [15] are able to accomplish. These are compared to the parameters of the 3m experiment [31] and what we have been able to use in their respective simulations.

Symbol	Earth	geodynamo sims	3m experiment	3m sims
Ek	10^{-15}	$10^{-7} - 3 \cdot 10^{-5}$	$3 \cdot 10^{-8}$	$3 \cdot 10^{-7} - 3 \cdot 10^{-6}$
Pm	10^{-6}	$0.1 - 1$	10^{-5}	$10^{-4} - 10^{-3}$
Λ	10	$1 - 10$	(0, 0.055)	0.0022 & 0.055
Rm	10^3	$10^2 - 10^3$	900	108 - 377
Ro	10^{-6}	$10^{-3} - 3 \cdot 10^{-2}$	(-68, -0.2)(0.2, 65)	(-1.75, 1.75)

Table 1.3: Table of nondimensional parameters comparing Earth, Earth simulations, the 3m experiment, and the 3m simulations.

The largest gap in parameters is the difference in Ek number between Earth and their simulations at a difference of 8 orders of magnitude. For the experiments and its simulations, we manage to get as close as a difference of 1 order of magnitude in Ek for $Ro = -0.5$. The magnetic Prandtl number is linked to the Ek by the Em since $Pm = Ek/Em$. Therefore, there again is the same scale of discrepancies in

Pm as with Ek between the Earth and geodynamo simulations and the experiment and their simulations. Elsasser number can be matched without issues. Since the Ro is the main driving force of turbulence in the experiment, it is not practical (i.e. very small time steps and high spatial resolution) to simulate and keep the low Ek except for a very narrow range of $Ro \in [-1.75, 1.75]$ where we can overlap. The smallest Ro that has been achieved with the physical experiment is 0.2.

1.2.1.1 Dynamic States

Figure 1.6 shows which Λ , Ro , and Ek are available in simulations and experiments via symbols. The colors of the symbols represent the state of the experiment. There are two available states: one where the inertial modes dominate (in black) and the other where there is high torque (in red). The states are dependent on only the Rossby number and are determined by prior analysis with a single coil [31]. The two higher Ro values of 1.67 and 1.75 are close to the parameter space where there are fluctuations between high and low torque states. In water experiments performed on the 3-meter experiment prior to the sodium experiment, the torque was examined for $0.07 < Ro < 3.4$. The authors of [50] determine that from $Ro < 1.8$ the high torque state dominates almost surely (probability of 1).

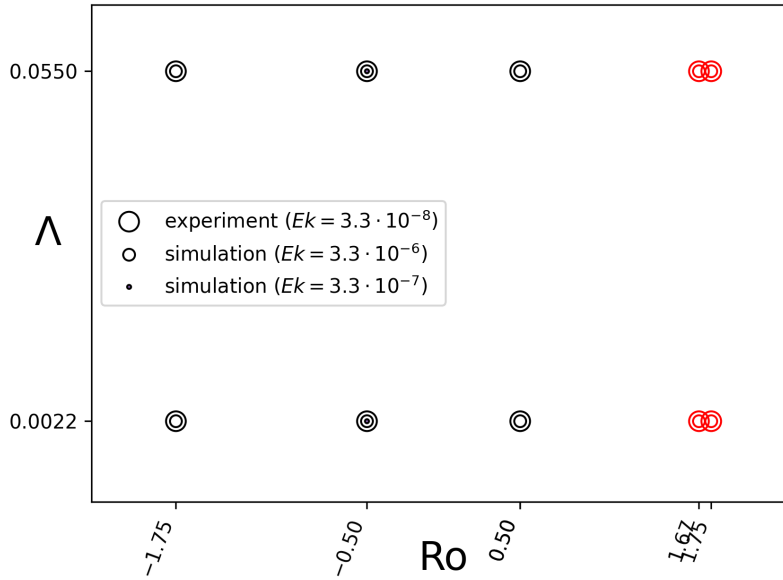


Figure 1.6: The diagram includes experiments and simulations of differing Ek as indicated in the legend. The black color indicates the parameters space where the inertial modes dominate. The red color are parameters with the high torque states.

1.3 Objective and Contributions

This thesis investigates the different approaches used to predict the magnetic field of the three-meter experiment in time. Our objectives and contributions are to:

- Simulate the three-meter experiment.
- Perform time series analysis of the full 3D velocity and magnetic fields.
- Show the surface magnetic field measurements are correlated with internal field.
- Perform PCA of radial magnetic field component from a full resolution of

the simulations at the radial distance equivalent to the experimental measurements.

- Validate the simulation and experiment match in eigenvectors corresponding to the largest eigenvalues of the PCA at certain control parameters.
- Score of the best proposed geometries for new probe locations to add to the surface measurements.
- Test machine learning techniques and their ability to predict the experimental measurements in time.

In this work, we analyze data from both the experiment and simulations based on the physical model described in Sec. 1.2.0.1 in order to combine the advantages of each and mitigate their limitations. The experimental data captures the highly turbulent nature of the system, plus some intrinsic error associated with physical measurements. The measurements are spatially sparse, limited to the magnetic field outside of the experiment, and cannot yet reach the velocity field. Simulations can capture the full magnetic and velocity field but are limited to Reynolds numbers that are 1-2 orders of magnitudes less than the real system due to computational limitations. They can reproduce the dynamic regimes in the systems and give us insight into regions of large variation in the system (seen in fluctuation studies of Sec. 2.5), which can be useful for establishing the initial error in potential data assimilation studies. Furthermore, simulations can give insight on the connection between the surface magnetic field measurements and the magnetic and velocity fields inside the experiment. In Sec. 2.6 we look at how the toroidal and poloidal

components of the surface magnetic field at the location of the probes are connected to the velocity and magnetic field within. In Sec. 3.3, the principal components of both the experiment and simulations are analyzed to determine (i) can the current experimental measurements capture the large variation in the system and if not, (ii) what measurements are necessary to add in the experimental upgrades. In Chapter 4 potential location of new probes are assessed to improve the accuracy of mapping of the radial surface magnetic data onto the spherical harmonics. Next, we look to machine learning techniques in Chapter 5 to test if reservoir computing and LSTM networks can use the sparse spatial magnetic field to forecast the probe measurements in time. Chapter 6 concludes the thesis with a discussion of the presented work and potential future work.

Chapter 2: Numerical Simulations

2.1 Objectives

The following chapter details techniques of the full 3D direct numerical simulation XSHELLS and modifications to the simulation to make it similar to the three-meter experiment. Data analysis is performed on the simulations in the form of fluctuation studies and correlation studies. The fluctuation studies show the distributions of the internal magnetic field and velocity field over time as well as the mean bulk of the fluid/magnetic field. Figures demonstrate the dynamics of the internal fluid and magnetic field motion for different Ro corresponding to the inertial mode and high torque states. Lastly, there are correlation studies to elucidate the relationship of the surface magnetic field measurements, like those captured with the experiment, with the internal toroidal velocity and poloidal magnetic fields.

2.2 XSHELLS: the rotating spherical fluid simulation

XSHELLS [51] is a highly parallelizable full 3D simulation designed to solve the rotating Navier-Stokes equation (Eq. (1.3)) in spherical shells. The C++ code was created by Nathanaël Schaeffer at the Institute for Earth Sciences in Greno-

ble, France and is available and maintained on bitbucket [52] along with his original spherical harmonics C library, SHTns, [53]. Benchmarked with other rotating spherical harmonic codes, XSHELLS is proven to be accurate and fastest [19]. Though there are several built-in high performance options, for the simulations shown here the library performs transforms using OpenMP while computations between radial shells are done with MPI. It is optimized to be fast and use low memory. XSHELLS solves several spherical shell problems including rotating hydrodynamics or rotating magnetohydrodynamics by coupling to the induction equation (Eq. (1.2)). Additionally it has the option to include temperature for convection driven problems like the geodynamo. For the rotating spherical shells experiments, we assume the contributions of the differential temperature is negligible compared to the rotating forces.

XSHELLS employs the numerical techniques of Gilman [36] and Glatzmaier [16]. In the problem of interest, the numerical model solves Eqs. (1.2) and (1.3) for \mathbf{u} and \mathbf{b} in terms of the spherical harmonics using SHTns [53]. Assume we work with solenoidal vector fields, that is, an incompressible velocity ($\nabla \cdot \mathbf{u} = 0$) field and a divergence-free magnetic field ($\nabla \cdot \mathbf{b} = 0$). The magnetic field (likewise the velocity field) is represented by the decomposition of its poloidal and toroidal components respectively,

$$\mathbf{b}(r, \theta, \varphi, t) = \nabla \times \nabla \times [B_{\mathcal{P}}\hat{r}] + \nabla \times [B_{\mathcal{T}}\hat{r}] \quad (2.1)$$

$$\mathbf{u}(r, \theta, \varphi, t) = \nabla \times \nabla \times [U_{\mathcal{V}}\hat{r}] + \nabla \times [U_{\mathcal{U}}\hat{r}]. \quad (2.2)$$

Here $B_{\mathcal{P}}(r, \theta, \varphi)$ and $B_{\mathcal{T}}(r, \theta, \varphi)$ are respective poloidal and toroidal scalars for the magnetic field. Likewise, $U_{\mathcal{V}}(r, \theta, \varphi)$ and $U_{\mathcal{U}}(r, \theta, \varphi)$ are the respective poloidal and toroidal scalars for the velocity field. The vector \hat{r} is the radial position vector. The scalar fields themselves decompose into sums of their radial and angular parts,

$$B_{\mathcal{P}}(r, \theta, \varphi, t) = \sum_{\ell=1}^{\infty} \sum_{m=-\ell}^{\ell} \mathcal{P}_{\ell}^m(r, t) Y_{\ell}^m(\theta, \varphi), \quad (2.3)$$

$$B_{\mathcal{T}}(r, \theta, \varphi, t) = \sum_{\ell=1}^{\infty} \sum_{m=-\ell}^{\ell} \mathcal{T}_{\ell}^m(r, t) Y_{\ell}^m(\theta, \varphi), \quad (2.4)$$

$$U_{\mathcal{V}}(r, \theta, \varphi, t) = r \sum_{\ell=1}^{\infty} \sum_{m=-\ell}^{\ell} \mathcal{V}_{\ell}^m(r, t) Y_{\ell}^m(\theta, \varphi), \quad (2.5)$$

$$U_{\mathcal{U}}(r, \theta, \varphi, t) = r^2 \sum_{\ell=1}^{\infty} \sum_{m=-\ell}^{\ell} \mathcal{U}_{\ell}^m(r, t) Y_{\ell}^m(\theta, \varphi), \quad (2.6)$$

where $Y_{\ell}^m(\theta, \varphi) = P_{\ell}^m(\cos \theta) e^{im\varphi}$ and $P_{\ell}^m(\cos \theta)$ are the Schmidt semi-normalized associated Legendre polynomials. Note that when $m = 0$ these are the Legendre polynomials. In this form, the Gauss coefficients \mathcal{P} , \mathcal{T} , \mathcal{U} , and \mathcal{V} take on complex values. Since we are dealing with real-valued data, then the Gauss coefficients satisfy $\mathcal{P}_{\ell}^{-m} = (\mathcal{P}_{\ell}^m)^*$ where z^* is the complex conjugate of z . Therefore, XSHELLS only stores coefficients for $m \geq 0$ [53].

Pressure in Eq. (1.3) is eliminated by taking the curl of Eq. (1.3) since the curl of the gradient of pressure is 0. This problem was originally used to model the similar French DTS experiment. The code uses second-order in-space finite-difference methods in the radial direction and handles the angular directions using spherical harmonic transforms (pseudospectral) on each radial shell. As it steps in time, it uses implicit Crank-Nicolson scheme for the diffusive terms and treats

the nonlinear terms and Coriolis contribution with an Adams-Bashforth scheme. It performs with second-order convergence in time.

2.3 Modifications to the model for 3m

The original setup for the experiment, which I'll refer to as the *Big Sister* magnetic setup, consisted of 160 turns of square 1.3 cm aluminum wire with a cooling bore. It was placed at the equator with an inner magnet diameter of 3.6 m and outer magnet diameter of 4 m. The turns have a rectangular cross section with wire stacked in 10 layers vertically and 16 layers radially. A current is supplied through the electromagnetic at a range of 0 to 300 A, producing a magnetic field of a maximum of 16 mT [31]. Dan Zimmerman modeled the magnetic field using a finite difference approximation of a single wire at 1.9 m. Likewise, in XSHELLS, the external applied magnetic field is supplied analytically by setting the initial magnetic field equal to the term 'bigsisiter' (i.e. $b=bigsisiter$ in parameter file 'xshells.par').

In XSHELLS, the analytic solution for the magnetic field from the equator coils is computed in terms of spherical harmonics using analysis from the classic electrodynamics text of Jackson [54]. We would like to compute the potential of a point P at \mathbf{x} due to a unit charge at \mathbf{x}' . The contributions of the unit charges are then summed up (integrated) over the curvature of the coil. Examining the Fig. 2.1, we can note that the face of the loop is parallel the to xy-plane and the loop is equal distance from the z-axis.

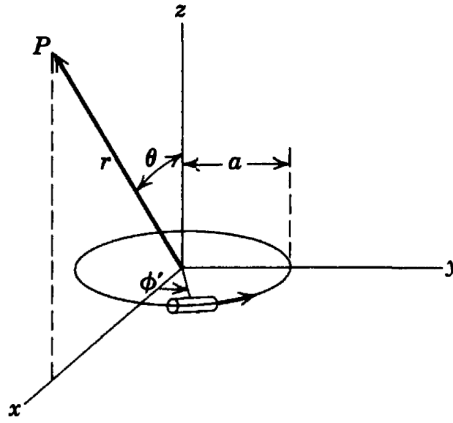


Figure 2.1: The potential of a point P at \mathbf{x} due to a unit charge at \mathbf{x}' . Figure from [54].

This symmetry in the current loop provides only the azimuthal component of the magnetic vector potential,

$$A_\varphi(r, \theta) = \int_0^{2\pi} \frac{Ia\mu \cos \varphi'}{4\pi |\mathbf{x} - \mathbf{x}'|} d\varphi'. \quad (2.7)$$

The value I is the current applied through the coils and a is the distance of the coil from the z -axis. This assumes that the current lies at $\theta = \pi/2$. In terms of the spherical coordinates, we can compute the distance between the coil and a desired point P in terms of the spherical harmonics,

$$\frac{1}{|\mathbf{x} - \mathbf{x}'|} = 4\pi \sum_{\ell=0}^{\infty} \sum_{m=-\ell}^{\ell} \frac{1}{2\ell + 1} \frac{r_{<}^\ell}{r_{>}^{\ell+1}} Y_\ell^{m*}(\theta', \varphi') Y_\ell^m(\theta, \varphi), \quad (2.8)$$

where $r_{>} = \max(r, a)$ and $r_{<} = \min(r, a)$. Substituting Eq. (2.8) into Eq. (2.7) and

simplifying (refer to Jackson [54] p. 183-4 for details) the potential becomes,

$$A_\varphi = -\frac{\mu I a}{4} \sum_{\ell=0}^{\infty} \frac{(-1)^\ell (2\ell - 1)!!}{2^\ell (\ell + 1)!} \frac{r_{\leq}^{2\ell+1}}{r_{>}^{2\ell+2}} P_{2\ell+1}^1(\cos \theta) \quad (2.9)$$

where $(2\ell - 1)!! = (2\ell - 1)(2\ell - 3)(\dots) \times 5 \times 3 \times 1$. From this form of the potential, we compute analytically the \mathbf{b}_r and \mathbf{b}_θ ($\mathbf{b}_\varphi = 0$) for each at desired grid points using,

$$\begin{aligned} \mathbf{b}_r &= \frac{1}{r \sin \theta} \frac{\partial}{\partial \theta} (\sin \theta A_\varphi) \\ &= \frac{\mu I a}{2r} \sum_{\ell=0}^{\infty} \frac{(-1)^\ell (2\ell + 1)!!}{2^\ell \ell!} \frac{r_{\leq}^{2\ell+1}}{r_{>}^{2\ell+2}} P_{2\ell+1}^1(\cos \theta) \end{aligned} \quad (2.10)$$

$$\begin{aligned} \mathbf{b}_\theta &= \frac{1}{r} \frac{\partial}{\partial r} (r A_\varphi) \\ &= -\frac{\mu I a^2}{4} \sum_{\ell=0}^{\infty} \frac{(-1)^\ell (2\ell + 1)!!}{2^\ell (\ell + 1)!} \left\{ \begin{array}{l} -\left(\frac{2\ell+2}{2\ell+1}\right) \frac{1}{a^3} \left(\frac{r}{a}\right)^{2\ell} \text{ if } r < a \\ \frac{1}{r^3} \left(\frac{a}{r}\right)^{2\ell} \text{ if } r \geq a \end{array} \right\} P_{2\ell+1}^1(\cos \theta). \end{aligned} \quad (2.11)$$

On Nov. 8, 2015 the 3m experiment was upgraded by Matthew Adams and Doug Stone from the single coil to two coils located roughly symmetric on the upper and lower hemisphere. Therefore, instead of only having one dipole external electromagnetic field configuration we now have two configurations: a dipole magnetic field is produced by running the current in the same direction in both coils and a quadrupole magnetic field produced by running the current in opposite directions. This will be called the *Big Sister 2* setup. Now, the challenge for *Big Sister 2* is to find an analytic solution in spherical harmonic representation for the coil off of

the xy-plane. We can no longer use Eq. (2.8) for the standard spherical harmonic representation centered at the origin. The following are solutions for the magnetic field components of a single coil located at the spherical radial a and colatitude θ_c taken from [55] using analysis from [54] and visualized in Fig. 2.2,

$$\mathbf{b}_r = \frac{\mu I}{4\pi r^2 \sin \theta \sqrt{r^2 + a^2 - 2ar \cos(\theta + \theta_c)}} \times \left[ar \sin(\theta + \theta_c) f(k) + \frac{(r^2 + a^2) \cos \theta - 2ar \cos \theta_c}{2 \sin \theta} g(k) \right] \quad (2.12)$$

$$\mathbf{b}_\theta = \frac{-\mu I}{4\pi r \sin \theta \sqrt{r^2 + a^2 - 2ar \cos(\theta + \theta_c)}} \times \left[\{r - a \cos(\theta + \theta_c)\} f(k) + \frac{a^2 - r^2}{2r} g(k) \right] \quad (2.13)$$

where

$$f(k) \equiv (2 - k^2) K(k) - 2E(k)$$

$$g(k) \equiv -2E(k) - k^2 K(k) + (2 - k^2) \Pi(-k^2, k)$$

$$k^2 = \frac{4ar \sin \theta \sin \theta_c}{r^2 + a^2 - 2ar \cos(\theta + \theta_c)}$$

where $E(k)$, $K(k)$ and $\Pi(k)$ are the complete elliptical integrals of the first, second, and third kind respectively.

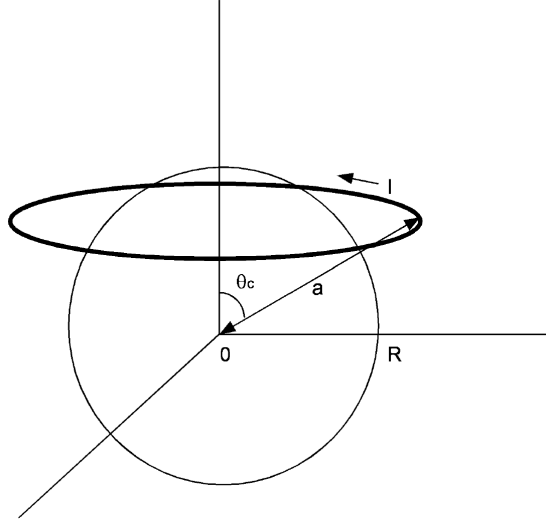


Figure 2.2: Schematic of a ring current I at colatitude of θ_c and distance a from the origin, and a sphere of radius R . Figure from [55].

The elliptic integrals are difficult and costly to represent. With the coils located off the xy -axis, an option would be to compute each on the xy -axis, convert to Cartesian or cylindrical coordinates, translate to their location on the upper and lower hemispheres, and then convert back to spherical harmonics. There is no simple way to translate the spherical harmonics in the z -direction. Instead, we return to using a numerical approximation to the coils. They are calculated by approximating them as single coils located at $z = 0.632$ m and $z = -0.540$ m with $r = -1.9$ m. Without too much difficulty, we can compute the Cartesian components of the magnetic field produced from each coil and then convert them to \mathbf{b}_r and \mathbf{b}_θ (\mathbf{b}_φ negligibly small) at the desired grid points and sum the two coil contributions for the dipole or take the difference for a quadrupole. The magnetic field at a point located at \mathbf{x}

due to the coil located at \mathbf{x}' is computed by numerically integrating the following,

$$B(\mathbf{x}) = \frac{I\mu}{4\pi} \int \frac{(\mathbf{x} - \mathbf{x}') \times d\mathbf{l}}{|\mathbf{x} - \mathbf{x}'|^3} \quad (2.14)$$

using python. The two external applied magnetic field configurations can be viewed using paraview as seen in Fig. 2.3.

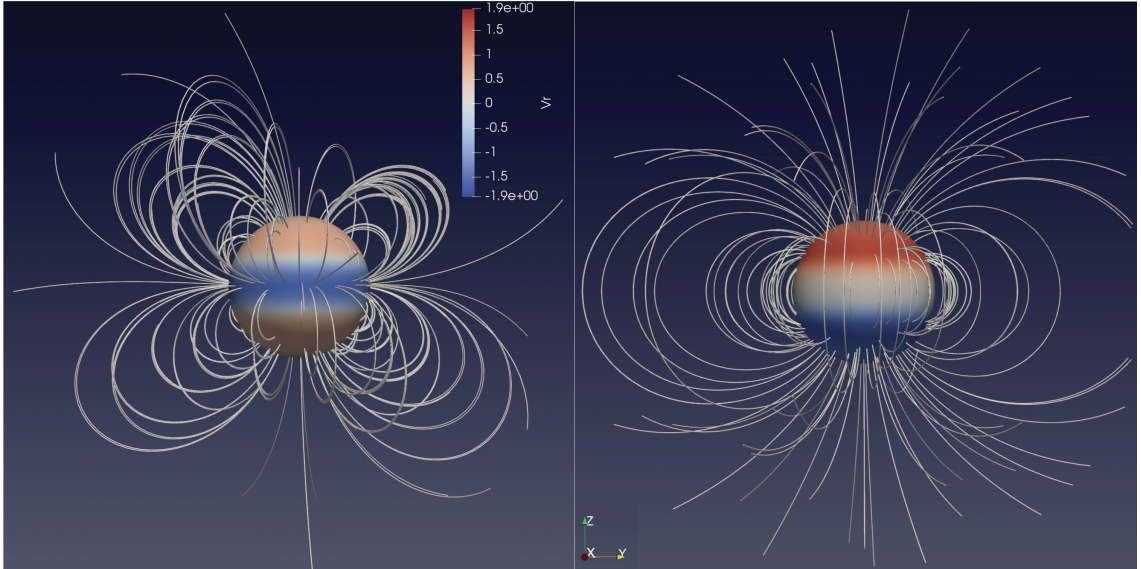


Figure 2.3: Left is the quadrupole magnetic field. Right is the dipole magnetic field. The contour is of the \mathbf{b}_r -component scaled according to the color bar for both configurations. The streamlines of the magnetic field are emitted from the surface. The images make it appear that the source of the magnetic field is inside the experiment rather than the external coils.

In summary, I have modified simulations from the DTS experiment (which has an internal magnet field and copper inner sphere) by constructing the applied exterior magnetic field using numerical Biot-Savart law and projecting it on the lowest 20 poloidal spherical harmonics. I also changed the boundary conductivity of the inner sphere to match the stainless steel inner shell. This code is parallelized with hybrid of MPI and OpenMP. Simulations have been completed on Grenoble's

HPC froggy and UMD’s HPC Deepthought2 for several regimes that match all parameters except for the unfeasibly low Ekman number as discussed in Sec. 1.2.1.

The magnetic field at the equivalent location of the experimental probes is outside the domain of the simulation. Therefore, the magnetic field in free space must be computed by combining the imposed field with the field from the outermost shell of the domain. The length scale in simulations is nondimensionalized by the location of the outermost radial shell of the velocity field. Therefore, the outermost shells of the magnetic field domain is at $r_b = 1.003$ and the location of the Hall probes is $r_p = 1.0522$. Let r_o be the location of the outermost shells of the magnetic field simulation domain and $\mathcal{P}_{\text{imposed}}(r)$ be the imposed external field constructed as described in section 2.2. Note the external magnetic field is constant in time. Then I assume the Hall probes are located in a potential vacuum (air) and compute the measurements from those at the shell r_o using the integral/sum,

$$\mathcal{P}_\ell^m(r, t) = \left(\mathcal{P}_\ell^m(r_o, t) - (\mathcal{P}_\ell^m)_{\text{imposed}}(r) \right) \left(\frac{r}{r_o} \right)^{-(\ell+1)} + (\mathcal{P}_\ell^m)_{\text{imposed}}(r) \left(\frac{r}{r_o} \right)^\ell. \quad (2.15)$$

Now the magnetic field outside the experiment can be measured for any r such as at the probe location $r = r_p$. There is no toroidal field outside of the experiment. The extrapolated magnetic field calculation is used to compare directly with the Hall probes of the experiment using the Principal Component Analysis in the next section. In the rest of the chapter, the computed shell will be included as part of the analysis of the full 3D magnetic field.

2.4 Simulation parameters

This section has information about the parameters used in successful simulations. Simulations are initialized with the imposed field of a certain Λ and $\mathbf{u} = 0$ with either the smallest $Ro = 0.5$ or -0.5 . The simulations are run until the energies stabilize and then $|Ro|$ is increased and parameters adjusted to get the next simulation.

Λ	Δt	\mathbf{n}_r	\mathbf{n}_{bl}	ℓ_{\max}	\mathbf{m}_{\max}
0.0022	$2.9 \cdot 10^{-5}$	360	50, 50	150	100
0.055	$1.6 \cdot 10^{-5}$	400	50, 50	150	100

Table 2.1: Simulation parameters used for the most turbulent cases. The parameters are $Ek = 3.3 \cdot 10^{-7}$ and $Ro = -0.5$.

Ro	Δt	\mathbf{n}_r	\mathbf{n}_{bl}	ℓ_{\max}	\mathbf{m}_{\max}
-1.75	$3.4 \cdot 10^{-6}$	540	40, 40	250	150
-0.5	$7.6 \cdot 10^{-5}$	256	20, 20	150	100
0.5	$1.8 \cdot 10^{-5}$	300	20, 20	150	100
1.67	$2.8 \cdot 10^{-6}$	480	40, 40	250	150
1.75	$3.0 \cdot 10^{-6}$	480	40, 40	250	150

Table 2.2: Simulation parameters for the lower external magnetic field cases. The parameters are $Ek = 3.3 \cdot 10^{-6}$ and $\Lambda = 0.0022$.

Ro	Δt	\mathbf{n}_r	\mathbf{n}_{bl}	ℓ_{\max}	\mathbf{m}_{\max}
-1.75	$3.0 \cdot 10^{-6}$	560	40, 40	250	150
-0.5	$7.6 \cdot 10^{-5}$	200	20, 20	150	100
0.5	$1.5 \cdot 10^{-5}$	320	20, 20	150	100
1.67	$2.9 \cdot 10^{-6}$	480	40, 40	250	150
1.75	$2.8 \cdot 10^{-6}$	480	40, 40	250	150

Table 2.3: Simulation parameters for the higher external magnetic field cases. The parameters are $Ek = 3.3 \cdot 10^{-6}$ and $\Lambda = 0.055$.

During a simulation run, Ro , Λ , and Ek are fixed and time step Δt is adaptive.

All simulations have the magnetic Ekman number $3.13 \cdot 10^{-3}$. The global spatial

resolution is defined based on the number of radial shells, max degree ℓ , and max order m . Eqs. (2.3)-(2.6) are truncated at different maximum ℓ and m values. The angular grid is regularly spaced but the radial grid is refined near the boundary layer which is found to have thickness scaling at \sqrt{Ek} . The refinement of the radial shells at the two inner and outer boundaries assigns the respective number of shells n_{bl} in the \sqrt{Ek} region from each of the boundaries. See Tables 2.1, 2.2, & 2.3 for the number of radial shells in the respective inner and outer boundary layers, n_{bl} , and radial grid n_r for different parameters. The radial grid, time step, and maximum ℓ and m are selected to ensure the simulation obeys physical laws through a spectral convergence test. The fields are checked by computing the ratio of the last four modes of the energy spectrum with lower order modes (neglecting the first $\ell, m = 0 - 2$ as they are related to the imposed field and forcing). The default threshold is a ratio of 0.3 which is chosen to check that the higher modes remain roughly an order of magnitude lower in energy than the lower modes. In order to achieve the low Ek numbers used in these simulations, we add a hyperviscosity and assume there exists a turbulent cascade to small scales in the Ekman layer. The simulations apply hyperviscosity to the angular part of the Laplace operator so that the effective viscosity is increased on the highest spherical harmonics ($\ell_0 > 0.8\ell_{\max}$) [13]. To ensure the simulations reproduce the physical attributes of the experiments, I performed an analysis to compare the spectrum of the experimental measurements with those of the simulation matching all parameters but varying Ek and with/without hyperviscosity (not shown here). An Ekman number of $3 \cdot 10^{-5}$ with hyperviscosity was sufficient to reproduce internal modes in the experiment.

Simulations have been prepared for analysis by running them until the total kinetic and magnetic energies appear statistically stable (over 100 or more rotation periods). I then initialize runs from the statistically stable fields and collect snapshots in time for data analysis.

The rotation time of the simulation is $\tau_{sim} \approx 0.02$. Say we need 8 points per azimuthal wave number to resolve it. Then if we sample it at a rate of 10^{-4} the maximum m is

$$m_{max} = \frac{\tau_{sim}}{8 \cdot 10^{-4}} = 25. \quad (2.16)$$

The sampling rate is sufficient for our purposes. As mentioned in the introduction, observation of Earth's magnetic field are only available up to $\ell_{max} = 13$ or 14. The 31 probes on the current 3m experiment capture up to $\ell_{max} = 4$. In Chapter 3, we will compare PCA results of both the experiment and simulation as well as investigate the number of rotation periods necessary to form the eigenvectors and eigenvalues close to the experimental results. In our current chapter, we proceed with analyzing the full 3D simulation data.

2.5 Fluctuation Studies of simulation runs

The purpose of the following studies is to show the internal behavior demonstrated in simulations by representing the bulk flow and the variation in the velocity field and magnetic field independently. The inside of the physical experiment cannot be measured so this simulation study provides an idea of what the interior of the 3m experiment could look like. These studies were inspired by those by Kaplan et.

al [42] on simulations of the DTS experiment.

2.5.1 Time series analysis

Figures 2.4 & 2.5 are plots of the fluctuations in the kinetic and magnetic levels over a time series, respectively. We first compute the average of each field over time, (which is predominantly $m = 0$) with $\ell_{\max} = 100 - 250$. The equation for the average magnetic field is

$$\bar{\mathbf{b}}(r, \theta, \varphi) = \frac{1}{N} \sum_{i=1}^N \mathbf{b}(r, \theta, \varphi, t_i). \quad (2.17)$$

We can compute ensembles as the difference between each snapshot in time and the average. For the magnetic field we compute the ensemble spread as

$$\tilde{\mathbf{b}}(r, \theta, \varphi, t_i) = \mathbf{b}(r, \theta, \varphi, t_i) - \bar{\mathbf{b}}(r, \theta, \varphi). \quad (2.18)$$

These ensembles reveal the fluctuations outside the large scale $m = 0$ caused by the shear from the driving differentially rotating shells. Effectively revealing signs of the α -effect by removing the Ω -effect. From these ensembles we compute the magnetic energy densities by performing the integral,

$$\langle \tilde{\mathbf{b}} \cdot \tilde{\mathbf{b}} \rangle(r, \theta) = \frac{1}{N} \sum_{i=1}^N \frac{1}{2\pi} \int_0^{2\pi} \tilde{\mathbf{b}} \cdot \tilde{\mathbf{b}}(r, \theta, \varphi, t_i) d\varphi. \quad (2.19)$$

Similarly, we perform the same calculation on the velocity field to find the kinetic energy densities. We display the square root of the energy densities as slices below where the intensity of the fluctuations scale from light in color for closer to zero and change to solid color closer to the maximum values listed. The contours represent the average bulk of the fluid/magnetic field motion. In the velocity field, those are various contours of the mean angular momentum and in the magnetic field plot, the φ - component of the mean magnetic field is shown. In the data we vary the Ro while keeping Λ fixed. We use $\Lambda = 0.055$, which is 25 times the strength of $\Lambda = 0.0022$. The magnetic field should be more active, ideally having more of an interesting impact on the velocity field.

The following figures show the time and azimuthally averaged data which depict the velocity field fluctuations (blue) and magnetic field fluctuations (green). The contours on the magnetic field are the mean toroidal magnetic field. The contours of the velocity field are the mean angular momentum. These are all completed for $\Lambda = 0.055$. The two $Ro = -1.75, 1.75$ have $Ek = 3.3 \cdot 10^{-6}$ and $Ro = -0.5$ has $Ek = 3.3 \cdot 10^{-7}$. These simulation studies overlap the parameters of the 3m experiment (except in Ek).

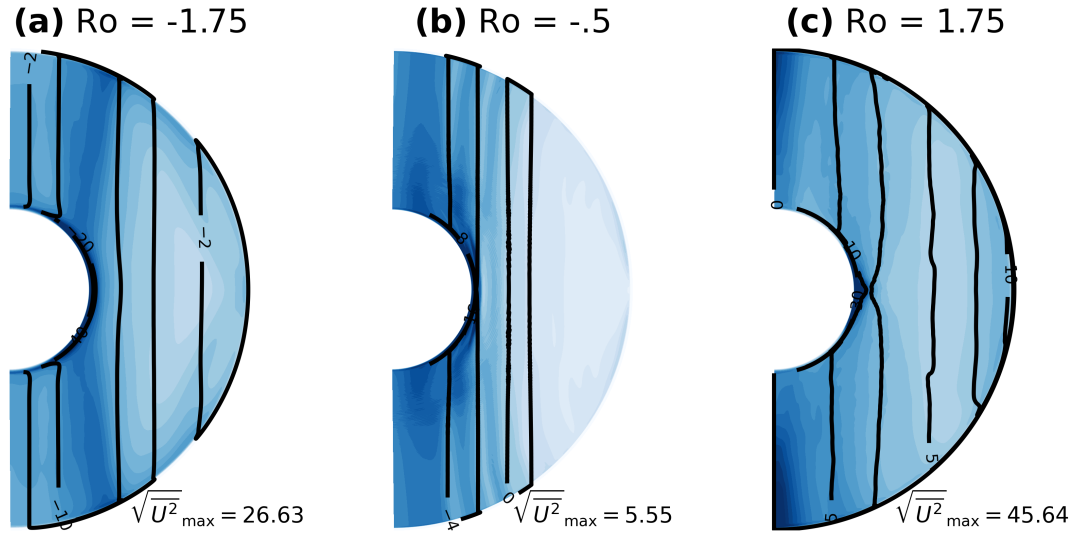


Figure 2.4: Meridian slice of fluctuations of the velocity field. Time and azimuthally averaged velocity field fluctuations are illustrated in white to blue from 0 to the maximum value of the energy density in the lower right of each meridian slice. The contours of the velocity field are the mean angular momentum.

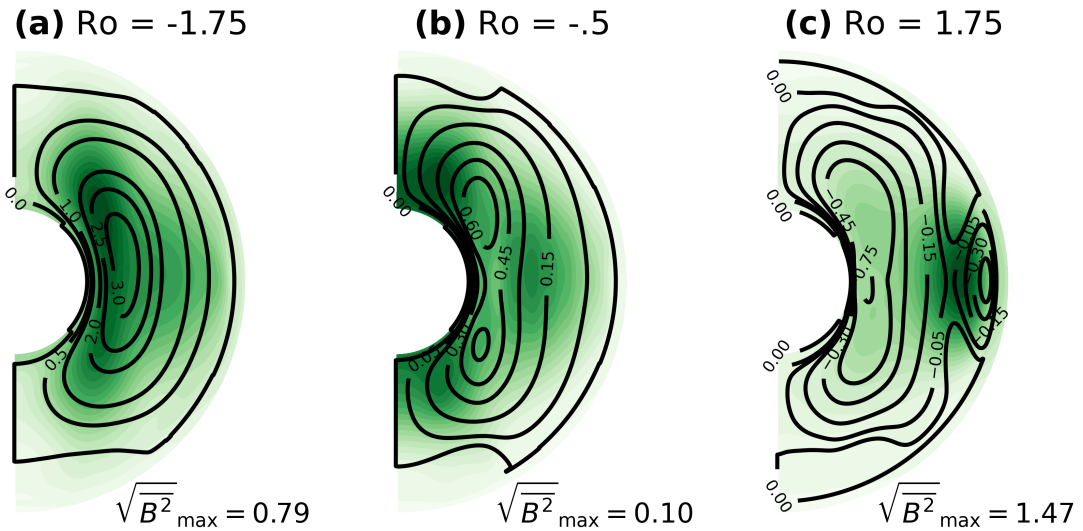


Figure 2.5: Meridian slice of fluctuations of the magnetic field. Time and azimuthally averaged magnetic field fluctuations are illustrated in white to green from 0 to the maximum value of the energy density in the lower right of each meridian slice. The contours on the magnetic field are the mean toroidal magnetic field.

2.5.2 Discussion

The velocity field in Fig. 2.4 shows consistently the highest region of fluctuations is at the equator of the inner sphere. This is where the angular momentum is highest as well. We can also see the contours of the angular momentum are somewhat concentric to the TC but change for different states. For the inertial mode state ($Ro = -1.75$ & -0.5) the contours are straight and parallel to the tangent cylinder but for the high torque state ($Ro = 1.75$), the contour begins to bend towards the poles. Observing the fluctuations shows none of the flows are geostrophic. For $Ro = -1.75$ the TC has more fluctuation towards the axis of rotation as we move from the top (or bottom) toward the inner sphere. For the $Ro = -0.5$ fluctuations are largest near the inner core. This contrasts with the higher $Ro = 1.75$ with fluctuations largest near the north and south poles, perhaps due to centrifugal forces pushing the fluid towards the equator and then up or down towards the poles.

The magnetic field in Fig. 2.5 shows fluctuations coinciding with the mean toroidal magnetic field for the inertial state parameters, $Ro = -1.75$ & -0.5 . For $Ro = -1.75$, the mean toroidal magnetic field is centered in one region near the equator of the inner sphere. The $Ro = -0.5$ study has two regions of the mean toroidal field in the upper and lower hemispheres. Its lack of symmetry is due to the asymmetry of the applied external field with external magnets simulated at different distances from the equator like with the experiment. Its more noticeable for the small $|Ro|$ parameter. Fluctuations for $Ro = -0.5$ have moved towards the poles where we also see fluctuations in the velocity field of Fig. 2.4. The contours

for the parameter $Ro = 1.75$ are symmetric with two regions of high magnetic field intensity at different distances from the equator. Between these regions in a patch of high fluctuations. The $Ro = 1.75$ parameters contrasts with the others by having fluctuations predominantly toward the outside near the equator.

2.6 Radial correlation studies of simulation runs

To prepare for the comparison of the experiment with simulations, from the XSELLS simulation output using python I recreate the radial shell at the radius of the 31 Hall probes that measure the magnetic field outside of the experiment. The location of the Hall probes is outside the domain of the simulation so it must be additionally computed using Eq. (2.3).

In the studies of this section, I look at truncated poloidal and toroidal components of both the magnetic field and velocity field and measure how well they are correlated (or anti-correlated) with the poloidal magnetic field (as decomposed in Eqs 2.4 & 2.6) observed at the equivalent hall probe locations in the simulation. I measure the covariance between the poloidal magnetic field, the probe location, and other fields at various radial shell depths. First by computing the spread and normalizing by the standard deviation. The covariances between the real poloidal component of the hall probe measurements are computed at various depths using a sample of $d = 10000$ (15000 for $Ro = 1.75$) ensemble members truncated at $\ell_{max} = 14$. The covariance is computed by taking the normalize spread elements,

and filling the columns of a matrix, \mathbf{X} . The covariance is calculated as

$$\mathbf{C} = \frac{1}{d-1} \mathbf{X}\mathbf{X}^T. \quad (2.20)$$

Figure 2.6 is an example of a covariance plot. I measure the covariance between the real component of the poloidal magnetic field coefficients at the outer radius of the simulation and itself. The unevenly distributed ticks correspond to the order m . Each pixel in that m -block is a ℓ -number within that order m , increasing the direction of the m -numbers along each axis. So the largest $m = 0$ has $\ell = 1, \dots, 14$; $m = 1$ has $\ell = 1, \dots, 14$ (ex: green box); $m = 2$ has $\ell = 2, \dots, 14$; ...; and $m = 14$ has $\ell = 14$. This produces the m -blocks of decreasing size along the diagonal of each matrix (see one block in green). Note the Gauss coefficient for (ℓ, m) is zero so it is not displayed here.

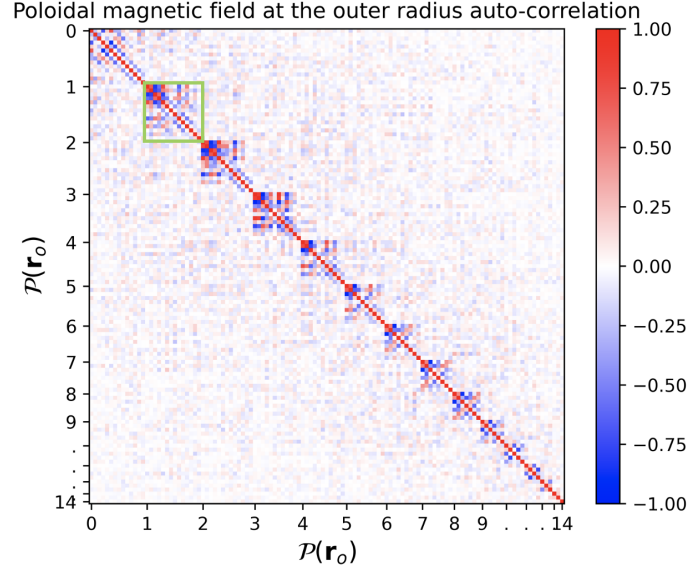


Figure 2.6: Covariance plot of $Re[\mathcal{P}(\mathbf{r}_o)]$ and itself for $Ro = -0.5$. The unevenly distributed ticks on each axis correspond to the order m . Within each m there are the pixels for each ℓ . For example, in the green box we have $m = 1$ with pixels $\ell = 1, \dots, 14$ from top to bottom. The colorscale indicates how correlated (red) or anti-correlated (blue) the elements of $Re[\mathcal{P}(\mathbf{r}_o)]$ are with itself.

Now the figures will be denser in information with multiple covariance plots between the real component of the poloidal magnetic field coefficients at the probe location, $Re[\mathcal{P}(\mathbf{r}_p)]$, and other fields at various radial shell depths such as 95%, 75%, 50%, and 35% (near the inner sphere) of the outer radius.

In Figs. 2.7, 2.8, & 2.9, the left column is the covariance with real component of the poloidal magnetic field coefficients and the right is the covariance with the real component of the toroidal velocity field coefficients at depths corresponding to the outer radius, \mathbf{r}_o . Each are compared with $Re[\mathcal{P}(\mathbf{r}_p)]$ with the objective to show correlations between the magnetic field coefficients at the equivalent experimental probe locations in simulations and the internal field coefficients that can currently only be captured through simulation.

Figure 2.7, is the correlation plot with the $Ro = -1.75$ and $Ek = 3 \cdot 10^{-6}$ simulation run. In the figure, there appears to be some correlation of $Re[\mathcal{P}(\mathbf{r}_p)]$ and the real component of the poloidal magnetic field coefficients at 75 % depth of the outer radius, $Re[\mathcal{P}(0.75\mathbf{r}_o)]$, for $m = 1 - 4$. However it is not very strong. There appears to be weak correlations between $Re[\mathcal{P}(\mathbf{r}_p)]$ and the real component of the toroidal velocity field coefficients at 95% of the outer radius depth, $Re[\mathcal{U}(0.95\mathbf{r}_o)]$. Correlations with deeper velocity field coefficients are too weak to distinguish.

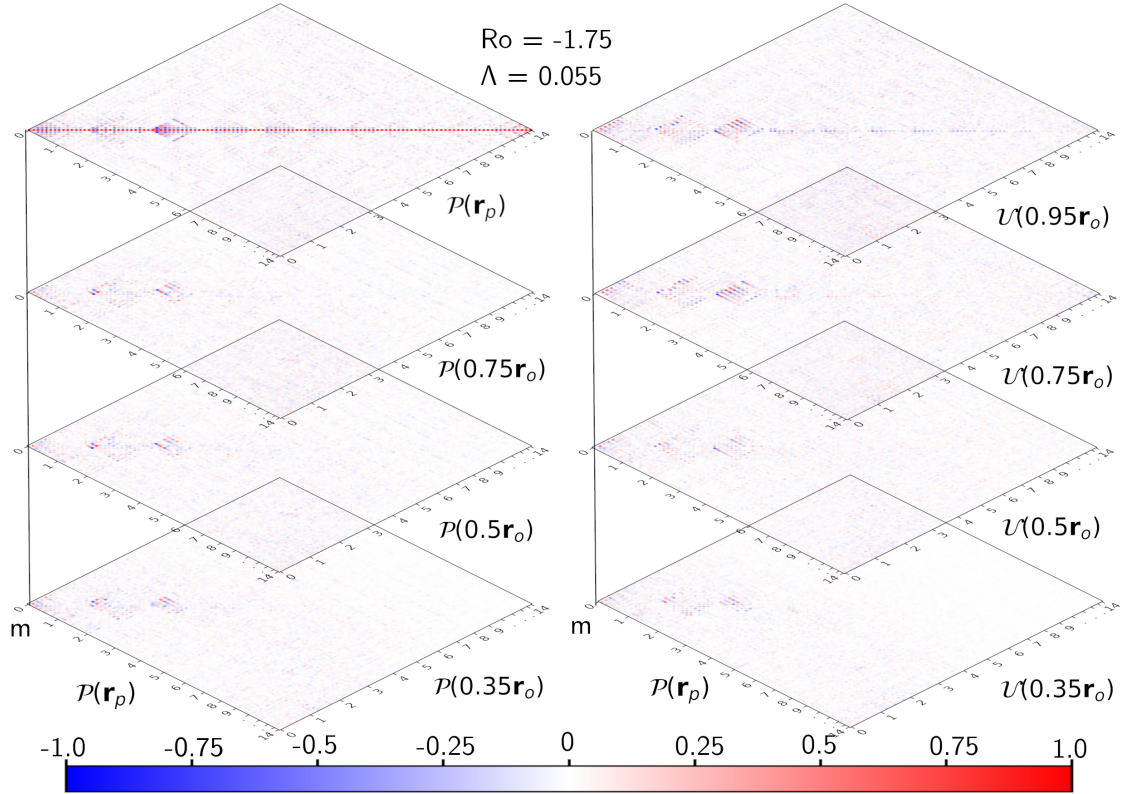


Figure 2.7: Covariance plots for $Ro = -1.75$, $\Lambda = 0.055$, and $Ek = 3 \cdot 10^{-6}$. Each covariance plot is computed from the real component of the poloidal field coefficients at the probe location \mathbf{r}_p and i) the real component of the poloidal magnetic field coefficients (left) and ii) the real component of the toroidal velocity coefficients (right) at depths corresponding to the outer radius, r_o . The unevenly distributed ticks on each axis of each covariance plot correspond to the order m . Within each m there are the pixels for each ℓ . Colors range blue to red with values -1 to 1 respectively denoting how anti-correlated or correlated each element of the field coefficients are with each other.

Figure 2.8, is the correlation plot with the $Ro = -0.5$ and $Ek = 3 \cdot 10^{-7}$ simulation run. Both $Ro = -1.75$ and $Ro = -0.5$ are characterized as inertial mode states due to their Ro but their covariance plots differ. Unlike $Ro = -1.75$, the plots of $Ro = -0.5$ show strong correlations for $m = 0$ & 1 over all the covariance plots. There even weaker correlations in all the plots for $m = 2$ & 3, more so for the magnetic field coefficients than with the velocity field coefficients. Again, large m have very subtle correlations that appear weaker with depth.

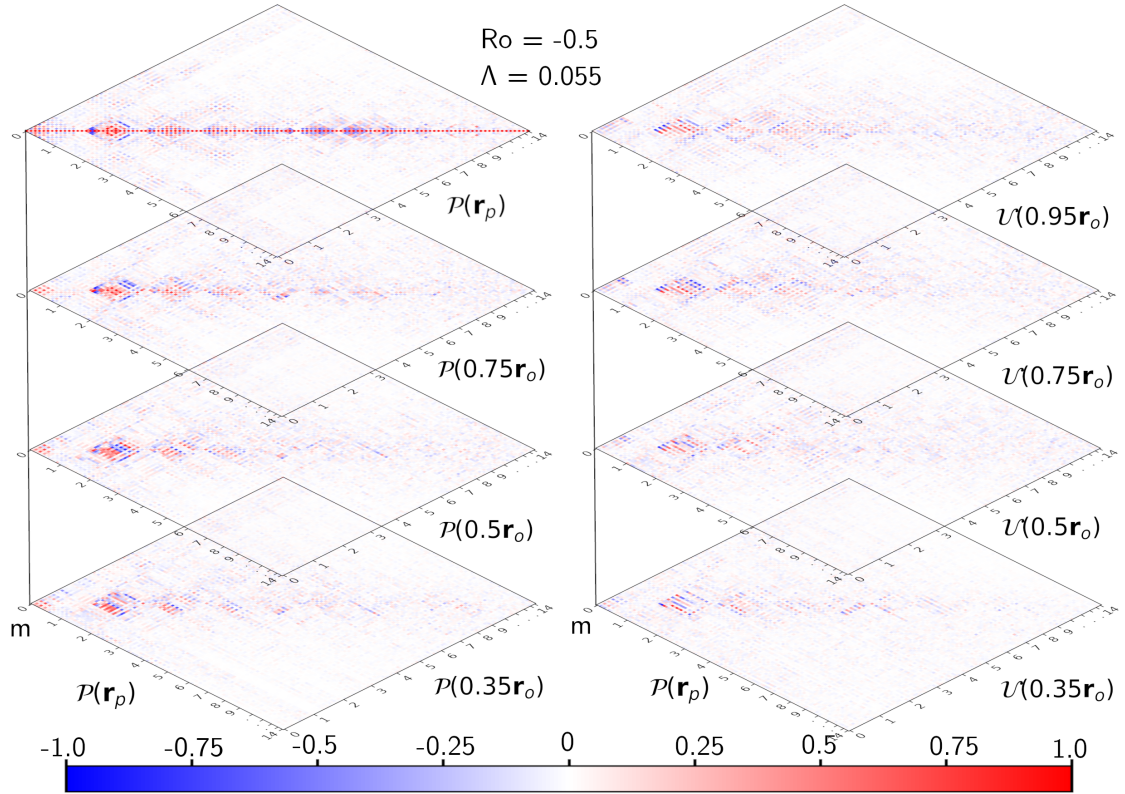


Figure 2.8: Covariance plots for parameters $Ro = -0.5$, $\Lambda = 0.055$, and $Ek = 3 \cdot 10^{-7}$. Each covariance plot is computed from the real component of the poloidal field coefficients at the probe location \mathbf{r}_p and i) the real component of the poloidal magnetic field coefficients (left) and ii) the real component of the toroidal velocity coefficients (right) at depths corresponding to the outer radius, r_o . The unevenly distributed ticks on each axis of each covariance plot correspond to the order m . Within each m there are the pixels for each ℓ . Colors range blue to red with values -1 to 1 respectively denoting how anti-correlated or correlated each element of the field coefficients are with each other.

Figure 2.9, is the correlation plot with the $Ro = 1.75$ and $Ek = 3 \cdot 10^{-6}$ simulation run. Out of all the correlation studies, Fig. 2.9 has the weakest correlations between $Re[\mathcal{P}(\mathbf{r}_p)]$ and the internal field coefficients. There are some weak correlations between $Re[\mathcal{P}(\mathbf{r}_p)]$ and $Re[\mathcal{P}(0.75\mathbf{r}_o)]$ for low $\ell \leq 7$. Also there are some weak correlation between $Re[\mathcal{P}(\mathbf{r}_p)]$ and $Re[\mathcal{U}(0.95\mathbf{r}_o)]$ for $m \leq 2$.

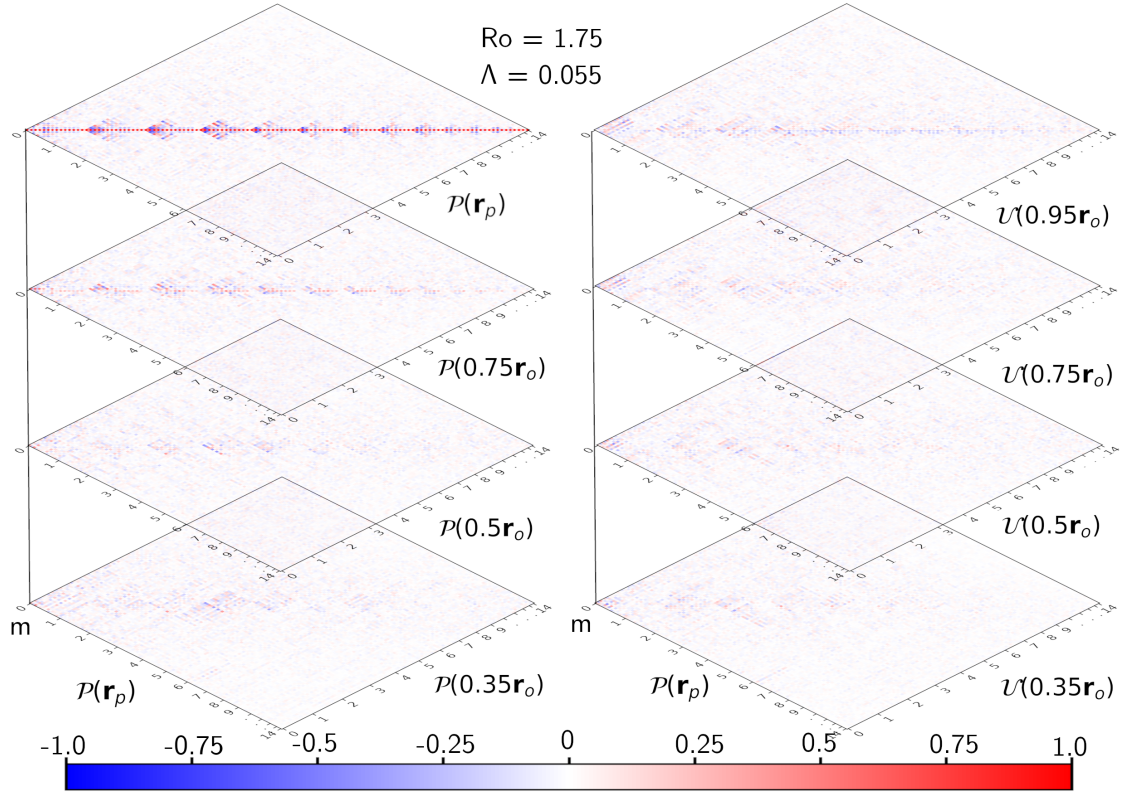


Figure 2.9: Covariances plots for parameters $Ro = 1.75$, $\Lambda = 0.055$, and $Ek = 3 \cdot 10^{-6}$. Each covariance plot is computed from the real component of the poloidal field coefficients at the probe location \mathbf{r}_p and i) the real component of the poloidal magnetic field coefficients (left) and ii) the real component of the toroidal velocity coefficients (right) at depths corresponding to the outer radius, r_o . The unevenly distributed ticks on each axis of each covariance plot correspond to the order m . Within each m there are the pixels for each ℓ . Colors range blue to red with values -1 to 1 respectively denoting how anti-correlated or correlated each element of the field coefficients are with each other.

2.6.1 Discussion

The radial correlation studies were inspired by the analysis of Fournier et al. [22] and Sanchez et al. [30] on geodynamo model data. In the work of Fournier et al., correlation plots, truncated at $\ell_{max} = 10$, are produced measuring between the surface poloidal magnetic field coefficients and the poloidal and toroidal field coefficients separately with correlation plots at various depths from the CMB to the inner core boundary. They observe the axial dipole coefficient is strongly correlated with its surface value at all levels of the radial field. Due to magnetic diffusion, there are correlations found along the diagonal, particularly in the upper part near the CMB [22]. The analysis of Sanchez et al. [30] is a plot of the autocorrelation between the poloidal surface magnetic field coefficients and itself with the field truncated at $\ell = 14$. In their paper, they found the presence of the selection rules of Bullard and Gellman [12] through the interaction of an even (odd) order m only correlates with odd (even) degrees ℓ , producing a ‘checkboard’ pattern in their correlation plot [30].

We see similar effects in Figs. 2.7, 2.8, & 2.9, as Fournier et al. [22] in the correlation of our surface magnetic field with the fields beneath. Magnetic diffusion is present at the surface of the experiment evident by the stronger correlations on the diagonal closer to the surface (see $\mathcal{P}(\mathbf{r}_p)$ vs. $\mathcal{P}(0.75\mathbf{r}_o)$ in Fig. 2.9). In the autocorrelation plot of Fig. 2.6, there is some ‘checkboard’ pattern indicating the selection rules of Bullard and Gellman [12]. Strong correlations in the $m = 0$ and $m = 1$ components in Fig. 2.8 are indicators that these external measurements can constrain both the 3D internal magnetic and velocity fields at least for the set of

control parameters corresponding to $Ro = -0.5$. This could be due to the dominant eigenvectors, which are mostly $m = 1, \ell = 1$, and will be seen in the PCA of the next chapter. The spherical harmonic with $m = 1, \ell = 1$ makes up a large wave that would go deep into the interior. The $Ro = 1.75$ simulations differ from the other two by being in the high torque state. We saw the noticeable difference in the fluctuations of the magnetic fields in Fig. 2.5. Specifically, the largest region of fluctuations was at the equator towards the outer shell. With the fluctuation localized to near the surface, there would not be strong correlations between the surface coefficient measurements and the field coefficient at any significant depth.

Chapter 3: Principal component analysis of mechanical MHD simulations and experiments

3.1 Objectives

In this chapter, we take a look at the eigenvalues and both the spatial and temporal eigenvectors corresponding to the largest eigenvalues. We wish to connect the principal component analysis (PCA) of both the simulation and experimental data to the spherical harmonics at the radial distance r_p from the origin. In the first section, we show the spherical harmonic basis functions for the magnetic field projected onto the radial component. We focus on this component for our studies because we can observe the radial component of the magnetic field in the experiment at the 31 probe locations. The PCA will be performed on the full 2D radial shell from the simulation at the simulation equivalent of r_p , a subsample of the simulated radial shell at grid points closest to the 31 probe locations, and the actual experimental 31 probe measurements. The purpose of these exercises is i) to match the simulation with the experiment by their eigenvectors and ii) to find which spherical harmonics are dominant so that we can make a clever suggestion for new hall probe placements on the experiment.

3.2 Spherical harmonic basis functions

The current 31 experimental measurements were placed to be at the same radial distance from the origin, i.e. the radial shell of radius 1.5369 m or 1.0522 times the inner radius of the outer shell. Where they are located outside of the stainless steel shell, there is no toroidal contribution to the magnetic field. Projecting the poloidal vector spherical harmonics onto the radial unit vector to get the radial component of the magnetic field (Eq. (2.3)) takes the form [9, 10, 12]

$$\hat{r} \cdot B_{\mathcal{P}} = \frac{\ell(\ell+1)}{r^2} \mathcal{P}(r) Y_m^\ell \quad (3.1)$$

with $\mathcal{P}(r) = r^{-\ell}$ outside the sphere and Y_m^ℓ of the form,

$$Y_m^\ell(\theta, \varphi) = P_\ell^m(\cos \theta) (G_\ell^{m,s}(t) \sin m\varphi + G_\ell^{m,c}(t) \cos m\varphi). \quad (3.2)$$

The radial component of the magnetic field now assumes the form of the finite sum of spherical harmonics and scalar Gauss coefficients,

$$\mathbf{b}_r(r, \theta, \varphi, t) = \sum_{\ell=1}^{\ell=4} \sum_{m=0}^{m=\ell} \ell(\ell+1) \left(\frac{r_0}{r}\right)^{\ell+2} P_\ell^m(\cos \theta) (G_\ell^{m,s}(t) \sin m\varphi + G_\ell^{m,c}(t) \cos m\varphi). \quad (3.3)$$

We use the data evaluated at the (r, θ, φ, t) locations of the simulation grid points or the Hall probes in time. Figure 3.1 illustrates the spherical harmonic basis projected onto the radial unit vector corresponding to different degrees ℓ and azimuthal wave numbers m . These plots only show the m values corresponding to the cosine term

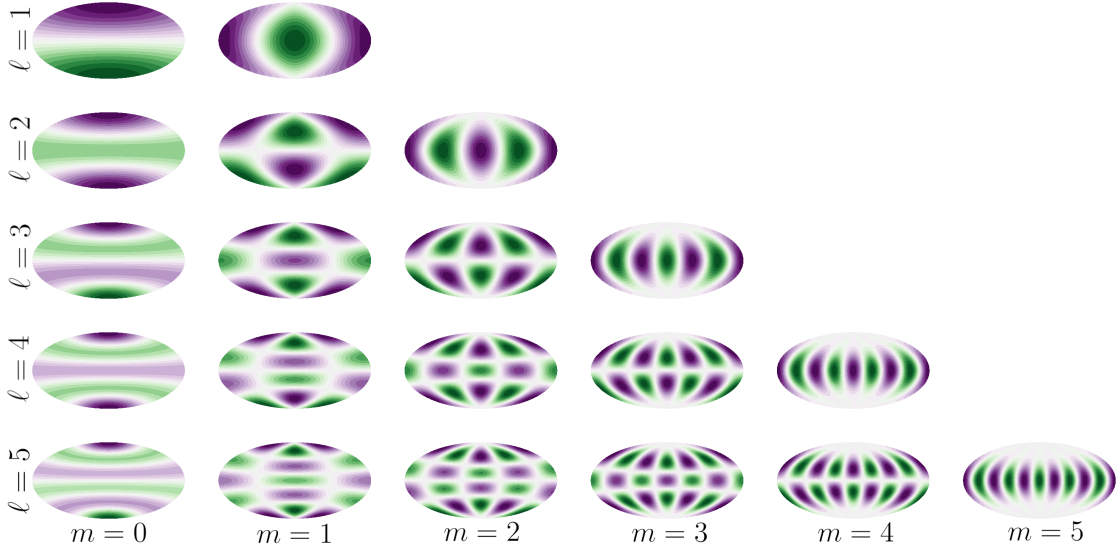


Figure 3.1: The radial component of the spherical harmonics on a shell up to $\ell_{max} = 5$. The degree $\ell = 0$ is constant and is omitted here.

of Eq. (3.2). The other sine m has the same structure except it is out-of-phase of its cosine counterpart. Thus, the azimuthal waves come in pairs.

In the PCA post-analysis we wish to map the spatial eigenvectors corresponding to the dominant eigenvalues to the spherical harmonics. The spherical harmonic basis vectors and the eigenvectors are each normalized so that their L_2 -norm is set to 1. Then the inner product, call it g_ℓ^m , is taken between the spherical harmonic basis vectors of the PCA eigenvectors. In order to ignore the phase difference of cosine/sine azimuthal wave pairs and the phase difference between the basis vectors and the eigenvectors, we can combine the inner products corresponding to the sine and cosine from Eq. (3.3). For each t , let $g_\ell^m = \sqrt{g_\ell^{m,s} + g_\ell^{m,c}}$, then rearrange so that

$$g_\ell^{m,s} \sin m\varphi + g_\ell^{m,c} \cos m\varphi = g_\ell^m \left(\frac{g_\ell^{m,s}}{g_\ell^m} \sin m\varphi + \frac{g_\ell^{m,c}}{g_\ell^m} \cos m\varphi \right). \quad (3.4)$$

Define an angle α of a right triangle to be such that $\cos(\alpha) = \frac{g_\ell^{m,s}}{g_\ell^m}$. Then,

$$g_\ell^m \left(\frac{g_\ell^{m,s}}{g_\ell^m} \sin m\varphi + \frac{g_\ell^{m,c}}{g_\ell^m} \cos m\varphi \right) = g_\ell^m (\sin \alpha \cos m\varphi + \cos \alpha \sin m\varphi) \quad (3.5)$$

$$= g_\ell^m \sin(m\varphi + \alpha). \quad (3.6)$$

For the purpose of analysis, for terms where $m \neq 0$, we can neglect the phase shift between $\cos m\varphi$, $\sin m\varphi$, and the eigenvectors and use g_ℓ^m as a single coefficient for the positive azimuthal wavenumber m . In order to eliminate the phase difference, the strength of the projection will be defined in this manner when we test the alignment of the eigenvectors with the spherical harmonics. For $m = 0$ in the projection strength map, I redefine $g_\ell^0 = |g_\ell^0|$ to be consistent with the other positive g_ℓ^m when $m \neq 0$.

3.3 Principal component analysis

Principal component analysis [56, 57] is a technique that stems from the calculus of variations. It uses eigenvalues as representation of the maximum variation in the direction of their corresponding eigenvectors. In implementation, PCA can uncover the best fit for a natural basis such as Fourier series, Chebyshev polynomials, or in our case, spherical harmonics. In derivation, seen in p.1-6 of [57], it is constructed with introductory knowledge of linear algebra (singular value decomposition), calculus 3 (Lagrange multipliers), and statistics (random variables).

PCA has been extensively used for weather modeling where eigenvectors from

PCA, also called empirical orthogonal functions (EOFs), are found as a basis for statistical weather prediction. In the classic work of Lorenz [59] and White [60] EOFs were used to predict the sea-level pressure field. Lorenz suggests eigenvectors can be fields of several variables (i.e. velocity field and magnetic field combined to make an eigenvector) to create coupled PCA in order to show the variation of multiple fields together. Coupled PCA was executed by Kutzbach [61] for monthly mean sea-level pressure, surface temperature, and precipitation at 23 points. He found that fewer eigenvectors were needed to explain the variance for coupled PCA than doing PCA on the individual fields separately. Though this approach has its appeals as the velocity and magnetic field are coupled by the Lorenz force term, coupled PCA is not used in this these due to the size and number of samples necessary as will be seen in Fig. 3.10 for example. Instead I will analyze only the 2D radial shell of magnetic field and argue that the correlation studies such as Fig. 2.8 show there is a relationship between the surface magnetic field measurements and those beneath for certain azimuthal wave numbers.

More applications of PCA on Earth include retrieving the principal components lateral velocity patterns from tomographic imaging of the mantle [58]. PCA has been implemented on MHD spherical Couette systems. In the geodynamo EOF analysis work by Fujii and Schultz [55], they found the main eigenvector can predominantly (explaining around 90% of the variance) represent SV for periods longer than 5 days. Most recently there has been a *little sister* study of Kaplan's work [42] on simulations of the DTS experiment, studying the energy density and its symmetry of the first three singular modes (eigenvectors) for the fields separately (i.e.

uncoupled) and well inside the boundaries ($r \in [0.425, 0.975]$). This was done in this domain to neglect the dense amount of radial shells near the boundary layer. In his analysis the eigenvectors were symmetric about the equator for $Ro = -1$ and $\Lambda = 0.095$. For Ro further from 0 and higher Λ the dominant mode is antisymmetric about the equator and exhibits chaotic bursts in energy. Aside from their size, the *little sister* setup includes an internal magnetic so the magnetic field is more intense than the *Big Sister* setup making it not ideal to compare with 3m.

3.3.1 Approach

The approach in practice is to place d snapshots of real data of dimensionality D into the rows of a $d \times D$ matrix. We want the distribution to be $\mathcal{N}(0, 1)$, so we then subtract the mean across the columns from each column and divide each column by the standard deviation also taken across the columns of the $d \times D$ matrix to get \mathbf{X} . The normalized matrix \mathbf{X} can then be written as the singular value decomposition (SVD) $\mathbf{X} = \mathbf{L}\mathbf{\Sigma}\mathbf{R}^T$ where columns of \mathbf{L} are the left singular vectors, columns of \mathbf{R} are called the right singular vectors, and $\mathbf{\Sigma}$ are the eigenvalues.

Since the high-dimensional space is so large ($D \sim 10^6$ for a radial shell), it is best to represent the $d \times D$ matrix \mathbf{X} explicitly to compute the SVD with $D \gg d$. A possible approach is to look at $\mathbf{X}\mathbf{X}^T$ which is now a smaller $d \times d$ matrix. Given

$\mathbf{X} = \mathbf{L}\mathbf{\Sigma}\mathbf{R}^T$, the property $\mathbf{R}^T\mathbf{R} = \mathbf{R}\mathbf{R}^T = \mathbb{I}$ and $\mathbf{\Sigma}$ is diagonal, then

$$\mathbf{X}\mathbf{X}^T = \mathbf{L}\mathbf{\Sigma}\mathbf{R}^T (\mathbf{L}\mathbf{\Sigma}\mathbf{R}^T)^T \quad (3.7)$$

$$= \mathbf{L}\mathbf{\Sigma}\mathbf{R}^T\mathbf{R}\mathbf{\Sigma}\mathbf{L}^T \quad (3.8)$$

$$= \mathbf{L}\mathbf{\Sigma}\mathbf{\Sigma}\mathbf{L}^T \quad (3.9)$$

$$= \mathbf{L}\mathbf{\Sigma}^2\mathbf{L}^T. \quad (3.10)$$

The SVD of $\mathbf{X}\mathbf{X}^T$ gives the squared non-zero singular values of \mathbf{X} , up to a rank $d-1$ due there being d snapshots total and to subtracting the mean so the columns of \mathbf{X} can only be at most rank $d-1$. In the next section, we will study the eigenvalues to see if we have a sufficient amount of snapshots to represent the system. Also note that the eigenvectors of $\mathbf{X}\mathbf{X}^T$ are the left singular eigenvectors of \mathbf{X} . The SVD of $\mathbf{X}^T\mathbf{X}$ by similar argument is

$$\mathbf{X}^T\mathbf{X} = \mathbf{R}\mathbf{\Sigma}^2\mathbf{R}^T. \quad (3.11)$$

In this case, the eigenvectors of $\mathbf{X}^T\mathbf{X}$ are the right singular eigenvectors of \mathbf{X} . The form, $\frac{1}{D}\mathbf{X}^T\mathbf{X}$ is the estimated covariance matrix C similar to those in Sec. 2.6. The $D \times D$ matrix is fine to represent for experiments with 31 probes but can be too large to represent for simulation data (unless the data is truncated like in Sec. 2.6). The $\mathbf{X}\mathbf{X}^T$ matrix (also known as the Gram matrix) is much smaller $d \times d$ (here we will use $d = 10000$ or 15000 for simulations).

The next challenge is more of a computational one: how to find the PCA of $\mathbf{X}^T\mathbf{X}$ when the dimension of the data is too large to represent the $D \times D$ matrix \mathbf{R} .

To do this, let's assume $\vec{\ell}$ is an eigenvector of $\mathbf{X}\mathbf{X}^T$ with corresponding eigenvalue λ . Then using some linear algebra, associative properties and λ is scalar,

$$\mathbf{X}\mathbf{X}^T\vec{\ell} = \lambda\vec{\ell} \quad (3.12)$$

$$\mathbf{X}^T(\mathbf{X}\mathbf{X}^T\vec{\ell}) = \mathbf{X}^T(\lambda\vec{\ell}) \quad (3.13)$$

$$(\mathbf{X}^T\mathbf{X})(\mathbf{X}^T\vec{\ell}) = \lambda(\mathbf{X}^T\vec{\ell}). \quad (3.14)$$

So what this says is λ is also an eigenvalue for $\mathbf{X}^T\mathbf{X}$ with corresponding eigenvector $\mathbf{X}^T\vec{\ell}$. We can compute the eigenvalues and left eigenvectors of $\mathbf{X}\mathbf{X}^T$ and then find the i th right eigenvector by computing $\mathbf{X}^T\vec{\ell}_i\sigma_i^{-1}$.

3.4 PCA studies on the 3-meter system

In these studies we look for a few items that are intrinsic to the dynamical system. In the following section we look at the radial component of the magnetic field on the radial shell where the probes are approximately located. Another thing we would expect to see if the eigenvectors corresponding to the natural basis of spherical harmonics. We expect there to be waves which come as pairs of sine and cosine. They can be recognized by similar eigenvalues and two eigenvectors aligning with the same projection strength g_ℓ^m . The largest waves in the experiment correspond with lower m -numbers spherical harmonics (see Fig. 3.1). Likewise, due to the scale of the large waves, their variation is large and thus the variance attained by PCA.

The eigenvalues are shown with the corresponding cumulative variance explained by the eigenvectors corresponding to the largest eigenvalues, V_k . The variance is computed by arranging the eigenvalues in decreasing order, λ_i , for $i = 1, 2, \dots, n - 1$ where $n = \min(N, D)$. Then for each eigenvalue λ_k the corresponding cumulative variance is explained by the sum

$$V_k = \sum_{i=1}^k \lambda_i / \sum_{i=1}^n \lambda_i. \quad (3.15)$$

The six eigenvectors corresponding to the largest eigenvalues will be plotted as hammer/aitoff projections. An analysis of the dominant 30 eigenvectors' alignment with the spherical harmonic basis will follow the spatial eigenvector plots. This is done first with the simulation data on a radial shell. Then in the next section, we subsample the simulation radial shell and compare that with the experimental data.

3.4.1 Extrapolated magnetic field of the simulation

The plots in this section are computed using simulation data on a full radial shell unless otherwise indicated. Each subsection includes the parameter values in the title which should overlap with the experiment except in Ek . The first plot contains a subplot of the eigenvalues for simulations with differing lengths in runs (more snapshots or rotations in time) to see how they compare to the experiment's eigenvalues. Similarly there is a plot of the spectra of the dominant temporal eigenvector for the different length simulation runs and comparison with the experiment. We hope that these plots will justify the amount of simulation snapshots needed for

PCA to represent the real system. The next plot is of the 6 leading eigenvectors which might appear to take the form of the spherical harmonics basis functions of Fig. 3.1. Below that is an assessment of how aligned the leading 30 eigenvectors are to the spherical harmonics. With the current number of probes on the 3m, we can measure up to $\ell_{max} = 4$ so these plots should demonstrate the utility of adding more probes.

3.4.1.1 Simulation $Ro = -1.75$, $\Lambda = 0.055$, $Ek = 3 \cdot 10^{-6}$.

Figure 3.2 contains the eigenvalues and the explained variance for control parameters $Ro = -1.75$, $\Lambda = 0.055$, and $Ek = 3 \cdot 10^{-6}$. In this figure, the first two eigenvalues come as a pair and the 6 largest eigenvalues make up 63% of the cumulative variance for the simulation with 51 rotations. For the experiment with 1098 rotations, the 6 largest eigenvalues make up 60% of the cumulative variance.

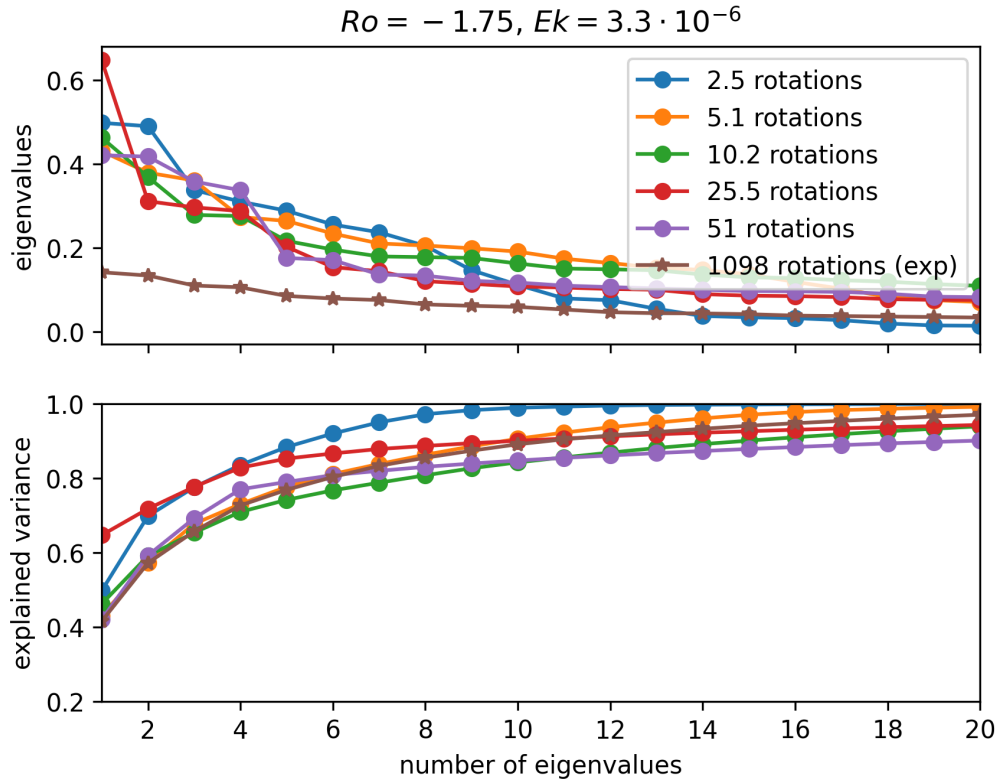


Figure 3.2: PCA eigenvalues and cumulative variance explained by the eigenvalues for simulation magnetic field data on a radial shell for parameters $Ro = -1.75$, $\Lambda = 0.055$, $Ek = 3.3 \cdot 10^{-6}$ for different test lengths. These are compared to the experimental data (from 31 measurements) in brown stars.

Figure 3.3 compares the temporal eigenvector corresponding to the largest eigenvalues for various lengths of simulations run and an experimental run. The first peak of the 51 rotation run overlaps with the first peak of the experiment near $f/f_o = 0.1$.

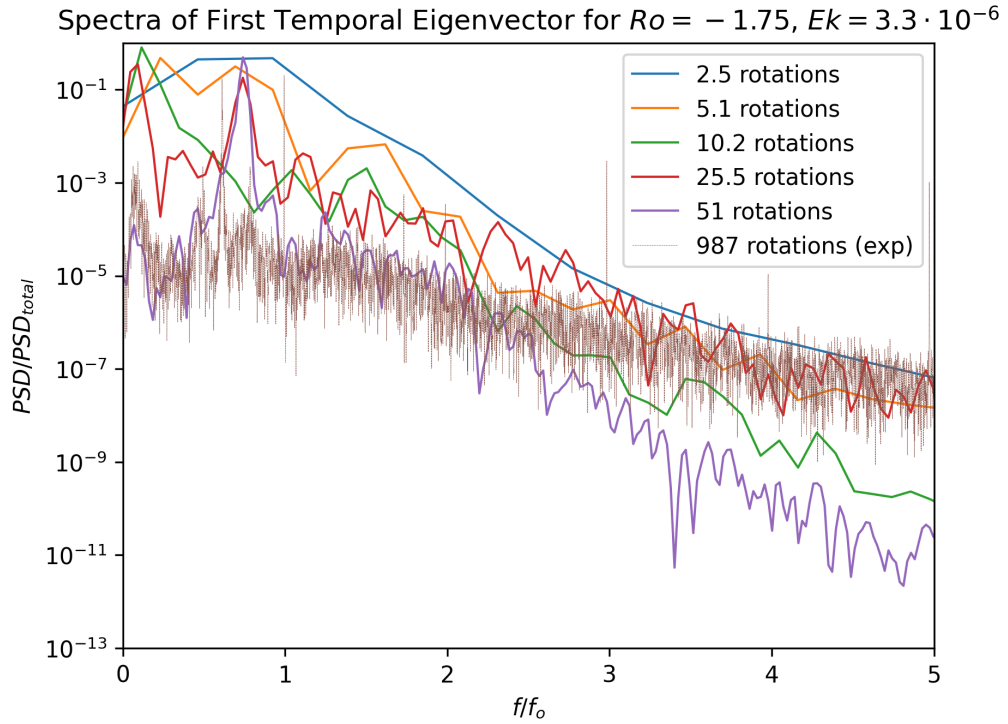


Figure 3.3: Spectra of first eigenvector for simulation and experimental data of $Ro = -1.75$, $\Lambda = 0.055$, $Ek = 3.3 \cdot 10^{-6}$. This plot include different lengths of simulation data to establish the appropriate amount of samples needed to compare to the experiment.

The following subplots in Fig. 3.4 are the eigenvectors corresponding to the 6 largest eigenvalues in order. The first 4 eigenvectors visually appear as pairs of out-of-phase waves. Their corresponding eigenvalues are close, confirming they are pairs.

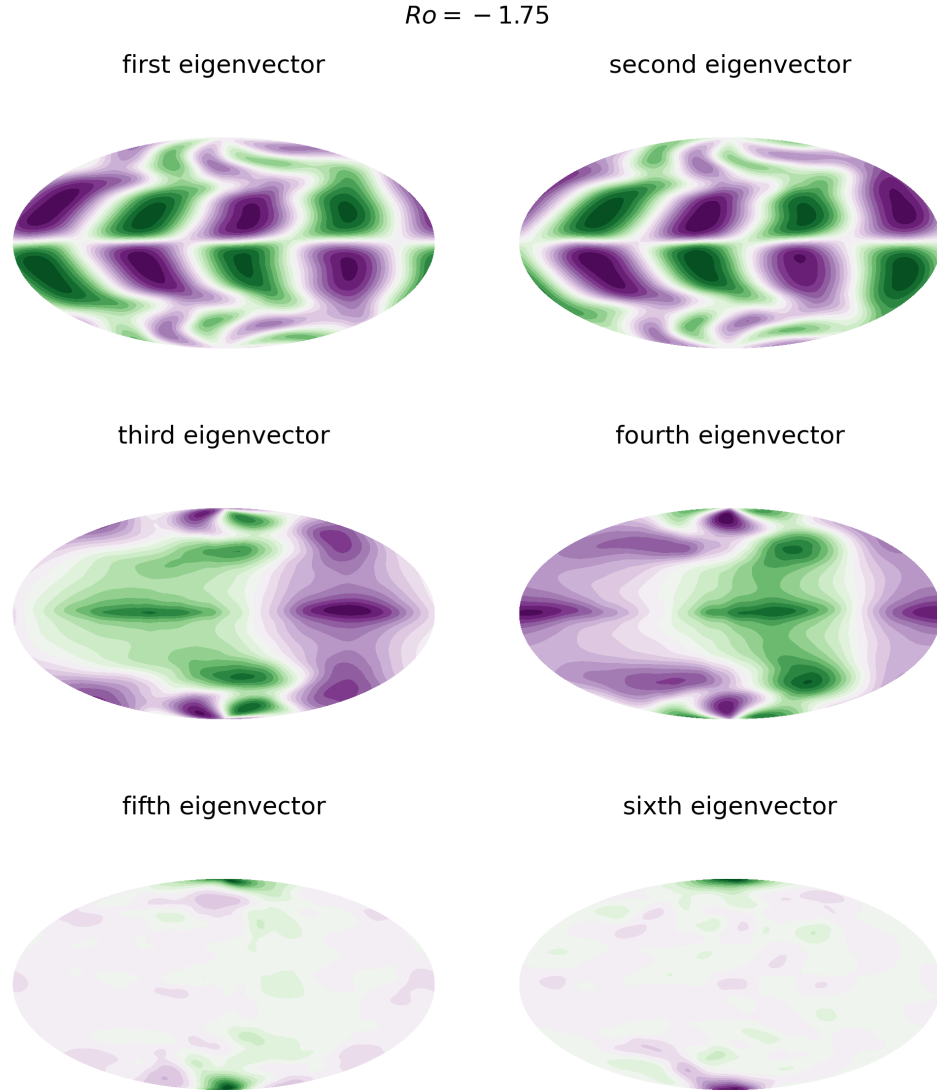


Figure 3.4: Simulation eigenvectors corresponding to the largest 6 eigenvalues for $Ro = -1.75$, $\Lambda = 0.055$, $Ek = 3.3 \cdot 10^{-6}$.

In Fig. 3.5, the strength of the projection of the eigenvectors are shown in the projection map. The principal eigenvector and its pair are mostly the spherical harmonic basis of $(m, \ell) = (2, 3)$. The second pair of eigenvectors appear as a combinations of $(m, \ell) = (1, 1), (1, 3), \&(1, 5)$. The fifth and sixth eigenvectors do not come as pairs, but the seventh and eighth appear to project onto $(m, \ell) = (1, 4)$.

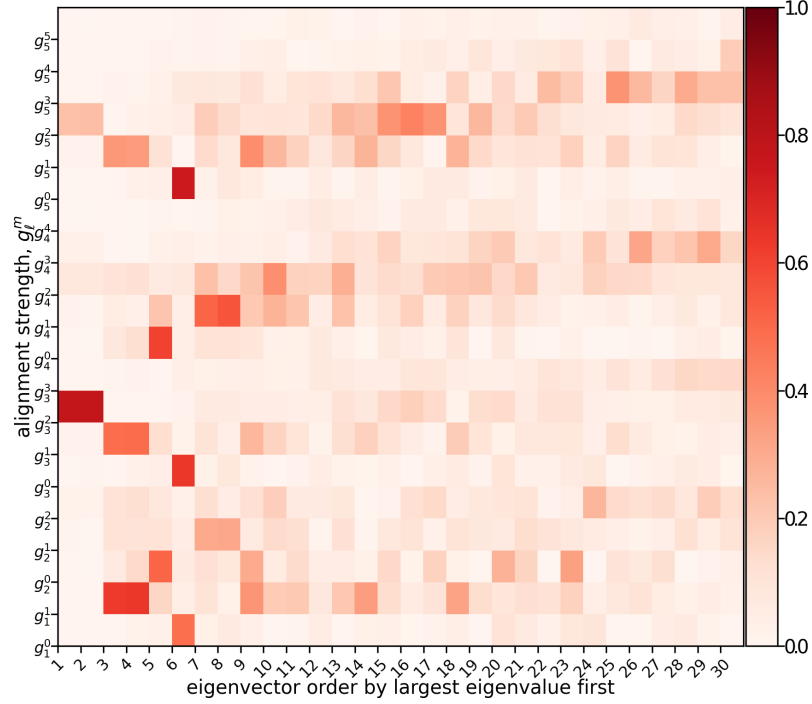


Figure 3.5: Projection strength map for simulation studies at $Ro = -1.75$, $\Lambda = 0.055$, $Ek = 3.3 \cdot 10^{-6}$. The map shows the alignment of the top 30 eigenvectors (in order of their corresponding eigenvalues) with the spherical harmonics basis up to $\ell_{max} = 5$.

3.4.1.2 Simulation $Ro = -0.5$, $\Lambda = 0.055$.

Figure 3.6 also displays the eigenvalues and explained cumulative variance for a variety of simulation lengths and one experimental run. Based on the two longest simulation runs matching, it seems 25 rotations is sufficient for the analysis. There is gap in the cumulative variance of the first two eigenvalues where the simulation is 81%, the experiment has 52% variance. For all analysis, we can see pairs in the largest two eigenvalues.

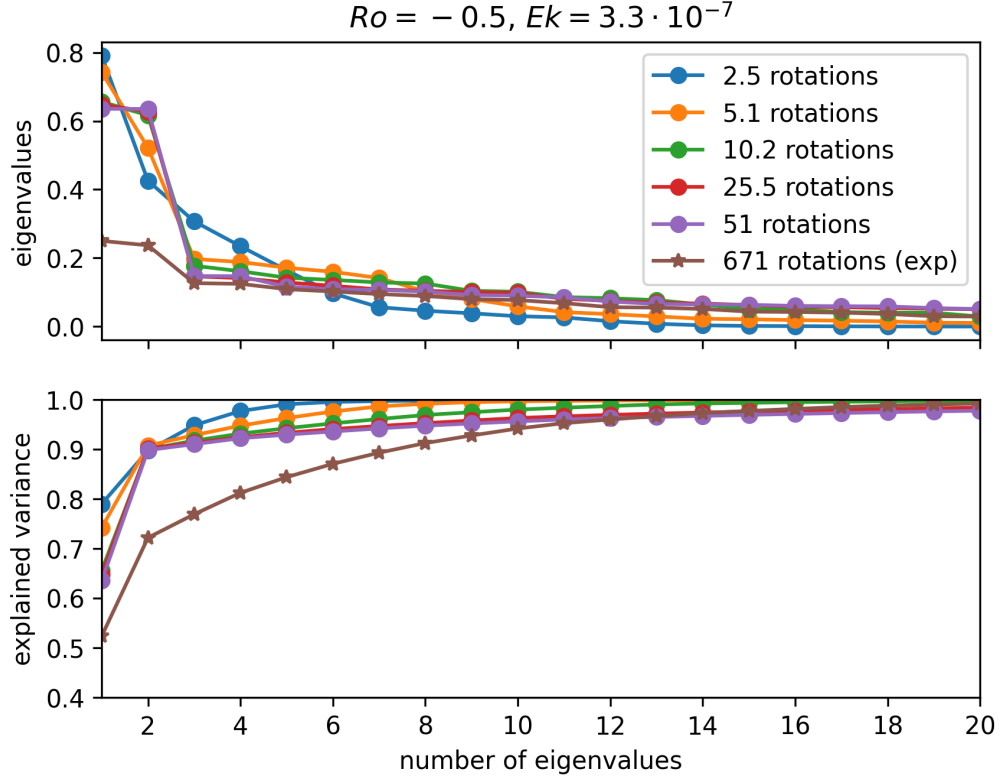


Figure 3.6: PCA eigenvalues and cumulative variance explained by the eigenvalues for simulation magnetic field data on a radial shell for parameters $Ro = -0.5$, $\Lambda = 0.055$, $Ek = 3.3 \cdot 10^{-7}$ for different test lengths. These are compared to the experimental data (from 31 measurements) in brown stars.

Figure 3.7 compares the temporal eigenvector corresponding to the largest eigenvalues for various lengths of simulations run and an experimental run. The first peak of the simulation with more than 10 rotations overlaps the first peak of the experimental run near $f/f_o = 0.1$. Note the noise floor of the experiment where the flat line of the simulation data appears for $f/f_o > 2.5$.

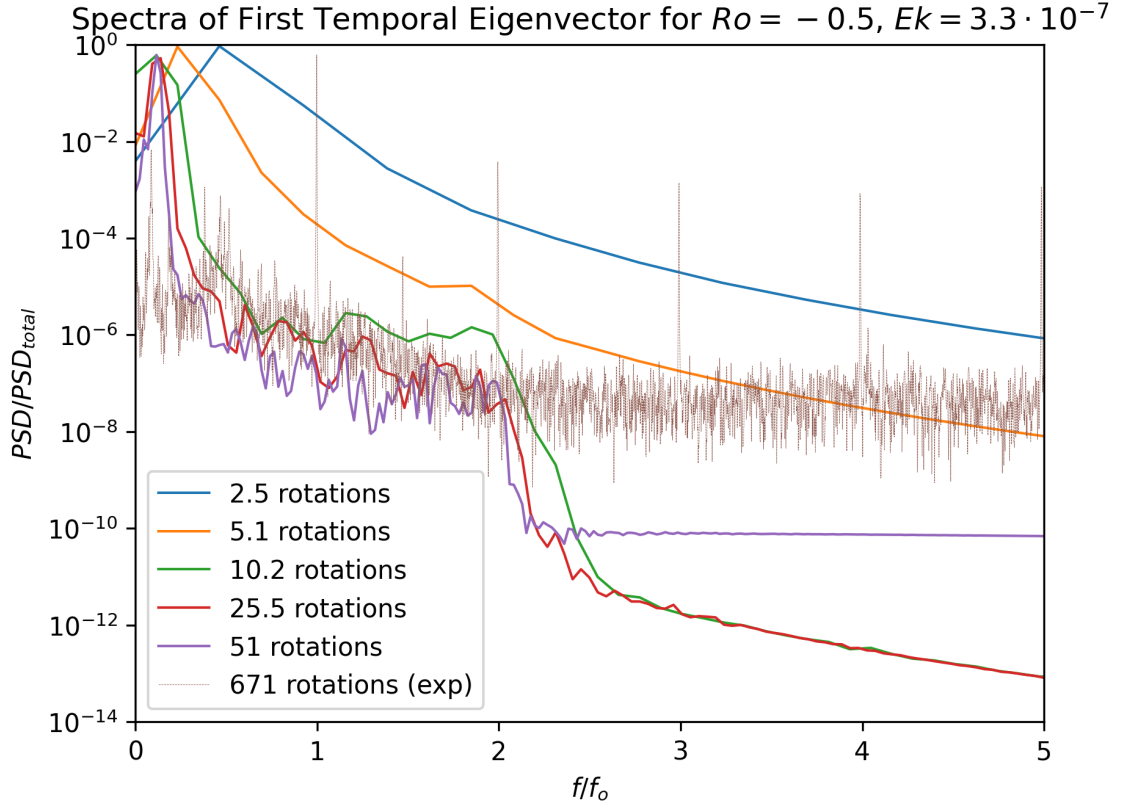


Figure 3.7: Spectra of first eigenvector for simulation and experimental Data of $Ro = -.5$, $\Lambda = 0.055$, $Ek = 3.3 \cdot 10^{-7}$. This plot include different lengths of simulation data to establish the appropriate amount of samples needed to compare to the experiment.

The following subplots in Fig. 3.8 are the eigenvectors corresponding to the 6 largest eigenvalues in order. As was seen from the eigenvalues in Fig. 3.6, the first 2 eigenvectors distinctly appear as a pair of out-of-phase waves.

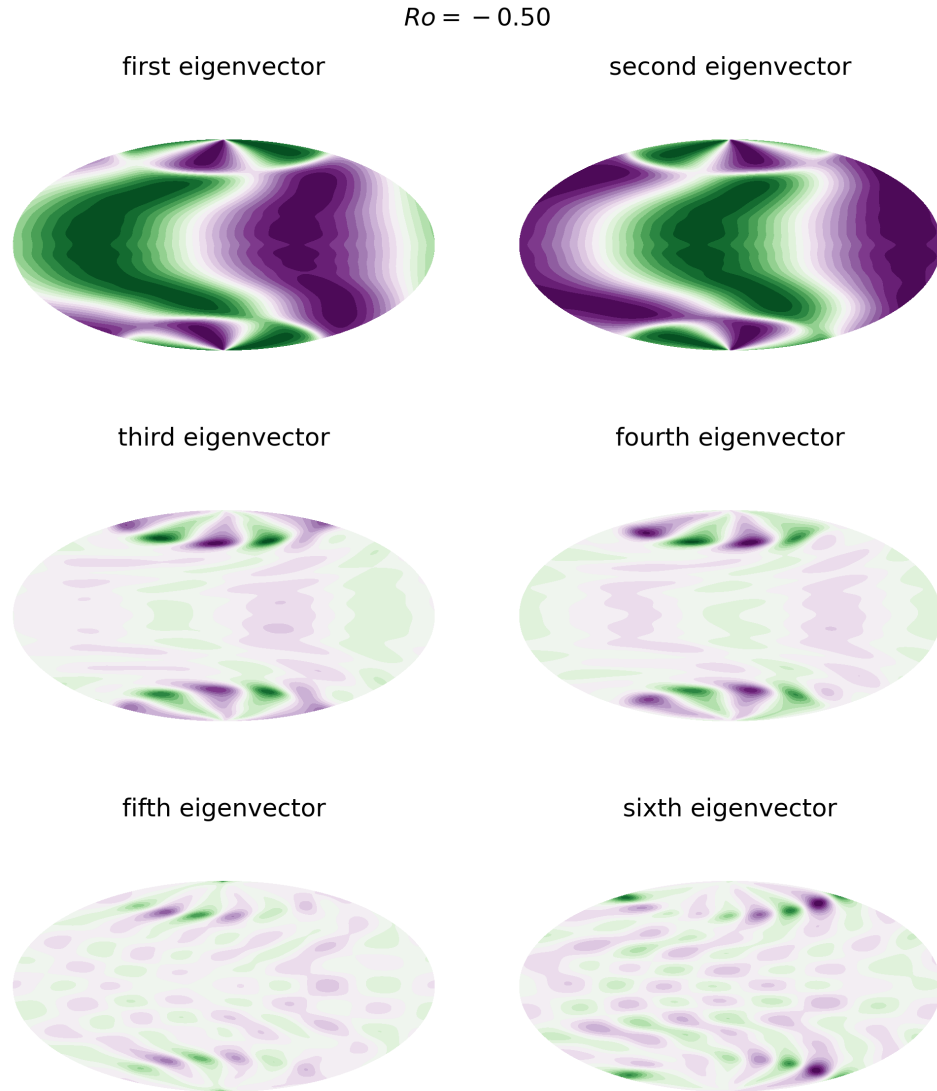


Figure 3.8: Simulation eigenvectors corresponding to the largest 6 eigenvalues for $Ro = -.5$, $\Lambda = 0.055$, $Ek = 3.3 \cdot 10^{-7}$.

Further analysis of Fig. 3.8, in the form of the projection strength maps of Fig. 3.9 shows there is another pair in the third and fourth eigenvector. The main pair maps onto the spherical harmonics basis of $(m, \ell) = (1, 5) \& (1, 1)$. The third and fourth maps more weakly onto $(m, \ell) = (2, 4)$.

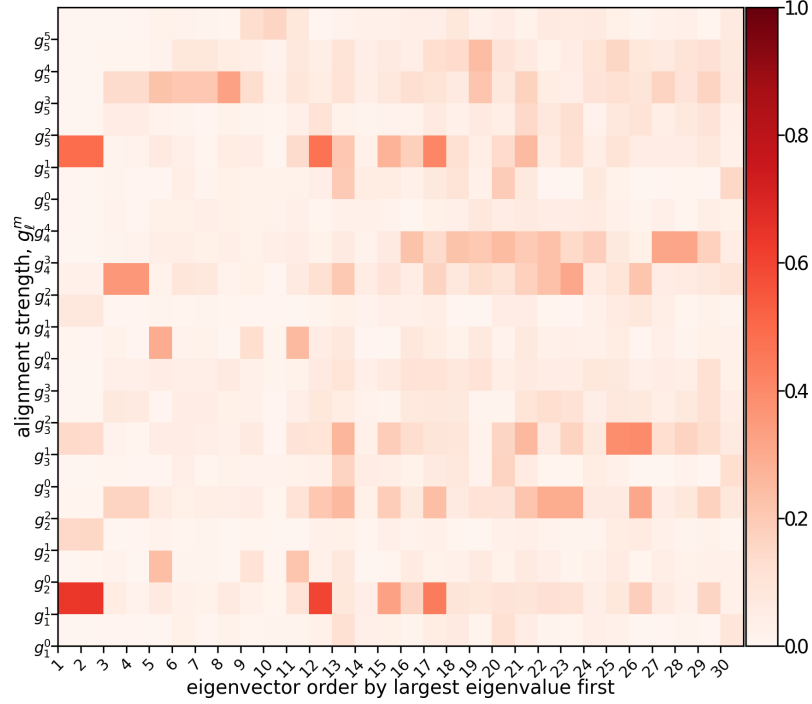


Figure 3.9: Projection strength map for simulation studies at $Ro = -0.5$, $\Lambda = 0.055$, $Ek = 3.3 \cdot 10^{-7}$. The map shows the alignment of the top 30 eigenvectors (in order of their corresponding eigenvalues) with the spherical harmonics basis up to $\ell_{max} = 5$.

3.4.1.3 Simulation $Ro = 1.75$, $\Lambda = 0.055$.

Figure 3.10 displays the eigenvalues and explained cumulative variance for several length of simulation runs and one experimental run. Based on the two longest simulation runs matching, it seems 51 rotations is sufficient for the analysis. The first two eigenvalues come as a pair and the 6 largest eigenvalues make up 41% of the cumulative variance for the simulation with 76 rotations. For the experiment with 987 rotations, the 6 largest eigenvalues make up 57% of the cumulative variance.

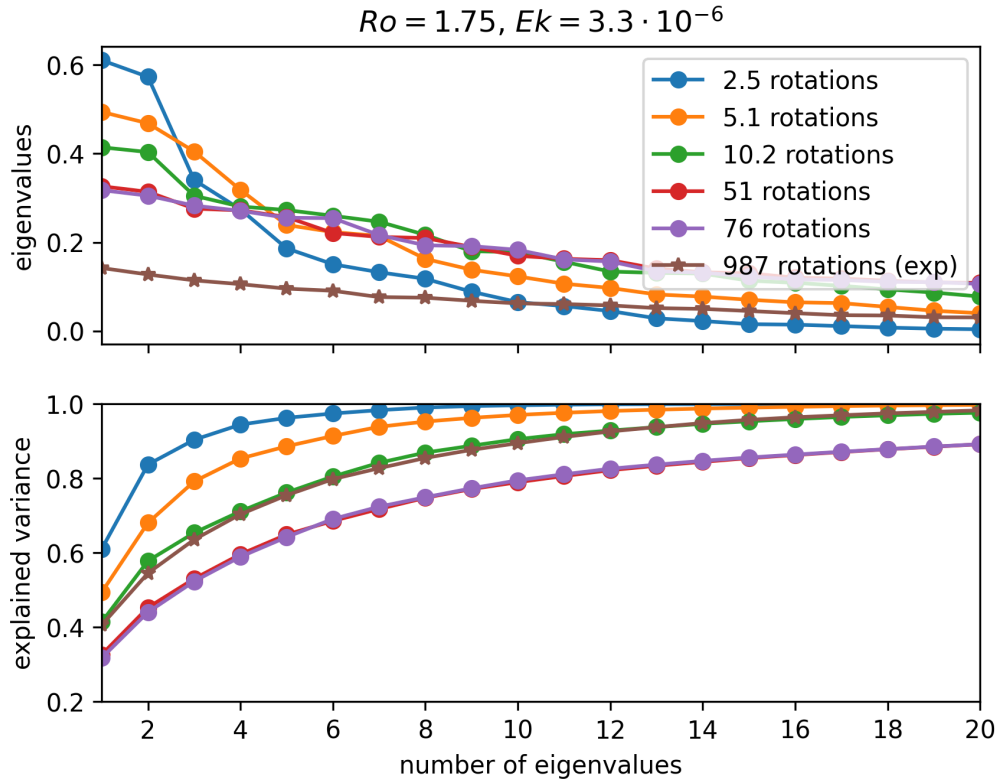


Figure 3.10: PCA eigenvalues and cumulative variance explained by the eigenvalues for simulation magnetic field data on a radial shell for parameters $Ro = 1.75$, $\Lambda = 0.055$, $Ek = 3.3 \cdot 10^{-6}$ for different test lengths. These are compared to the experimental data (from 31 measurements) in brown stars.

Figure 3.11 compares the temporal eigenvector corresponding to the largest eigenvalues for various lengths of simulations run and an experimental run. The first peak of the longest simulation run appears at $f/f_o = 0.1$ but does not precisely overlap with the peak from the experimental data.

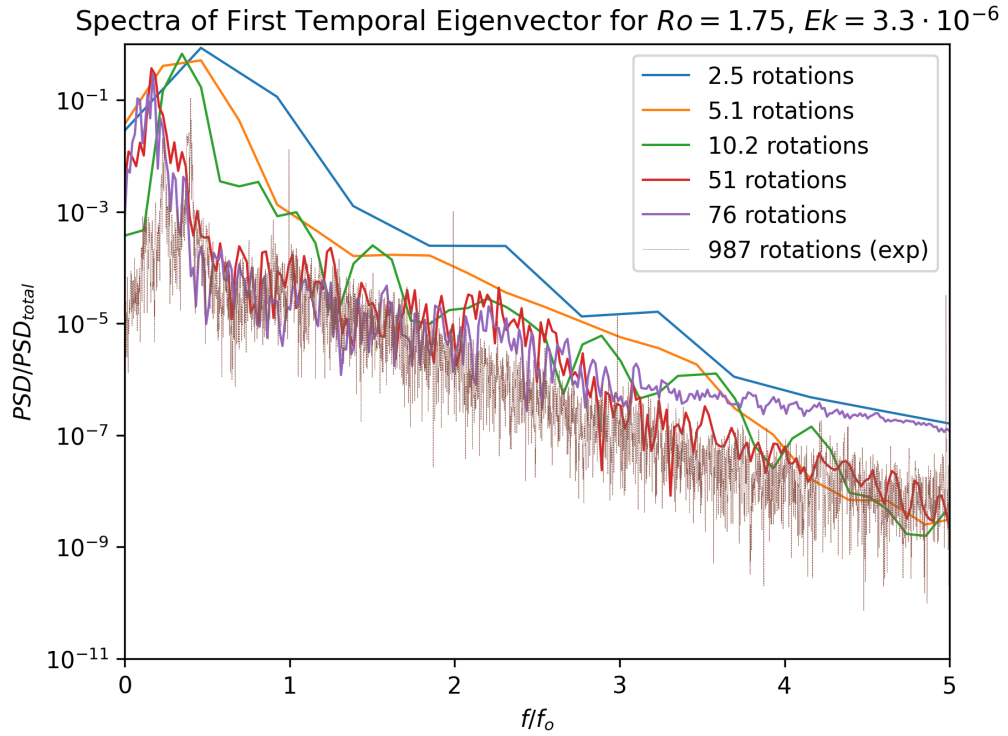


Figure 3.11: Spectra of first eigenvector for simulation and experimental Data of $Ro = 1.75$, $\Lambda = 0.055$, $Ek = 3.3 \cdot 10^{-6}$. This plot include different lengths of simulation data to establish the appropriate amount of samples needed to compare to the experiment.

The following subplots in Fig. 3.12 are the eigenvectors corresponding to the 6 largest eigenvalues in order. As was seen from the eigenvalues in Fig. 3.10, the first 2 eigenvectors appear as a pair of out-of-phase waves.

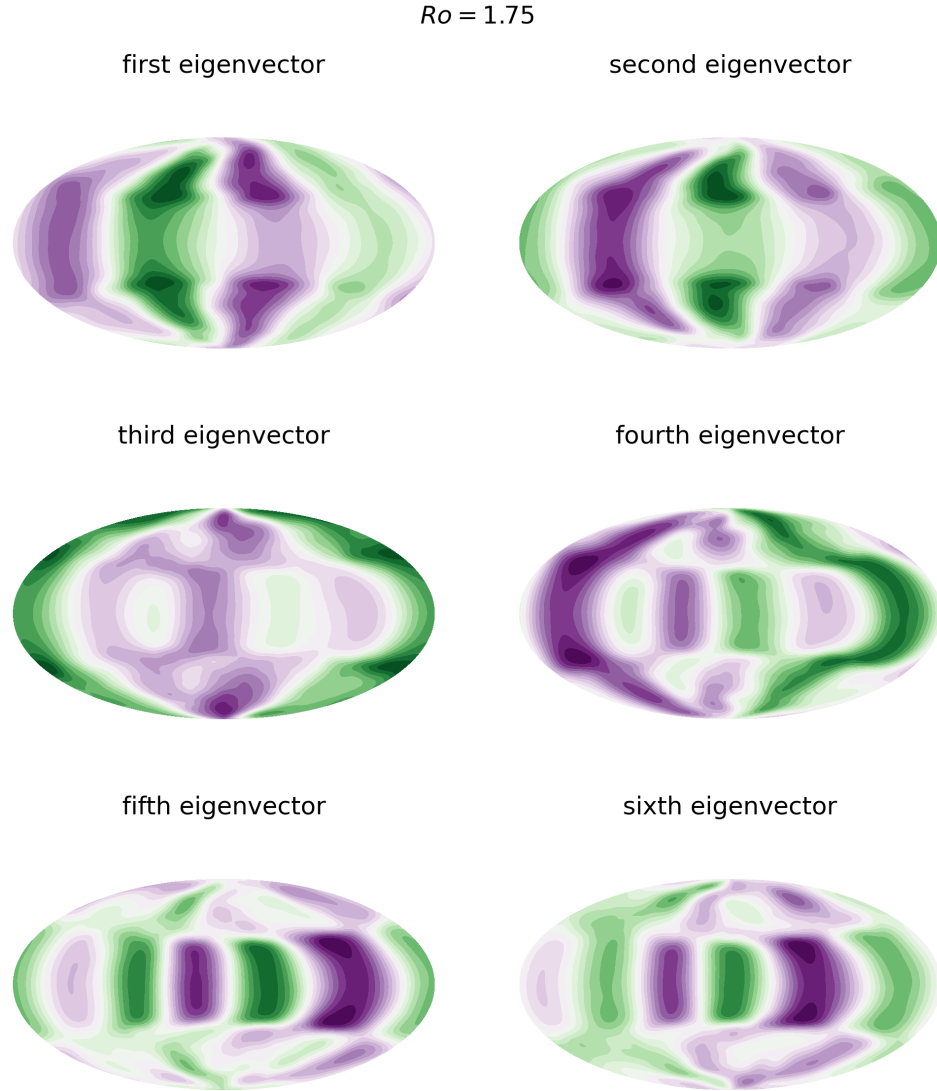


Figure 3.12: Simulation eigenvectors corresponding to the largest 6 eigenvalues for $Ro = 1.75$, $\Lambda = 0.055$, $Ek = 3.3 \cdot 10^{-6}$.

To search for pairs beyond the main two eigenvectors, we look at the projection strength map of Fig. 3.13. The main two eigenvectors appear to be a combination of $(m, \ell) = (2, 4)$ & $(2, 2)$. The fifth and sixth eigenvector make mostly of the spherical harmonic basis of $(m, \ell) = (3, 3)$. The 16th and 17th eigenvector make a pair from $(m, \ell) = (5, 5)$.

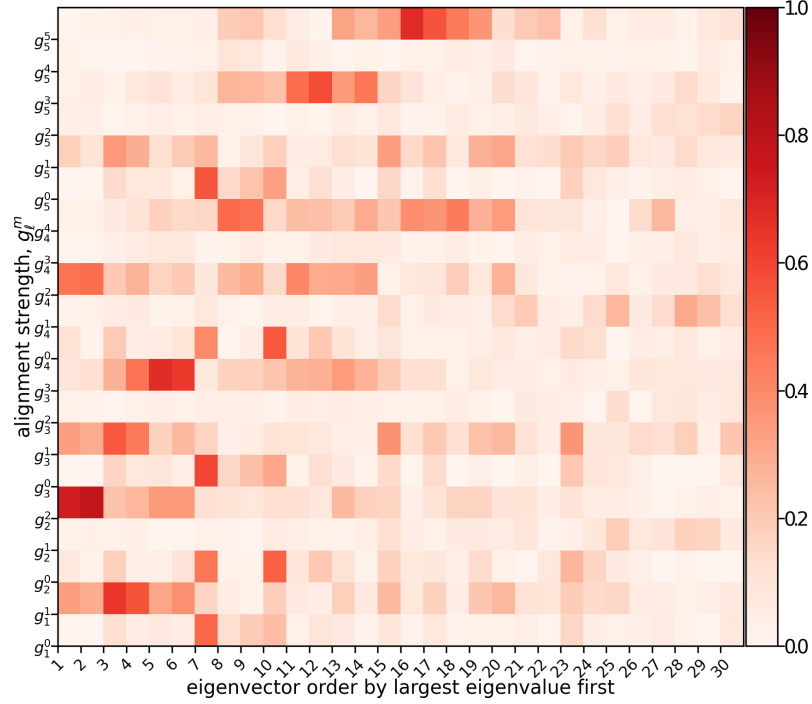


Figure 3.13: Projection strength map for simulation studies at $Ro = 1.75$, $\Lambda = 0.055$, $Ek = 3.3 \cdot 10^{-6}$. The map shows the alignment of the top 30 eigenvectors (in order of their corresponding eigenvalues) with the spherical harmonics basis up to $\ell_{max} = 5$.

3.4.1.4 Discussion

For $Ro = -1.75$ and based on the plot of the variance explained by the eigenvalues, in Fig. 3.2 we can interpret that 51 rotations is enough to properly compute the PCA of the system since it compare well with the experimental variance. Another justification 51 rotations are sufficient is from the first peak near $f/f_o = 0.1$ matching the experiment in the spectra of the first temporal eigenvector in Fig. 3.3. The largest peaks differ slightly between the experiment and simulation which could be due to noise in the eigenvectors. For $Ro = -0.5$, we look at Fig. 3.6, the eigenvalues don't match the experiment but appear to converge at 25.5 rotations. We can also see in the spectra of Fig. 3.7 there isn't much difference between the domi-

nant eigenvector of the PCA of 25.5 rotation and 51 rotations. The first peak, again roughly near $f/f_o = 0.1$ matches between the experiment and simulation. The most interesting thing about this plot is the noise floor of the experiment can be noted by comparing with the flat line of the simulation data for $f/f_o > 2.5$. For our high torque state at $Ro = 1.75$, Fig. 3.10 shows 51 rotations to be sufficient. Unlike the two inertial mode parameters, in Fig. 3.11 we see the first peak of the experiment spectra falls at a higher relative frequency than the simulations, likely indicating a greater noise level that is not captured in the simulation data. You might notice too that the change in the cumulative variance curve is smoother for the experiment likely due to noise in the experimental measurements. Note about all the eigenvalue plots is that the first two eigenvalues are close in value, indicating they are a pair of waves which can be seen in the eigenvector figures and projection strength maps.

For $Ro = -1.75$, Fig. 3.4 shows two pairs of eigenvectors: the first & second and the third & fourth. The pairs are out-of-phase versions of each other. We can observe the pairs in Fig. 3.5 they the first & second eigenvectors are strongly correlated with spherical harmonic $(m, \ell) = (1, 1)$. The third & fourth eigenvectors are strongly correlated with $(m, \ell) = (2, 3), (1, 3), \&(1, 5)$. The spherical harmonic $(1, 3)$ is hard to view from just the eigenvector plots without the projection strength map. For $Ro = -0.5$, Figs. 3.8 & 3.9, we can deduce the first two eigenvectors are a pair corresponding to $(m, \ell) = (1, 1)\&(1, 5)$. The spherical harmonics basis corresponding to $(1, 5)$ would not be able to be observed in the current experimental setup with only $\ell_{max} = 4$ attainable. For $Ro = 1.75$, Figs. 3.12 & 3.13 shows 2 pairs of eigenvectors in the first six eigenvectors. The first two are strongly correlated

with $(m, \ell) = (2, 4) \& (2, 2)$. The fifth & sixth eigenvector is strongly correlated with $(3, 3)$. Fig. 3.13 shows another pair of eigenvector corresponding to the 16th & 17th eigenvalues aligning with corresponding basis of $(5, 5)$. Again, our current experiment setup with 31 probes can only capture $\ell_{max}, m_{max} = 4$. These studies further motivate the need for more surface measurements on the experiment.

3.4.2 Comparison of experiment and simulation at hall probe locations

In this section, we explore the principal component analysis of the 2D PCA of the experiment's 31 probes placed on a radial shell of radius 1.5369 m or 1.0522 times the inner radius of the outer shell. The mean and eigenvectors are compared with the simulation data subsampled at the equivalent 31 locations of the Hall probes. The measurements are spatially sparse, yet temporally dense (so in this case $d \gg D$) so the SVD for PCA is implemented on $\mathbf{X}^T \mathbf{X}$.

3.4.2.1 Simulation vs. Experiment: $\mathbf{Ro} = -1.75$, $\mathbf{\Lambda} = 0.055$.

In Fig. 3.14 we compare the average radial magnetic field on the probe shell of the full resolution simulation and the experiment measurements for $Ro = -1.75$, $\Lambda = 0.055$, and $Ek = 3.3 \cdot 10^{-6}$. The 31 experimental measurements are shown in red and the python package tricontour is used to fill in the magnetic field between them. There is good agreement between the means which are predominantly the $(m, \ell) = (0, 2)$ spherical harmonics basis.

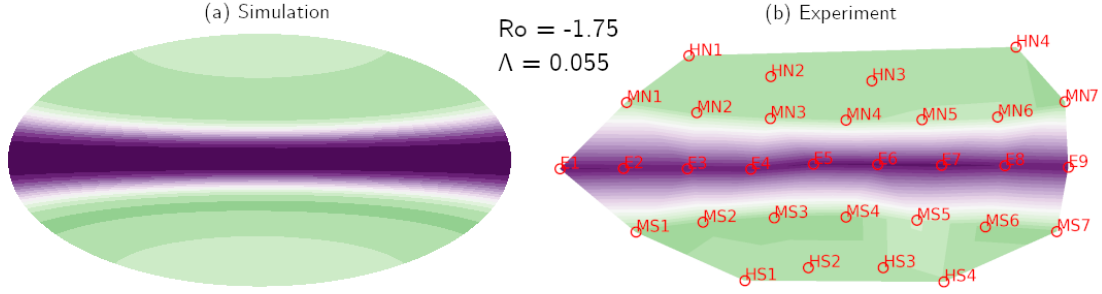


Figure 3.14: Mean magnetic field for $Ro = -1.75$ normalized by the spatial mean and standard deviation. Green corresponds to negative values and purple to positive values. Plot (a) show the magnetic field from the full 3D simulation and (b) shows the magnetic field from 31 points (labeled in red) observed in the experiment.

Figure 3.15 are projection strength plots of the subsampled simulations (at the equivalent 31 Hall probe locations are the experiment) and the experiments. Each of these plots separately categorizes the eigenvectors based on their alignment with the spherical harmonic basis (m, ℓ) with value g_ℓ^m . The two plots are displayed side by side to see how the main eigenvectors compare between the simulation and experiment as well as the spherical harmonic basis. The first two eigenvectors of the subsampled simulation make up a pair predominantly aligning with the $(m, \ell) = (2, 3)$ spherical harmonic basis. The first two main eigenvectors of the experiment also make up a pair but contrast with the simulation since they are a combination of $(m, \ell) = (1, 4), (1, 3) \& (1, 5)$. The third & fourth eigenvectors of the subsampled simulation make up a pair predominantly aligning with the $(m, \ell) = (1, 1)$ spherical harmonic basis. The third & fourth eigenvectors of the experiment also make up a pair but contrast with the simulation since they are a combination of $(m, \ell) = (1, 3), (1, 1), (1, 4), \& (1, 5)$. A few other pairs are distinguishable including the 6th & 7th eigenvectors of the experiment which are predominantly made of $(m, \ell) = (1, 1)$

spherical basis.

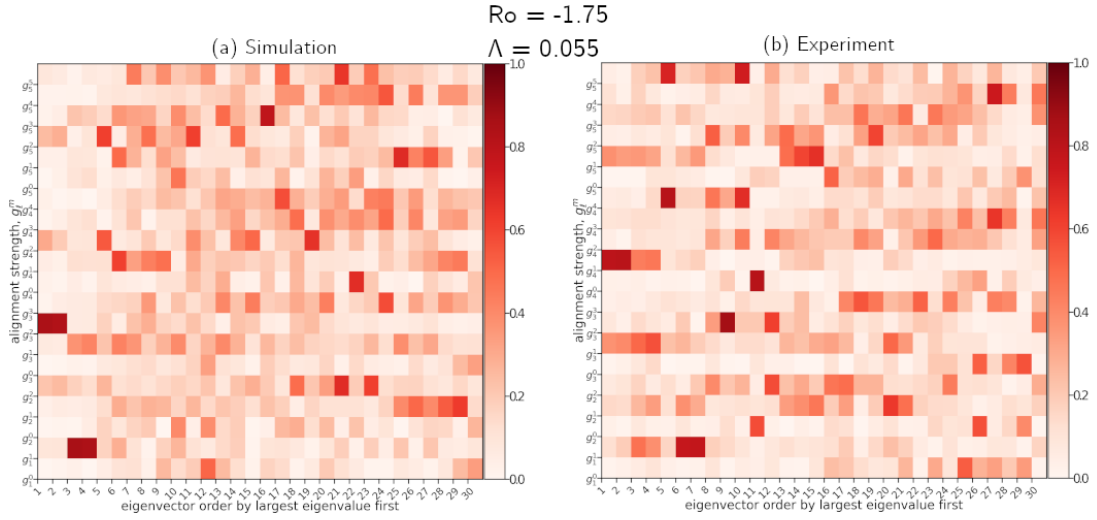


Figure 3.15: Projection strength map for subsampled simulation studies at $Ro = -1.75$, $\Lambda = 0.055$, $Ek = 3.3 \cdot 10^{-6}$ vs. experimental studies. The map shows the alignment of the top 30 eigenvectors (in order of their corresponding eigenvalues) with the spherical harmonics basis up to $\ell_{max} = 5$.

3.4.2.2 Simulation vs. Experiment: $Ro = -0.5$, $\Lambda = 0.055$.

In Fig. 3.16 we compare the average radial magnetic field on the probe shell of the full resolution simulation and the experiment measurements for $Ro = -0.5$, $\Lambda = 0.055$, and $Ek = 3.3 \cdot 10^{-7}$. The 31 experimental measurements are shown in red and the python package tricontour is used to fill in the magnetic field between them. Again, there is good agreement between the means which are predominantly the $(m, \ell) = (0, 2)$ spherical harmonics basis.

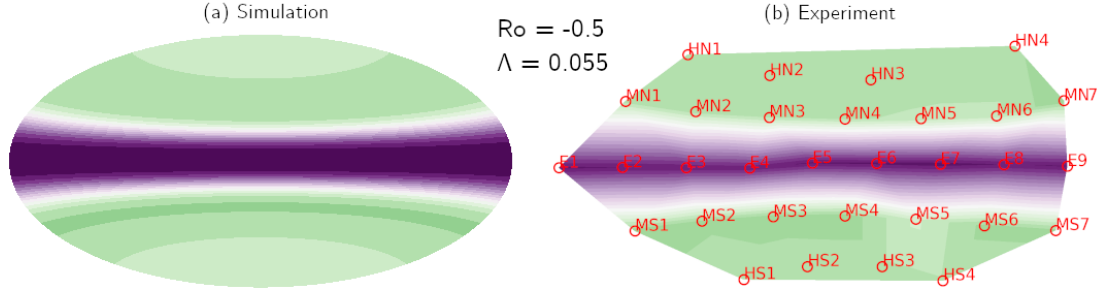


Figure 3.16: Mean magnetic field for $Ro = -0.5$ normalized by the spatial mean and standard deviation. Green corresponds to negative values and purple to positive values. Plot (a) show the magnetic field from the full 3D simulation and (b) shows the magnetic field from 31 points (labeled in red) observed in the experiment.

Figure 3.17 are projection strength plots of the subsampled simulations and the experiments. Each of these plots separately categorizes the eigenvectors based on their alignment with the spherical harmonic basis (m, ℓ) with value g_ℓ^m . I look for pairs of eigenvectors since wave as intrinsic to the MHD system. In the subsampled simulation there is strong alignment of the main two eigenvectors with $(m, \ell) = (1, 1)$ spherical harmonic basis and weaker alignment with $(1, 5)$ & $(1, 4)$. Another pair then appears in the 4th & 5th eigenvectors which align with $(m, \ell) = (4, 4)$ & $(5, 5)$. Unfortunately, I do not see overlap with the pairs of the experiment. The first pair of eigenvectors as made up of a combination of $(1, 2)$, $(1, 3)$, $(1, 4)$, & $(1, 5)$.

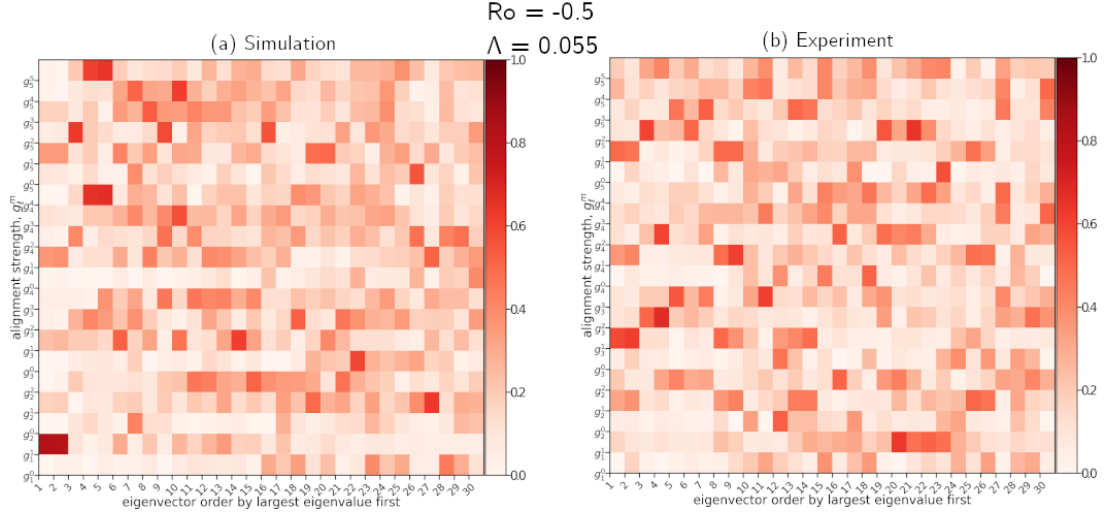


Figure 3.17: Projection strength map for subsampled simulation studies at $Ro = -0.5$, $\Lambda = 0.055$, $Ek = 3.3 \cdot 10^{-7}$ vs. experimental studies. The map shows the alignment of the top 30 eigenvectors (in order of their corresponding eigenvalues) with the spherical harmonics basis up to $\ell_{max} = 5$.

3.4.2.3 Simulation vs. Experiment: $Ro = 1.75$, $\Lambda = 0.055$.

In Fig. 3.18 we compare the average radial magnetic field on the probe shell of the full resolution simulation and the experiment measurements for $Ro = 1.75$, $\Lambda = 0.055$, and $Ek = 3.3 \cdot 10^{-6}$. The 31 experimental measurements are shown in red and the python package tricontour is used to fill in the magnetic field between them. Visually, there is good agreement between the means which are predominantly the $(m, \ell) = (0, 2)$ spherical harmonics basis. This is consistent across the changing Ro and Ek because it is the structure of the dipolar external magnetic field.

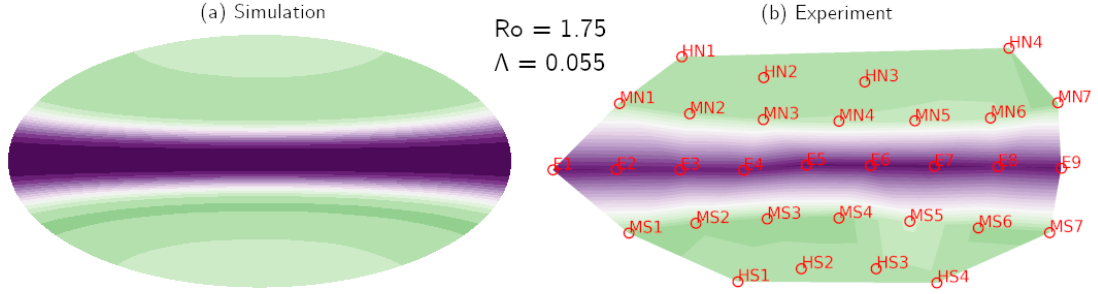


Figure 3.18: Mean magnetic field for $Ro = 1.75$ normalized by the spatial mean and standard deviation. Green corresponds to negative values and purple to positive values. Plot (a) show the magnetic field from the full 3D simulation and (b) shows the magnetic field from 31 points (labeled in red) observed in the experiment.

Figure 3.19 are projection strength plots of the subsampled simulations and the experiments. Each of these plots separately shows the alignment of the eigenvectors with the spherical harmonic basis (m, ℓ) with value g_ℓ^m . In the subsampled simulations, there is a pair of eigenvectors strongly aligned with the $(m, \ell) = (2, 2)$ spherical harmonic basis. The 3rd & 4th eigenvectors align with $(3, 3)$ and the 4th & 5th eigenvectors align with $(1, 1)$. A similar alignment appears in the experiment for the main 6 eigenvectors.

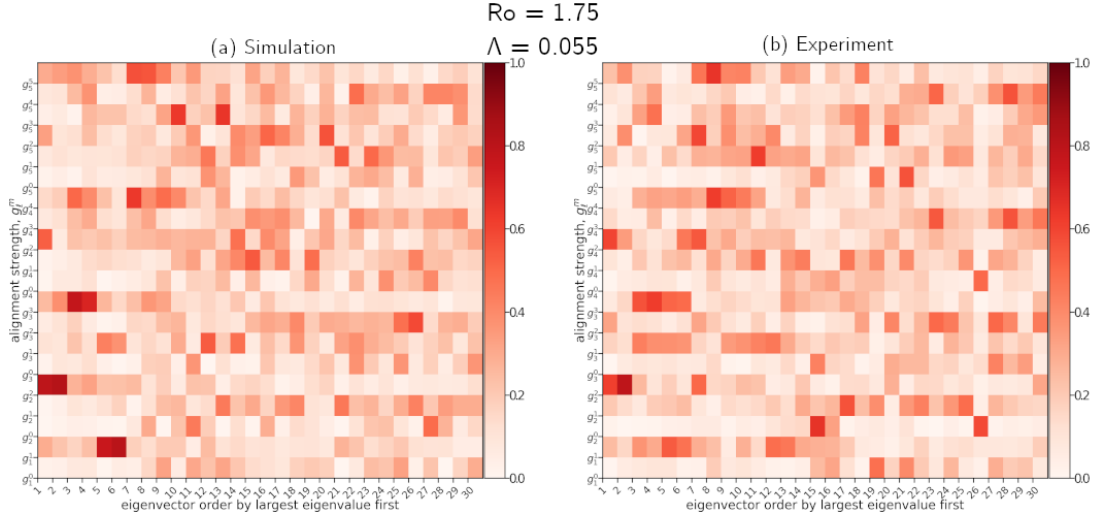


Figure 3.19: Projection strength map for subsampled simulation studies at $Ro = 1.75$, $\Lambda = 0.055$, $Ek = 3.3 \cdot 10^{-6}$ vs. experimental studies. The map shows the alignment of the top 30 eigenvectors (in order of their corresponding eigenvalues) with the spherical harmonics basis up to $\ell_{max} = 5$.

3.4.2.4 Discussion

Figure 3.18 shows the mean of the simulations data compared with the experimental data. Both plots have been separately normalized for comparison. It should be noted that the magnetic field in Figs. 3.14, 3.16, & 3.18 are roughly the same. This is because the mean field is predominantly the applied external field at $m = 0$.

There is not a strong comparison between the eigenvector of the simulation and the experiment, but there is some evidence their dynamics overlap. For $Ro = -1.75$ in the experimental analysis of (b) in Fig. 3.15, there are two pairs of eigenvectors (1 & 2 and 6 & 7) aligning strongly with (1, 4) and (1, 1) respectively. Interestingly, (1, 1) appears to strongly align with the third and fourth eigenvectors of in the map (b) of the subsample simulation data.

For $Ro = -0.5$, we see Fig. 3.17 has no overlap in the projection strength maps

of the simulation vs. experiment. However, the presence of values of $m, \ell \geq 4$ encourages us that more probes should be used to capture the higher m and ℓ . Also, since the first pair in the experiment is a combination of $(m, \ell) = (1, 2), (1, 3), (1, 4), \&(1, 5)$, we should consider more probes along the meridian to resolve higher degrees of ℓ . In Chapter 4, we will further investigate adding more probes in this proposed probe geometry.

For $Ro = 1.75$ and Fig. 3.19, we see both the experiment and simulation match well for their first four eigenvectors (somewhat for the 5th and 6th). The first & second eigenvectors align with $(2, 2)$ and the third & fourth eigenvectors align with $(3, 3)$, and then the fifth & sixth eigenvectors align with $(1, 1)$.

Chapter 4: New probe locations

4.1 Objective

In this chapter, we assess the potential locations for adding new probes to the current experimental configuration of Hall probes. The current setup has a sparse external probe configuration. The experiment has 31 probes measuring the radial component of the magnetic field on the same radial shell. The natural approach to get a bigger picture of the radial shell from the probe information is to use linear regression, in following Sec. 4.2, to map them onto the spherical harmonics. This creates a model which can evaluate the radial magnetic field component at any location. Therefore, using linear regression, at every timestep t , a set of Gauss coefficients is obtained to create our spherical harmonic model. For a particular location, the radial component of the magnetic field is collected to create what we assume to be the true distribution. Likewise, a distribution is collected by evaluating the spherical harmonic model at the same location as the true distribution over time. Then we measure the discrepancy of the true distribution and its spherical harmonic model distribution using JS divergence, total variation distance, and the Wasserstein distance. In the following studies I exclusively use simulation data in order to capture values at potential new probe locations. We can place 15 new

probes so I evaluate 3 different potential set ups. The results show the average and maximum distances and divergence for each of the three configurations. We suggest higher distance mean that the new probe location would improve on the accuracy if incorporated in the spherical harmonic model.

4.2 Linear regression

In this section, we review the current methods for estimating the Gauss coefficients from the raw magnetic field using the least-squares approach. We assume that the unbiased data from the 31 Hall probes measures the r-components of the magnetic field via the finite sum in Eq. (3.3). In this sum, we select $\ell_{\max} = 4$ since we estimate $\ell_{\max}(\ell_{\max} + 2) = 24$ coefficients in the spherical harmonics expansion. For 31 Hall probes, this yields an overdetermined linear system which can be solved and allows us to omit up to 7 hall probe measurements if we choose to. Note: If we want to use $\ell_{\max} = 5$ we need at least 4 more Hall probes. To begin, we generate a basis of Schmidt semi-normalized associated Legendre polynomials $P_{\ell}^m(\cos \theta)$ evaluated at the colatitude, θ , of the probe locations. These are multiplied by either $\sin(m\varphi)$ or $\cos(m\varphi)$ at each hall probe location φ and multiplied by the factor $\ell(\ell + 1) \left(\frac{r_o}{r}\right)^{\ell+2}$ where $r_o = 1$. In this example, we generate a 31 by 24 matrix \mathbf{K} whose rows are the individual pieces of the sum excluding the Gauss coefficients from Eq. (3.3) evaluated at each of the 31 probe positions.

By using the linear regression approach we wish to estimate the Gauss coefficients \mathbf{g} in $\mathbf{d} = \mathbf{K}\mathbf{g}$ where \mathbf{d} is a vector containing the Hall probe measurements of

the r-components of the magnetic field at some time. Our goal is to minimize the following cost function with respect to the Gauss coefficients \mathbf{g} ,

$$\mathcal{J}(\mathbf{g}) = (\mathbf{d} - \mathbf{K}\mathbf{g})^T \mathbf{W}^{-1} (\mathbf{d} - \mathbf{K}\mathbf{g}). \quad (4.1)$$

In this cost function, \mathbf{W} is the weight given to each datum according to the covariance describing the accuracy of each hall probe measurement. Because we assume that errors on different Hall probes are uncorrelated, it is simply a diagonal matrix of the variances. Now we take the derivative of \mathcal{J} with respect to \mathbf{g} and find $\hat{\mathbf{g}}$ such that,

$$\left. \frac{\partial \mathcal{J}}{\partial \mathbf{g}} \right|_{\mathbf{g}=\hat{\mathbf{g}}} = 0. \quad (4.2)$$

To help with taking the derivative note the expansion is

$$\mathcal{J}(\mathbf{g}) = \mathbf{d}^T \mathbf{W}^{-1} \mathbf{d} - \mathbf{g}^T \mathbf{K}^T \mathbf{W}^{-1} \mathbf{d} - \mathbf{d}^T \mathbf{W}^{-1} \mathbf{K} \mathbf{g} + \mathbf{g}^T \mathbf{K}^T \mathbf{W}^{-1} \mathbf{K} \mathbf{g}, \quad (4.3)$$

$\mathbf{W}^{-1} = \mathbf{W}^{-T}$, each of the terms are equal to a some scalar α with $\alpha^T = \alpha$, and the derivative of a quadratic, $\alpha = \mathbf{m}^T \mathbf{B} \mathbf{m}$, is

$$\frac{\partial \alpha}{\partial \mathbf{m}} = \mathbf{m}^T (\mathbf{B} + \mathbf{B}^T). \quad (4.4)$$

So then

$$\frac{\partial \mathcal{J}}{\partial \mathbf{g}} = -2\mathbf{d}^T \mathbf{W}^{-1} \mathbf{K} + 2\mathbf{g}^T \mathbf{K}^T \mathbf{W}^{-1} \mathbf{K}, \quad (4.5)$$

$$0 = -\mathbf{d}^T \mathbf{W}^{-1} \mathbf{K} + \mathbf{g}^T \mathbf{K}^T \mathbf{W}^{-1} \mathbf{K} + \lambda \mathbf{g}^T \mathbf{D}, \quad (4.6)$$

$$\mathbf{d}^T \mathbf{W}^{-1} \mathbf{K} = \mathbf{g}^T (\mathbf{K}^T \mathbf{W}^{-1} \mathbf{K}), \quad (4.7)$$

and

$$\boxed{\mathbf{g} = (\mathbf{K}^T \mathbf{W}^{-1} \mathbf{K})^{-1} \mathbf{K}^T \mathbf{W}^{-1} \mathbf{d}}. \quad (4.8)$$

In the special case of $\mathbf{W} = \mathbb{I}$ then Eq. (4.8) simplifies to

$$\hat{\mathbf{g}} = (\mathbf{K}^T \mathbf{K})^{-1} \mathbf{K}^T \mathbf{d}. \quad (4.9)$$

4.3 Information theory

Information theory allows us to determine how much information is necessary to transmit a message. Particularly, we are interested in how many probes and what positioning best captures the behavior of the magnetic field in the experiment. Our approach uses information theory and simulations to justify the placement and number of new probes added to the experiment.

In general, a system might have levels of certainty and uncertainty in different locations. For example, a fair coin will flip and give us a 50% probability of heads and a 50% probability of tails. The outcome will then have some level of uncertainty –will it be heads or tails? However what if we have a biased coin that has a 100%

chance of landing on heads and 0% chance of landing on tails? We will always expect this coin to land on heads with absolute certainty. There is no surprise in it landing on heads and never on tails. A measure of the surprise in such a probabilistic outcome, x can be mathematically described by the entropy defined as

$$H(P) = - \int p(x) \log p(x) dx = E[\log p], \quad (4.10)$$

for a continuous probability distribution, and for a discrete probability distribution it is the sum,

$$H(P) = - \sum_{x \in X} p(x) \log p(x) = E[\log p], \quad (4.11)$$

When the log function is base e , the information is measured in “nats” and when log base 2 is used, the information is measured in “bits”. For our biased coin (always heads) example,

$$\begin{aligned} H &= - (p(0) \log p(0) + p(1) \log(p(1))) \\ &= - (0 \log 0 + 1 \log(1)) = 0. \end{aligned}$$

i.e., there is no surprise regarding the outcome of a coin toss. For our fair coin

example,

$$\begin{aligned} H &= -(p(0) \log p(0) + p(1) \log(p(1))) \\ &= -\left(\frac{1}{2} \log\left(\frac{1}{2}\right) + \frac{1}{2} \log\left(\frac{1}{2}\right)\right) \\ &= -\left(\frac{1}{2}(-1) + \frac{1}{2}(-1)\right) = 1. \end{aligned}$$

The result is nonzero which means there is entropy or some element of surprise to the outcome of our system. This fair coin has a uniform distribution of possible outcomes, which is the maximum uncertainty or maximum entropy we can get out of this particular system.

We can also compute the cross-entropy which computes the number of bits it takes to represent the average event from one true distribution $p(x)$ compared to another model distribution $q(x)$. Such a cross-entropy is defined as

$$H_P(Q) = - \sum_{x \in X} p(x) \log q(x). \quad (4.12)$$

An important quantification of information is the Kullback-Leibler (KL) divergence [62, 63] or “information gain” that measures how much more information there is in a distribution $p(x)$ compared to a distribution $q(x)$. The KL divergence is defined as

$$KL(p(x)||q(x)) = \sum_{x \in X} p(x) \log \frac{p(x)}{q(x)}, \quad (4.13)$$

where $p(x)$ is the true distribution and $q(x)$ is the model distribution. Though this quantity returns a non-negative value, it is not a metric distance because it is asymmetric with respect to the two arguments. It also requires that $q(x) > 0$ whenever $p(x) > 0$. A symmetrized version is called the Jensen-Shannon divergence [64]. Despite not being a proper metric, it is widely used because KL divergence can be described as relative entropy,

$$KL(p(x)||q(x)) = H_P(Q) - H(P) \quad (4.14)$$

To see how they are the same definition, plug in Eqs. (4.11) & (4.12)

$$\begin{aligned} KL(p(x)||q(x)) &= H_P(Q) - H(P), \\ &= \left(- \sum_{x \in X} p(x) \log q(x) \right) - \left(- \sum_{x \in X} p(x) \log p(x) \right), \\ &= \sum_{x \in X} -p(x) \log q(x) + p(x) \log p(x), \\ &= \sum_{x \in X} p(x) (-\log q(x) + \log p(x)), \\ &= \sum_{x \in X} p(x) \log \frac{p(x)}{q(x)}. \end{aligned}$$

When we look at the three-meter simulation data sets as probabilities, like the coin toss, they are discrete probabilities represented by snapshots of the radial component of the magnetic field at the probe location over a time period, $b_r(r_i, \phi_i, \theta_i, t_n)$ where n is an integer from $(0, N)$ and N is the total number of events in the tested

sample space. The index i is the location where we wish to test the entropy of the probe. In theory, the evolution, which is based off a continuous system of partial differential equations (Eqs. (1.3) and (1.2)) would be a continuous probability distribution. However, since it is discretized and solved numerically it is represented as a discrete probability distribution. To compute the information gain, we must assign a true probability distribution $p(b_r(r_i, \phi_i, \theta_i, t_n))$ and a model probability distribution $q(b_r(r_i, \phi_i, \theta_i, t_n))$. We build a model with the current 31 probes which measure the radial component of the magnetic field $b_r(r, \theta, \phi)$. The 31 current probes are mapped onto Schmidt semi-normalized associated Legendre polynomials evaluated at their positions, up to a maximum degree ℓ_{\max} . At each time t , the least squares approach outlined in (section 4.2) linearly solves for Gauss coefficients. Then we have a model for new probe positions: the sum of the Gauss coefficients and the Legendre polynomials evaluated at the new probe location can compute an estimate of $b_r(r_i, \phi_i, \theta_i, \mathbf{t})$. From this we determine the model distribution $q(b_r(r_i, \phi_i, \theta_i, t_n))$ over samples from snapshots in time. The model is then compared to the true distribution $p(b_r(r_i, \phi_i, \theta_i, \mathbf{t}))$ which is the $b_r(r_i, \phi_i, \theta_i, \mathbf{t})$ at the new probe over samples from snapshots in time. We denote each new potential probe by an index i and its relative entropy,

$$KL(p(b_r(r_i, \phi_i, \theta_i, t)) || q(b_r(r_i, \phi_i, \theta_i, t))) = \sum_{n=0}^N p(b_r(r_i, \phi_i, \theta_i, t_n)) \log \frac{p(b_r(r_i, \phi_i, \theta_i, t_n))}{q(b_r(r_i, \phi_i, \theta_i, t_n))}. \quad (4.15)$$

A proper measure can be found in the Jensen-Shannon (JS) divergence [64]. Let's define the pointwise mean of probabilities to be $m(x) = \frac{1}{2}(p(x) + q(x))$, then the

definition is

$$JS(p(x)||q(x)) = \frac{1}{2}KL(p(x)||m(x)) + \frac{1}{2}KL(q(x)||m(x)) \quad (4.16)$$

or in our specific case,

$$\begin{aligned} JS(p(b_r(r_i, \phi_i, \theta_i, t))||q(b_r(r_i, \phi_i, \theta_i, t))) = & \quad (4.17) \\ & \frac{1}{2}KL(p(b_r(r_i, \phi_i, \theta_i, t))||m(b_r(r_i, \phi_i, \theta_i, t))) \\ & + \frac{1}{2}KL(q(b_r(r_i, \phi_i, \theta_i, t))||m(b_r(r_i, \phi_i, \theta_i, t))). \end{aligned}$$

These two measures of surprise are used to determine the amount of surprise of the i^{th} additional probe added to the system at the location (r_i, ϕ_i, θ_i) . Probe positions with more surprise (entropy closer to 1) are ranked higher than those evaluated to be closer to 0 (meaning $q(b_r(r_i, \phi_i, \theta_i, t_n))$ is the same as $p(b_r(r_i, \phi_i, \theta_i, t_n))$ and there's no information gain). The benefit of the JS divergence over the KL divergence is it is symmetrized and smooth. Also, in practical implementation, the KL divergence can only be evaluated for $x \in X$ when $q(x)$ is nonzero. The JS divergence does not have restrictions. (Note if $p(x) = 0$ and we have $p(x) \log \frac{p(x)}{m(x)}$, the limit as $x \rightarrow 0$ is 0 since $p(x)$ converges faster to 0 than $\log \frac{p(x)}{m(x)}$ to $-\inf$).

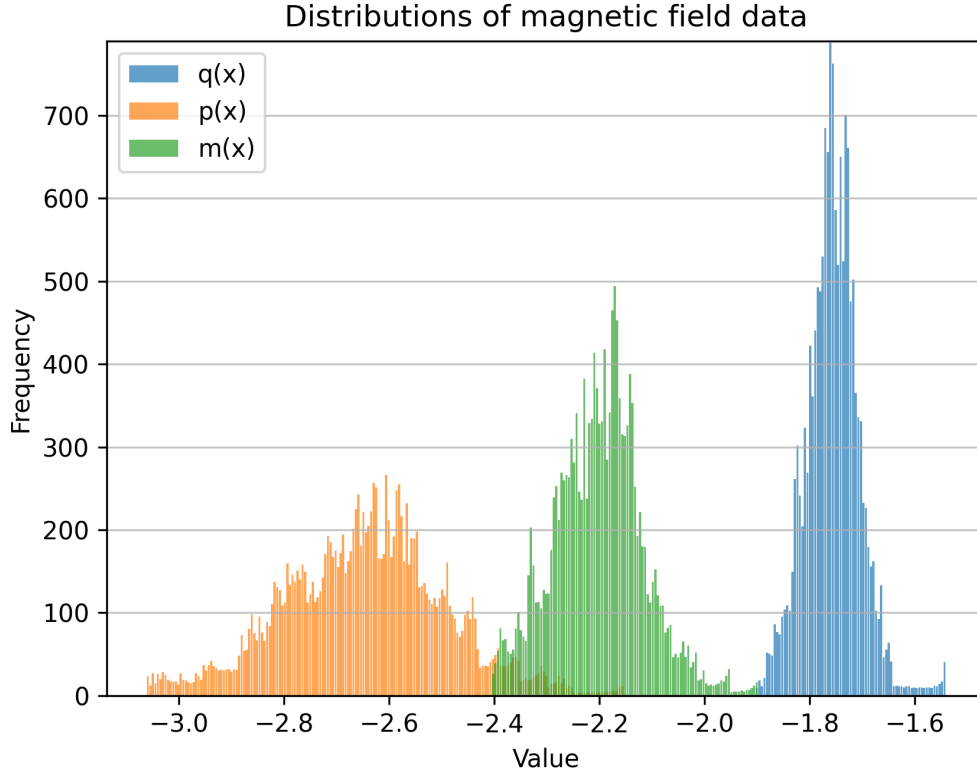


Figure 4.1: For parameters $Ro = 1.75$ and $Le = 0.0013$, the figure shows histograms of the radial magnetic field simulation data $p(x)$, the spherical harmonics model $q(x)$, and their pointwise mean $m(x)$ at the location of one probe. From the figure, we can see the portion of information left out of the JS divergence calculation due to $p(x)$ and $q(x)$ not overlapping $m(x)$.

The JS divergence is a proper measure, but for distributions that do not overlap, the manner that it measures can miss some portion of the information (parts of $p(x)$ or $q(x)$ not overlapping of $m(x)$) used to assess the measure (see Fig. 4.1). KL divergence also has this disadvantage. One option could be to assume $p(x)$ and $q(x)$ are normal distributions, normalize by their mean and standard deviation, and calculate the KL and JS divergence. Then, we could incorporate the difference in the original means to the calculated entropies. However, this method is ad hoc, since there is no a priori reason to expect the distributions to be Gaussian. A

preferable measure to the JS divergence that is not complicated by non-overlapping distributions would be the Wasserstein distance.

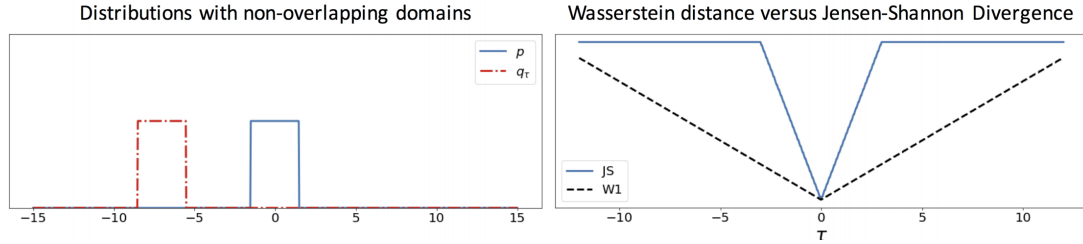


Figure 4.2: Figure 6 from [65] showing in blue the uniform distribution p and in dashed red the uniform distribution $q(x) = (x - \tau)$. The right plot shows the Wasserstein distance, $W_1(p||q_\tau)$, in black and the JS divergence $JS(p||q_\tau)$

Figure 4.2 is Figure 6 from [65] which shows two nonoverlapping uniform distributions on the left. In the right plot the Wasserstein distance and JS divergence are calculated as a function of τ , that is, how far the uniform distributions are separated. With the JS divergence, there is a τ (here around 2.5) in which for any large τ , the measure loses all meaning since $m(x)$ no longer overlaps with $p(x)$ or $q(x)$. The Wasserstein distance provides a useful measure without limitations on the distance of the distributions.

4.4 Distance functions

In this section, I will define the Wasserstein distance along with the more straightforward total variation distance that will be used to assess how well the spherical harmonic model encodes the magnetic field at a particular of location. Instead of quantifying how much ‘surprise’ is captured, the goal is to compute the distance of the model prediction from the true observation. We assume that lo-

cations resulting in higher values for this distance would be better candidates for new probe placements because they should improve the spherical harmonic model estimation.

Total variation (TV) distance [66] is a measure of the maximum distance between two probabilities assigned to a single event by their distributions. The total variation distance of probability measures can be defined as

$$TV(p(x), q(x)) = \frac{1}{2} \sum_{x \in X} |p(x) - q(x)| = \frac{1}{2} L_1(p, q) \quad (4.18)$$

where L_1 denotes the L_1 -norm.

Let's define the Wasserstein (W1) distance [67, 68]. Also known as the Kantorovich-Rubinstein metric [69], it is also sometimes called Earth Mover's distance [70] despite a slight difference in their definitions. Like KL and JS divergence, the Earth Mover's distance is based on physical concepts. Instead of entropy, it is computed as the minimum amount of work required to transform our raw probe measurements to the spherical harmonic model estimates. More specifically, it is a measure of the amount of distribution weight that must be moved, times the distance it has to be moved. Mathematically, W_1 can be defined as

$$W1(p, q) = \sup \left\{ \left| \int h dp - \int h dq \right| : \|h\|_L \leq 1 \right\} \quad (4.19)$$

with the supremum being taken over all h satisfying the Lipschitz condition $|h(x) - h(y)| \leq \delta(x, y)$ where δ is metric on our domain.

4.5 Approach

We assess the potential of a new probe location using three possible measures: JS divergence, TV distance, and the W1 distance. We exclusively use simulation data in order to capture values at new probe locations. The experiment currently has 31 probes measuring the radial component of the magnetic field on a radial shell. The best way to get a higher resolution depiction of the radial shell from the spatially sparse probe information is to use linear regression (see section 4.2) to map them onto the spherical harmonics. This creates a model which can be evaluated at any shell location. We will compare the radial magnetic field data from the probes with the spherical harmonic magnetic field data.

We consider adding up to 15 new probe locations. Prior to assessing the measures, the reasons for choosing certain locations are to i) reduce the condition number in the linear regression model, ii) to target areas of rapid change in magnetic field value (e.g. positive to negative at the TC), and iii) to elucidate higher wavenumbers m in our analysis by adding more on the equator. The tangent cylinder lies at the surface at 0.3 radians and 2.8 radians. Due to physical restrictions in the experiment, only polar angles $0.56 < \theta < 2.88$ radians are possible on the outer sphere, or $0.090 < \theta < 0.46$ radians on the lid. Figure 4.3 shows some suggested new probes placements by team members and affiliates.

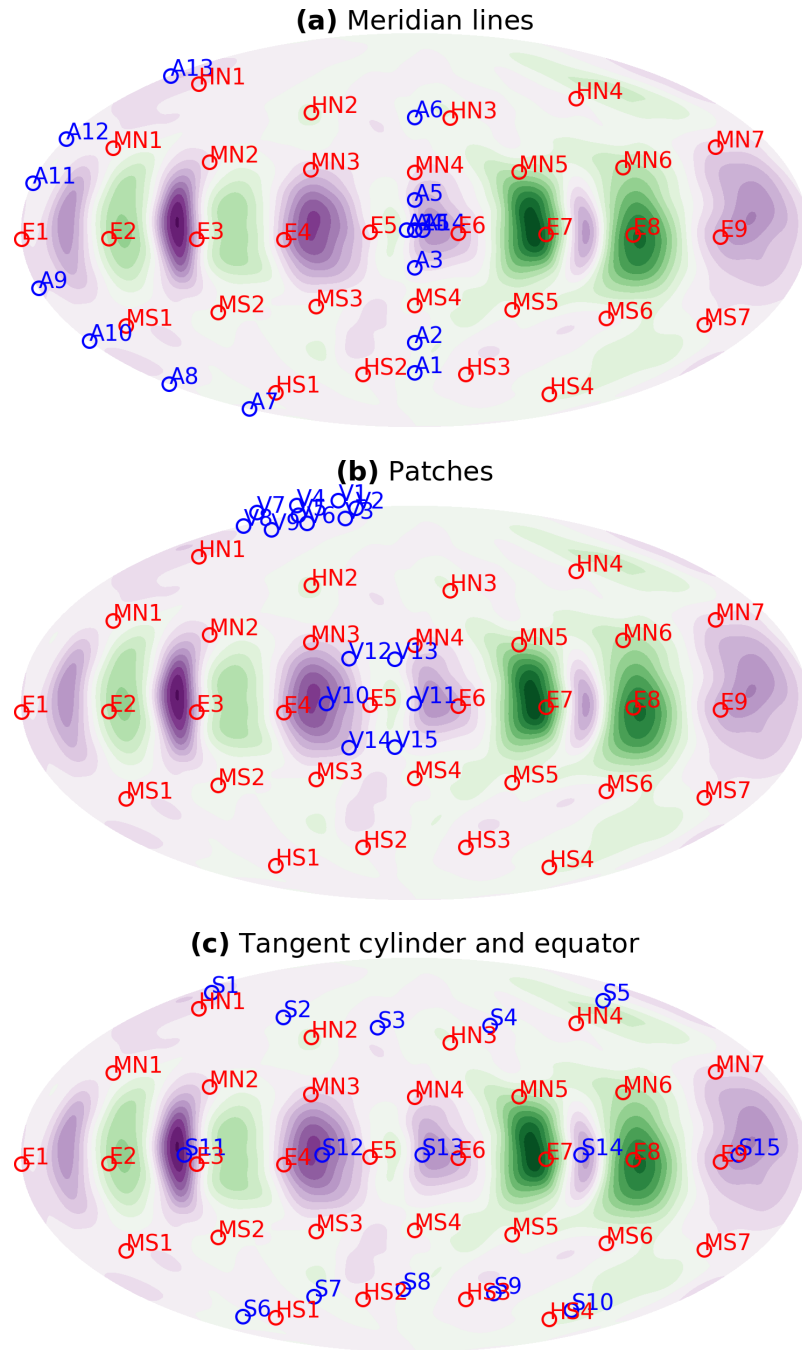


Figure 4.3: Suggested probes locations by team members and affiliates. The contour plots are over a shell of radial magnetic field components with the mean removed. Original probes are in red and suggested probes are in blue. The probes in **(a)** are two arrays of meridian probes with two points added off the meridian at the equator (suggested by Artur Perevelov), **(b)** are two patches similar to the patches taken in satellite imaging (suggested by Vedran Lekić), and **(c)** are more probes added at the equator and close to the tangent cylinder (suggested by the author).

The following analysis were performed on simulation runs of control parameters of $Ro = -1.75$, $\Lambda = 0.055$, and $Ek = 3.3 \cdot 10^{-6}$. Table 4.1 reflects the means of the scores for each type of measurement over the 15 suggested probe locations in each configuration. From this table, the meridian line configuration scores the highest in total variation distance with 2.65 and Wasserstein distance with 5.29.

Configuration	JS	TV	W1
Original	0.693	1.22	2.45
Meridian lines	0.693	2.65	5.29
Patches	0.693	2.19	4.39
Equator & TC	0.671	1.26	2.53

Table 4.1: For each configuration, the table shows the averages for each type of measurement. Tests were run by assessing the measure between the radial magnetic field data at the prospective probe location and comparing that with the spherical harmonic model (approximated from the original 31 probes) evaluate at the prospective probe location.

Table 4.2 now depicts the maximum values for each measure and their locations which can be seen on the subplots of Fig. 4.3. This table reveals that the maximum TV and W1 are comparable 3.99 and 7.97, respectively, for certain locations for the ‘meridian lines’ and ‘patches’ configurations. For the ‘patches’ configurations, there are two patches. The one closest to the pole has the highest score values. The ‘meridian lines’ configurations has the same scores on one of the meridian lines on the left side of the subplot.

Configuration	JS	TV	W1
Original	HS2, MS3, E5, MN2, HN2 (0.693)	E1 (3.99)	E1 (7.97)
Meridian lines	A1-A15 (0.693)	A7-A13 (3.99)	A7-A13 (7.97)
Patches	V1, V12, V14 (0.693)	V1, V2, V4, V5, V7, V8 (3.99)	V1, V2, V4, V5, V7, V8 (7.97)
Equator & TC	S1,S2 (0.693)	S1 (3.58)	S1 (7.15)

Table 4.2: For each configuration, the table shows the maximum values with the respective probe location for each type of measurement. Tests were run by assessing the measure between the radial magnetic field data at the prospective probe location and comparing that with the spherical harmonic model (approximated from the original 31 probes) evaluate at the prospective probe location.

4.6 Conclusion

The results of the single probe analysis favor the ‘meridian lines’ proposed geometry which has the highest average TV and W1 score (JS is an ineffective measure for our analysis). Part of the advantage of this setup it there are 3 additional probes placed along the equator as well. There should be $2m_{max} + 1$ probes along the equator. All the proposed geometries have at least 2 addition probes at the equator allowing for $m_{max} = 5$. The ‘patches’ setup is tied for the highest TV and W1 for the probes V1-V8 set near the pole. However, physical placement of these probes at the same radii (as used for the analysis) is not possible due to the experiment lid. Additional analysis would have to be performed knowing the physical radial distances V1-V8 could be placed on the lid. The next step would be to iteratively test the effect of adding the most favorable probes from the ‘meridian lines’ configuration. This should be done two ways: i) by obtaining new Gauss coefficients and computing the condition number and ii) by computing the W1 distance. The TV distance is somewhat redundant as it is a measure similar to W1

distance by definition.

Chapter 5: Machine Learning

5.1 Objective

The purpose of this chapter is to test whether machine learning tools can predict the magnetic field variations in time. Since the experiment can provide long time series of data without much storage or computation cost, we test our machine learning tools on experimental data. We use an experimental set from $Ro = -0.5$ and $\Lambda = 0.055$ for these studies. We intend to compare how well both reservoir computing (RC) and Long short-term memory (LSTM) network can perform on the data of 31 probes and on the Gauss coefficients computed for the probe data.

5.2 Theory

In this section we will go over two types of recurrent neural network (RNN). In its basic form, data is input into a neuron and activates it in two ways: i) one activation is passed forward through hidden layers and then output and ii) one activation is passed back to be re-input with the data from the next time sample. Essentially, the RNN has loops as seen in red in Fig. 5.1, in contrast to traditional feed-forward architectures used in the multi-layer perceptron and convolutional neural networks.

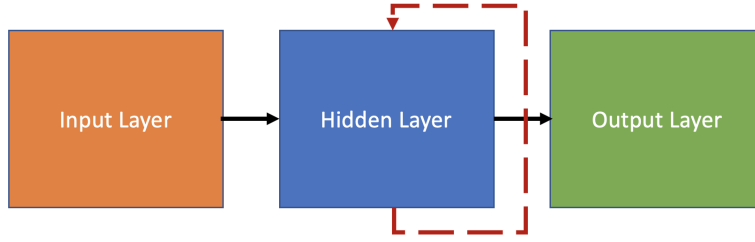


Figure 5.1: Recurrent Neural Network with a loop.

A linear combination (with weights w_x, w_h) of the output from the hidden layer at time $t - \Delta t$ and the input data, $x(t)$, at time t , plus a bias, b_h , are input into the activation. Let $f[\cdot]$ be a desirable activation function. This can be formulated as

$$h(t) = f [w_x x(t) + w_h h(t + \Delta t) + b_h]. \quad (5.1)$$

This produces an output of the hidden layer at time t , $h(t)$, which is input into the activation of the output node along with a bias, b_y , to get an output at time t . The output is then computed by the equation

$$y(t) = f [w_y h(t) + b_y]. \quad (5.2)$$

In this simplest form of a scalar data value and a single hidden layer, the linear combination of the previous layer and data input includes 2 fixed weights and a bias which are input into the activation function of the hidden layer. The output of the hidden layer is multiplied by a fixed weight and added to the bias before being input into the desired activation function to get the RNN prediction at a time $t + \Delta t$. For data that is not 1D (like our 31 probes) those weights become matrices

and biases become vectors. Activation functions are nonlinear in form such as the hyperbolic tangent function, $\tanh(x)$, used in both reservoir computing and LSTM or the sigmoid function, $\sigma(x) = 1/(1 + e^{-x})$, used in the LSTM recurrent step.

5.2.1 The algorithm for reservoir computing

Reservoir computing is a type of RNN. Resources for more details can be found recently in the work of Pathak et. al [71] and originally in the work of Lukoševičius and Jaeger [72]. The algorithm for reservoir computing has two phases: (i) the training phase where the ‘reservoir’ is created from a sufficient pool of data as inputs and (ii) the prediction phase where we close the loop and use the outputs of the reservoir as inputs.

5.2.1.1 Training phase

In this stage, we aim to train our reservoir on a subset of the data that we will call the ‘measurements’, $\mathbf{x}(t)$. These measurements are mapped into the reservoir state space using the $D_r \times D$ matrix \mathbf{W}_{in} , where D_r is reservoir dimensions and D is the dimension of the input, either 31 Hall probes or 24 Gauss coefficients. Likewise, outputs from the reservoir are mapped back to the same state space as the inputs using the function $\mathbf{W}_{out}(\mathbf{h}, \mathbf{P})$, where $\mathbf{h}(t)$ is the reservoir state and \mathbf{P} is a regularization matrix.

The reservoir is updated/trained by iterating through the measurements and combining them with the reservoir states via the fixed random sparse D_r by D_r

matrix \mathbf{A} , giving the new reservoir state and output

$$\mathbf{h}(t + \Delta t) = \tanh[\mathbf{A}\mathbf{h}(t) + \mathbf{W}_{in}\mathbf{x}(t)], \quad (5.3)$$

$$\mathbf{y}(t + \Delta t) = \mathbf{W}_{out}(\mathbf{h}(t + \Delta t), \mathbf{P}). \quad (5.4)$$

The desired effect we want the reservoir to have is that the output $\mathbf{y}(t + \Delta t)$ be the same as the data, $\mathbf{y}_d(t + \Delta t)$. We do this by choosing \mathbf{P} such that during the training period of $-T_p \leq t \leq 0$ the following equation

$$\sum_{-T_p \leq t \leq 0} \|\mathbf{W}_{out}(\mathbf{h}, \mathbf{P}) - \mathbf{y}_d(t + \Delta t)\|^2 + \beta \|\mathbf{P}\|^2 \quad (5.5)$$

is minimized, where $\beta > 0$ is a regularization constant. Considering \mathbf{W}_{out} is taken linearly in \mathbf{P} , this becomes a linear regression problem solved using standard approaches described previously. Below is a schematic for the feed forward reservoir training.

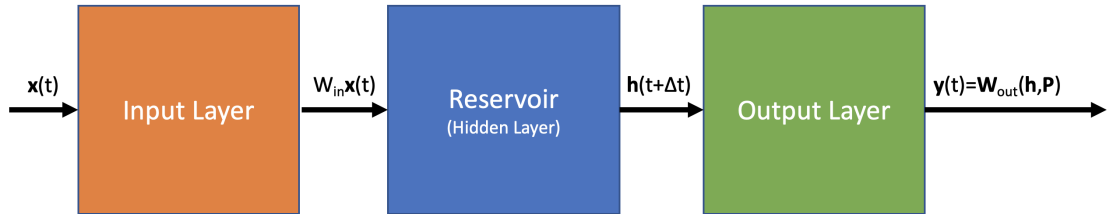


Figure 5.2: The training phase involves training the memory of the reservoir.

5.2.1.2 Prediction phase

Following the training stage is the prediction phase. The approach Jaeger and Haas [73] used is to take the desired output to be equal to the input, $\mathbf{y}_d(t + \Delta t) = \mathbf{x}(t + \Delta t)$. Now at the time of prediction, starting at $t = 0$, the reservoir states are computed by

$$\mathbf{h}(t + \Delta t) = \tanh [\mathbf{A}\mathbf{h}(t) + \mathbf{W}_{in}\mathbf{W}_{out}(\mathbf{h}(t), \mathbf{P})]. \quad (5.6)$$

With this, $\mathbf{y}(t) = \mathbf{W}_{out}(\mathbf{h}(t), \mathbf{P})$ functions as the input measurements, $\mathbf{x}(t)$, in the training stage, except now they act as ‘predictions’ for these values. Eventually, these predictions diverge from the truth as small errors are amplified by chaos whose complexity cannot be captured by the reservoir. In the experiments in the next section, I measure the error between the predictions and truth. Figure 5.3 is a schematic for the reservoir prediction. Notice the red arrow which shows the loop of the RC where the output is input into the network to get the next time step. That is, $\mathbf{x}(t) = \mathbf{y}(t)$ to compute $\mathbf{y}(t + \Delta t)$.

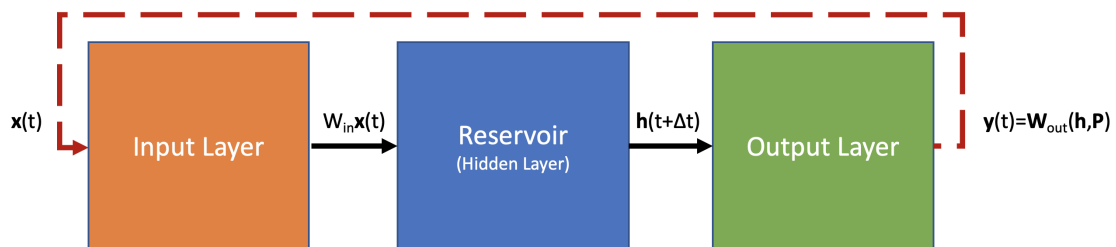


Figure 5.3: The prediction phase of reservoir computing. Note the input measurements, $\mathbf{x}(t)$, have been replaced by $\mathbf{y}(t)$ in order to provide a prediction.

5.2.2 The algorithm for LSTM networks

LSTMs [74] are known for their ability to capture long-term dependencies. This architecture builds on the RNN in a way that allows for long-term memory. Not only does it use long-term memory but it is selective about what has to be remembered. As a reader of this thesis, you likely have not retained every single word you have read so far but recall the context of the former chapters. We will now go over how this is done. Recall in the RNN with each application of the neural net, we linearly combine the input data with information intrinsic to the hidden layer. Therefore, using some of the previous information to then generate the output. The basic feedforward RNN process can be seen in the diagram of Fig. 5.4.

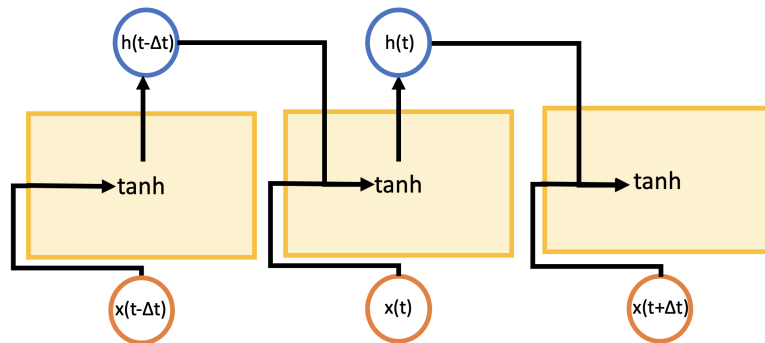


Figure 5.4: Repeating diagram showing recurrent neural network with a single layer.

Figure 5.5 is a diagram of the LSTM network. Instead of the single hidden layer with activation tanh, there are now 4 with σ and tanh.

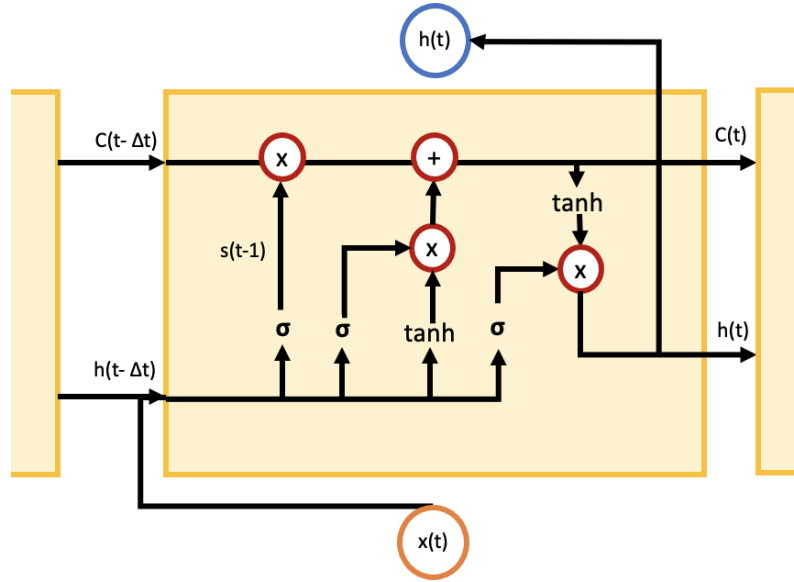


Figure 5.5: Repeating diagram showing long short-term network with four hidden layers indicated by the 4 activation functions of σ and \tanh .

The addition of the horizontal line across the top of the diagram is called the cell state. It passes this information from the hidden layer at time $t - \Delta t$ to time t and so on. During the hidden layer operations the cell state is can modified by pointwise multiplication and addition at the red circle which are called gates. Three gates include a sigmoid layer and a pointwise multiplication operator and manage which information is let through.

The LSTM takes in a linear combination of the previous output of the hidden layer $h(t-\Delta t)$ and new data $x(t)$ plus a bias and passes it through a sigmoid function to be pointwise multiplied by the cell state $C(t - 1)$. So then we have

$$s(t) = \sigma (W_f \cdot [h(t - 1), x(t)] + b_f) . \quad (5.7)$$

The process is indicated by the first vertical arrow with the sigmoid function. The

hidden layer is pointwise multiplied by $C(t - \Delta t)$ and passed along the horizontal line. The next step is to determine the new information added to the cell state by again taking a linear combination of $h(t - \Delta t)$ and new data $x(t)$ plus a bias and passing that through a sigmoid function. Parallel to this, new potential cell state values are computed by taking a linear combination of $h(t - \Delta t)$ and new data $x(t)$ plus a bias and passing that through a tanh function. These two parallel outputs are pointwise multiplied and then summed with the output of the first sigmoid function pointwise multiplied by the cell state $C(t - \Delta t)$ to get cell state $C(t)$. To determine the output, for the third time, the hidden layer $h(t - \Delta t)$ and new data $x(t)$ plus a bias is passed through a sigmoid function. This vector is then pointwise multiplied by $\tanh[C(t)]$ to get $h(t)$. The equations before the pointwise multiplications are,

$$i(t) = \sigma(W_i \cdot [h(t - \Delta t), x(t)] + b_i), \quad (5.8)$$

$$\tilde{C}(t) = \tanh(W_C \cdot [h(t - \Delta t), x(t)] + b_C). \quad (5.9)$$

where Eq. (5.8) is pointwise multiplied by $\tanh[C(t)]$ and Eq. (5.9) is pointwise multiplied by $i(t)$ and the cell state is updated from the former by the pointwise addition,

$$C(t) = s(t) * C(t - \Delta t) + i(t) * \tilde{C}(t). \quad (5.10)$$

Lastly, the output is computed and the hidden layer is updated,

$$y(t) = \sigma (W_y [h(t - \Delta t), x(t)] + b_y) \quad (5.11)$$

$$h(t) = y(t) * \tanh (C(t)) . \quad (5.12)$$

Then the process continues for the next time step with input data $x(t + \Delta t)$.

5.3 Results

The following two section shows the results for each RNN on the experimental run with $Ro = -0.5$, $\Lambda = 0.055$, and $Ek = 3.3 \cdot 10^{-8}$. Sections below show the RNN parameters used in the studies. Figures are also shown to contrast the prediction and the true measurements of both the data and the spherical harmonic coefficients. Error is quantified by the L_2 -norm of the difference between the real data and the RNN prediction.

5.3.1 Reservoir computing

The reservoir was trained on 80% of the magnetic field data from a time series of 671 rotations. It was first normalized, stored as the truth, and then 1.5% error was added before training the reservoir. Table 5.6 shows the parameter set for the following RC prediction results.

Parameter	Value
D_r	3000
average degree	3
λ	0.6
β	10^{-4}

Figure 5.6: Table of the parameters that can be adjusted to optimize the network. D_r is the adjacency matrix \mathbf{A} size and ‘average degree’ refers to the sparsity. The spectral radius of \mathbf{A} is scaled to λ . Lastly, the term β is the regularization parameter.

The first results seen in Figs. 5.7 & 5.8 are produced by training on the measurements from the 31 Hall probes. The second set of results, Figs. 5.9 & 5.10, are produced by training on the 24 Gauss coefficients obtained by using linear regression on the 31 Hall probe data.

5.3.1.1 Hall probe data

Figure 5.7 shows the time series of 31 Hall probes during the time of the prediction phase. The top subplot is the RC prediction, the middle subplot is the true data, and the bottom subplot is the truth subtracted from the predicted data. The L_2 -norm of the displayed error is 252.9.

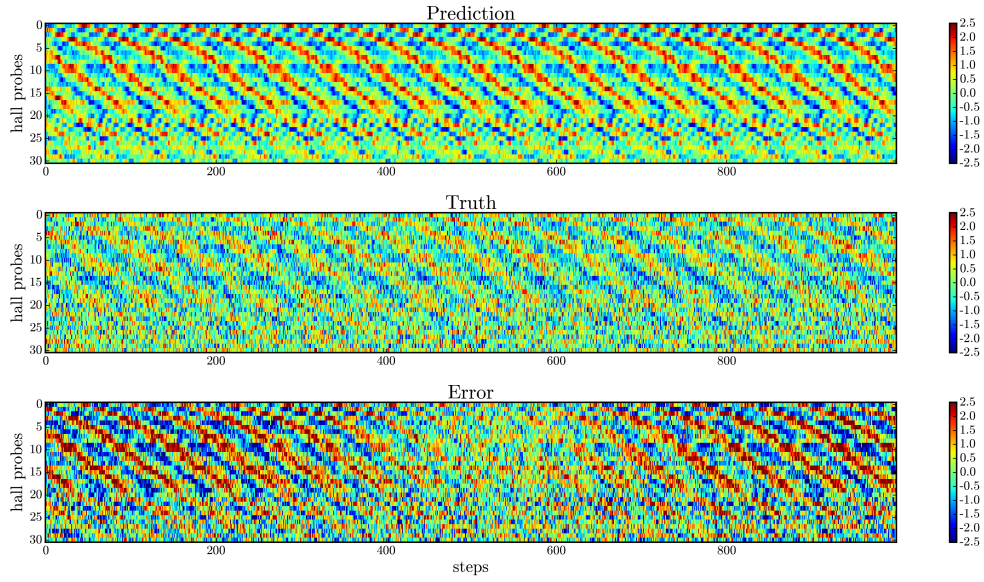


Figure 5.7: Time series in time steps of the normalized r-component of the magnetic field from 31 Hall probes. From top to bottom: (i) reservoir prediction using noised test data, (ii) the true values, and (iii) the difference between the predicted and truth. The norm of the error is 252.9.

We take a closer look at the comparison between the prediction and the true data for a single probe in Fig. 5.8. There appears to be some agreement between 77.8 & 78.2 seconds but outside that interval, the main phases between the experiment and prediction do not overlap.

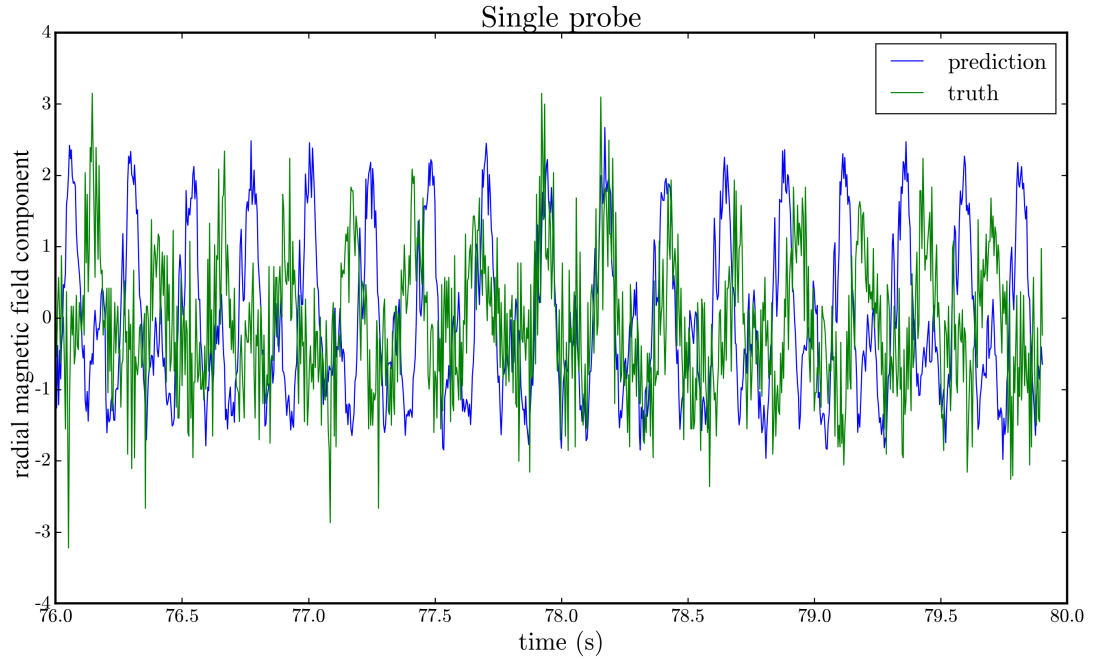


Figure 5.8: Time series of the normalized r-component of the magnetic field from a single hall probe of the reservoir prediction using noised test data (blue) and the true values (green).

5.3.1.2 Gauss coefficient data

Figure 5.7 shows the time series of 24 Gauss coefficient during the time of the prediction phase. The top subplot is the RC prediction, the middle subplot is the true data, and the bottom subplot is the truth subtracted from the predicted data. The L_2 -norm of the displayed error is 204.2.

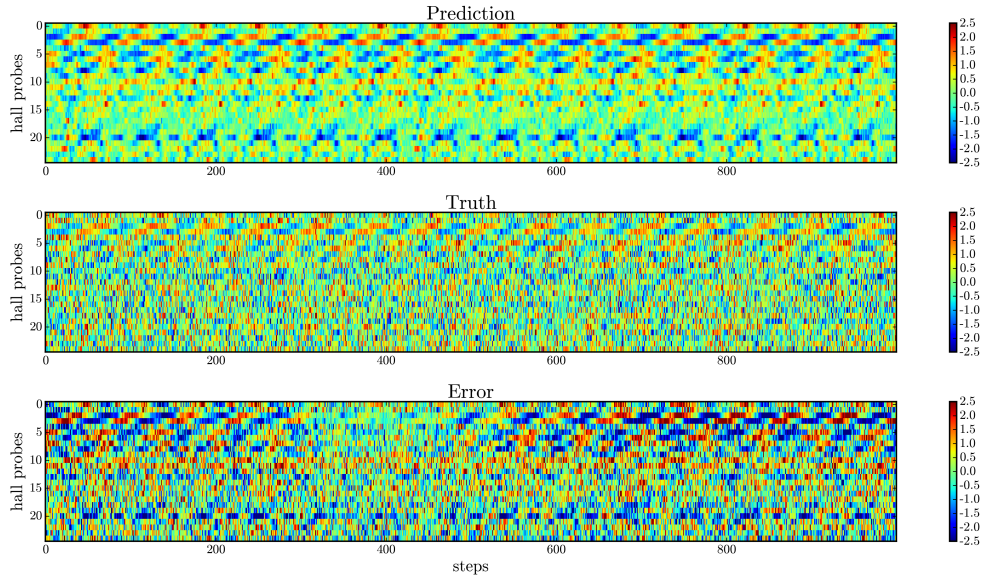


Figure 5.9: Time series of the normalized 24 Gauss coefficients of the magnetic field. From top to bottom: (i) reservoir prediction using noised test data, (ii) the true values, and (iii) the difference between the predicted and truth. The norm of the error is 204.2. The Gauss coefficients are organized from top to bottom grouped by ℓ with m in pairs of cosine and then sine. So $m = 0, 1, 1, 0, 1, 1, 2, 2, 0, 1, 1, 2, 2, 3, 3, 0, 1, 1, 2, 2, 3, 3, 4, 4$ and $\ell = 1, 1, 1, 2, 2, 2, 2, 2, 3, 3, 3, 3, 3, 3, 3, 4, 4, 4, 4, 4, 4, 4, 4$.

In Fig. 5.10 we examine the time series of the Gauss coefficient, $G_1^{1,s}$, to view the contrast between the truth and prediction. Again there appears to be some small window agreement in the middle of the prediction, this time between 77.2 & 77.7 second. Otherwise, the coefficient prediction and truth are not in phase.

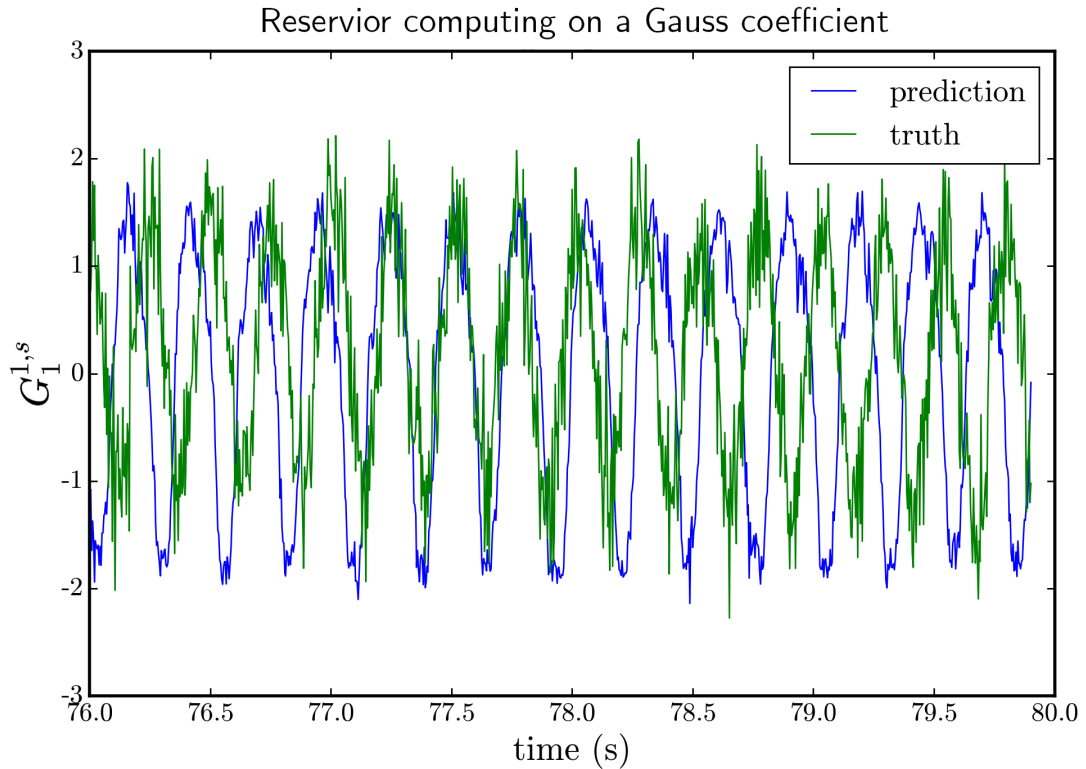


Figure 5.10: Time series of the normalized $m = -1$, $\ell = 1$ of the magnetic field from a single hall probe of the reservoir prediction using noised test data (blue) and the true values (green).

5.3.2 LSTM

In this section we compare the best results of the reservoir computing to the best results of a simple LSTM. This is a simple LSTM built using keras with 50 neurons in the first hidden layer and 31 neurons in the output layer. The training uses the Mean Absolute Error loss function and Adams gradient descent. It is trained for 50 epochs batch sizes of 72.

5.3.2.1 Hall probe data

Figure 5.11 shows the time series of 31 Hall probes during the time of the prediction phase. The top subplot is the LSTM prediction, the middle subplot is the true data, and the bottom subplot is the truth subtracted from the predicted data. The L_2 -norm of the displayed error is 137.6. This is a significant improvement in error from the RC computing error. We can see a good match from the diagonal wave in both the prediction and truth plots.

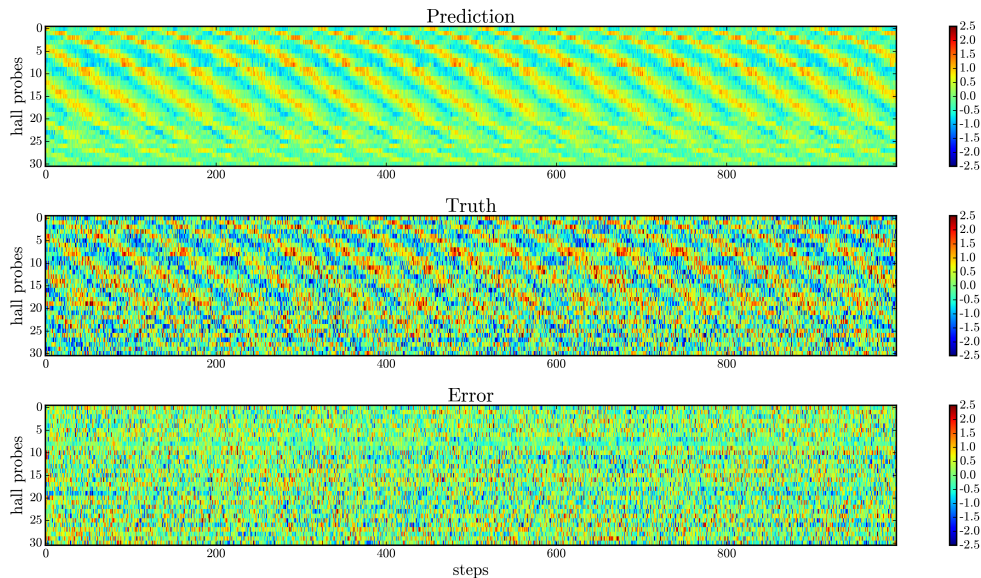


Figure 5.11: Time series of the normalized r-component of the magnetic field from 31 Hall probes. From top to bottom: (i) simple LSTM prediction using noised test data, (ii) the true values, and (iii) the difference between the predicted and truth. The norm of the error is 137.6.

Now for a closer look. Figure 5.12 shows a time series of both the prediction and true radial magnetic field component of a single probe. The prediction captures the main wave but does not resolve the more extreme variations. Thus the variation of the prediction is much smaller than the truth.

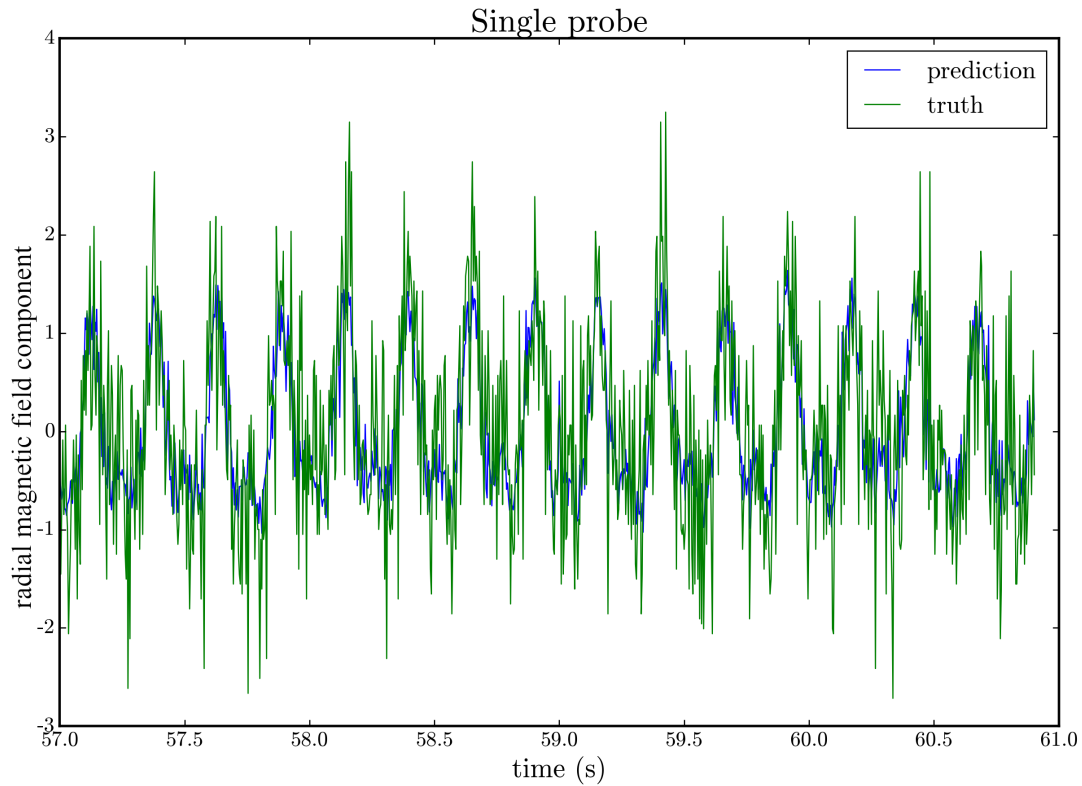


Figure 5.12: Time series of the normalized r-component of the magnetic field from a single hall probe of the LSTM prediction using noised test data (blue) and the true values (green).

5.3.2.2 Gauss coefficient data

Figure 5.13 shows the time series of 24 Gauss coefficient during the time of the prediction phase. The top subplot is the LSTM prediction, the middle subplot is the true data, and the bottom subplot is the truth subtracted from the predicted data. The L_2 -norm of the displayed error is 128.8. Like the RC computing predictions, the LSTM prediction are slightly better on the Gauss coefficients than the Hall probe data.

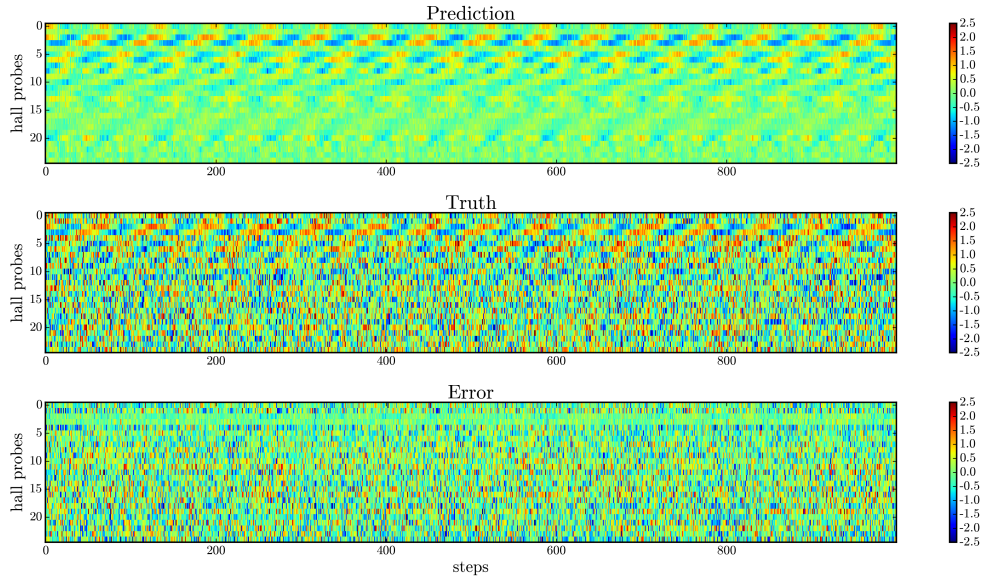


Figure 5.13: Time series of the normalized 24 Gauss coefficients of the magnetic field. From top to bottom: (i) simple LSTM prediction using noised test data, (ii) the true values, and (iii) the difference between the predicted and truth. The norm of the error is 128.8. The Gauss coefficients are organized from top to bottom grouped by ℓ with m in pairs of cosine and then sine. So $m = 0, 1, 1, 0, 1, 1, 2, 2, 0, 1, 1, 2, 2, 3, 3, 0, 1, 1, 2, 2, 3, 3, 4, 4$ and $\ell = 1, 1, 1, 2, 2, 2, 2, 2, 3, 3, 3, 3, 3, 3, 3, 4, 4, 4, 4, 4, 4, 4, 4$.

In Fig. 5.12 we notice that the LSTM prediction does well for the main wave in a single probe time series. In Fig. 5.14 we look at the times series of a larger wave though the Gauss coefficient, $G_1^{1,s}$, to view the contrast between the truth and prediction. The oscillations in the prediction aligns very well with the truth. Compared to Fig. 5.12, the variation of the truth is only slightly larger than the prediction. From this, we can confirm that the LSTM network does well for predicting long-term dependencies like the main wave in the experiment.

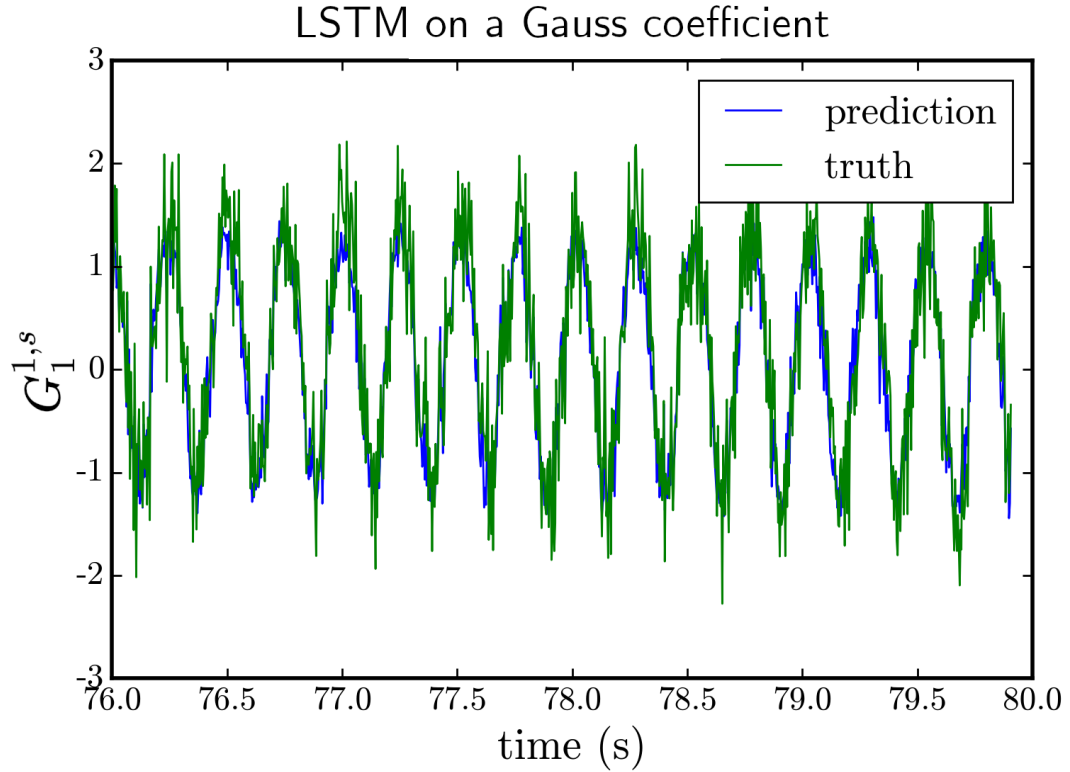


Figure 5.14: Time series of the normalized $m = 1, s, \ell = 1$ of the magnetic field from a single hall probe of the LSTM prediction using noised test data (blue) and the true values (green).

5.4 Conclusion

The LSTM network does the best for predicting the experimental data at least for the larger scale wave. The neural nets do not perform well on small variation, at least for the length of training and testing time windows shown here. This could be because the 31 probes restrict us to perhaps 24 degrees of freedom rather than the 10,000+ degrees intrinsic to the turbulent system. The most successful approach was the simple LSTM which appears to predict the long-term dependencies such as the rotation of the experiment (which is fairly simple to model). Future efforts

to improve RC should be to sample subsets of data from the full set and train the network as keras does in batches. Since the method has some stochasticity in the generation of the initial adjacency matrix and W_{in} , it may be fruitful to research ways to take advantage of that.

More future work includes (i) installing many additional Hall probes or (ii) using synthetic data. In order to answer ‘how many?’ and ‘where to place them?’, I plan to use synthetic data from a numerical model to assess the exact number of measurements needed to allow reliable prediction with NN and data assimilation. Multi-scale hybrid methods might be suitable to separate the small scales from the main rotation in the sphere. Right now, because of the low-dimensionality of the data, it seems everything small scale is treated as noise compared to the rotation.

Provided enough prediction data, further analysis could be done from here by looking at the spectra of the prediction to see if the the magneto Coriolis modes appear or if its just the main rotation that the NNs pick up. I would have also like to compare the spherical harmonic prediction projected back onto the hall probe locations. Though the experiment has few spatial measurements, it does have the ability to capture sufficient of data in time relative to its intrinsic timescales. Something that we will be waiting for with Earth for tens of thousands of years.

Chapter 6: Conclusions and potential future work

6.1 Conclusion

This thesis introduces the significance of the geodynamo and the difficulty studying it due to the inaccessibility of measurements and limited data in time. I then motivate the advantages of studying the mechanical 3m over the geodynamo. Still, experimental data of the velocity field and internal magnetic fields elude us as it is dangerous to place measurements inside the experiment. The simulations provide a mean to capture full 3D fields. In Chapter 2, we explore the behavior in three different set of control parameters that belong to two different dynamical states: the inertial mode state and high torque state. For the first time, we can see how the fields fluctuate and the movement of the bulk flow inside the 3m experiment. The radial correlation simulation studies show the correlations between poloidal magnetic field on the radial shell where probes would reside and poloidal magnetic fields in the interior. Same with correlations between poloidal magnetic field of probe shell and the toroidal velocity field in the interior. For the $Ro = -0.5$ in particular, there are strong correlations of the poloidal probe shell for $m = 1$ with both the poloidal magnetic field and toroidal velocity field. For larger $|Ro|$ the correlations are weak with depth. In the high torque case, the correlations in the magnetic

field vs. magnetic field appear only subtly for $r < 0.75r_o$. The magnetic field vs. velocity field barely correlates at $0.95r_o$. Therefore, if the surface measurement can be representative of the internal workings at least for shallow measurements near the surface and low $|Ro|$ for measurements at greater depth.

In chapter 3, we aim to match the experiment and simulations using their PCA analysis. The basis of spherical harmonics should be detected by the 31 probes at least to $\ell_{max} = 4$. By viewing the spatial eigenvectors of simulations, we can see $\ell_{max} = 4$ is not large enough to capture the large scale variation in the magnetic field measured at the surface. We can also note that the experiment is very noisy. In the spectra of the dominant temporal eigenvector of $Ro = -0.5$, any frequency larger than $f/f_o = 2.5$ in the experiment is noise. Also, for $Ro = -0.5$, we see the experiment aligns with a combination of spherical harmonic basis functions that encourage the placement of new probes in a meridian line. The experimental and simulation match best in main six eigenvectors for $Ro = 1.75$.

In chapter 4, several new probes configurations were tested on simulation data using the raw data and comparing it with data recreated from Gauss coefficients. These studies used several measures including the Wasserstein distance. From our assessment, the best new probe locations would be to place them on two new meridian arrays.

In chapter 5, we test two types of RNN on one set of experimental data. The most successful approach was the simple LSTM but that predicted well the rotation of the experiment. Due to the high levels of noise found in chapter 3, it is likely the RC have difficulty training and distinguishing between noise and small scale

spherical harmonics from the MHD flow.

6.2 Potential work

At the beginning of this thesis, I mentioned there are two possible external magnetic field setups: dipolar and quadrupolar. I choose the quadrupolar magnetic field because I found it interesting. The simulations should also be tested on the dipole external magnetic field configuration. Dipolar simulations would be more geodynamo-like.

6.2.1 Coupled PCA

In Chapter 3, I mentioned the positive aspects of coupled PCA. In Kutzbach's work [61], he was able to explain 80% of the variance with 6 eigenvectors from coupled PCA with for monthly mean sea-level pressure and surface temperature whereas the same amount of variance was explain by a total of 8 eigenvectors of the PCA of the two field separately. More information could be ascertained from a PCA of the coupled velocity and magnetic fields but then non-standard version of PCA must be used to the large amounts of data. Techniques such as a randomized version of the block Lanczos method can be used for performing PCA on large data sets [75].

6.2.2 Data assimilation

Data assimilation has been implemented on the geodynamo model [29, 30, 76, 77, 78] Based on prior geodynamo Data Assimilation studies [30, 78] an Observation Simulation System Experiment (OSSE):

1. Compute the e-folding time [79] by observing the exponential growth of noisy Gaussian ensemble members. Use this to estimate assimilation window.
2. Take snapshots of a simulation run at times greater than the e -folding time to use as the initial ensemble.
3. Generate synthetic observations for a window of about 2 e -folding times.
4. Assimilate observations.

The measure of e -folding time of the exponential growth, τ_e determines the rate single dominant error growth rate $\lambda = \tau_e^{-1}$. Hulot et al. found that this growth rate varies depending on each set of control parameters Ek , Pm , and those associated with the geodynamo thermal properties [79]. I attempted to capture the e -folding time by adding 1% of the magnetic field rms value to the magnetic field for parameters $Ek = 3 \cdot 10^{-6}$, $Ro = -0.5$, and $Le = 0.013$. Any larger added error caused bad spectral convergence. Then I computed the trace of the covariance of these ensembles over time. To get the τ_e , I fit the time and traces of the covariance to the exponential curve: $tr(Covariance) = e^{t/\tau_e}$. My attempts for these control parameters didn't produce a spread that increased in time. Part of what might have

gone differently with the 3m simulations vs. geodynamo simulations is the difference in parameters (see Table 1.3). I believe the forcing terms of the experiment (driving shear from the shell, the applied external field) the simulations converge to a statistic equilibrium and there is no exponential growth from which to calculate the e -folding time.

For someone who wants to try it, I can provide initial conditions of my runs. I suggest running from control parameters in the high torque state. First, make sure you have plenty of storage space since you will need multiple ensembles and field outputs for each to compute the e -folding time. Next, initialize the run with more radial shells and increase ℓ_{max} and m_{max} . Adding error can cause poor spectra convergence so a finer resolution will help with spectral convergence. Next at 1% (or even 0.1%) of the rms error a shell or a point in the magnetic field. Run over several rotation times, saving sufficiently many outputs to determine the e -folding time. Ideally, there will be an ensemble spread and you will be able to determine the dynamically timescales from the e -folding time which can be used to determine how often observations are needed and the size of the assimilation window.

Another important aspect, to study prior to implementing data assimilation is localization. Localization reduces the effects of spurious correlations in the data assimilation weather modeling framework (i.e. weather in Maryland is not affected by weather in Russia, so separate local analysis is preferable). In the work of Sanchez et al. [30] which inspired correlation studies, they analyze a time series of a geodynamo model. They look at localization in terms of the spectral coefficients as done in Sec. 2.6 as well as in (r, θ, φ) -space. In the end they concluded that localization

in spectral space is preferable to real space. A similar localization study should be carried out in order to strategically localize and implement a data assimilation technique like the local ensemble transform Kalman filter [80].

6.2.3 Machine Learning

There are a wealth of new machine learning techniques and variations on LSTMs. Preprocessing of the data to remove the largest wave could improve on LSTMs prediction of the smaller features. More complexity in hidden layers might improve on the prediction of the probes in time. Also, with the right amount of storage to collect the simulation data, a combination of training on the simulation data and testing on the real experimental data could be implemented. One advantage the 3D data has is it can help us predict into the interior magnetic and velocity field from the exterior where the radial probes are setup. Synthetic data could be created from the simulation by extracting the magnetic field at various depths and calculating the field outside the domain at the probe radius. Noise would be added to represent the noise intrinsic to the experiment. A convolutional neural network (CNN) could be trained and verified on the synthetic data and then tested on the experimental data. In the recent paper of Bolton and Zanna [81], a CNN was trained to predict subsurface stream function data from surface stream function data. Lastly, an ambitious thing to try would be to combine the prediction power of LSTM with the CNN abilities to reveal subsurface flows to predict a 3D magnetic field and velocity field in time.

Bibliography

- [1] Emmanuel Dormy. The origin of the earth’s magnetic field: fundamental or environmental research? *Europhysics news*, 37(2):22–25, 2006.
- [2] Francis Birch. Elasticity and constitution of the earth’s interior. *Journal of Geophysical Research*, 57(2):227–286, 1952.
- [3] William F McDonough and S-S Sun. The composition of the earth. *Chemical geology*, 120(3-4):223–253, 1995.
- [4] Joseph G O’Rourke and David J Stevenson. Powering earths dynamo with magnesium precipitation from the core. *Nature*, 529(7586):387–389, 2016.
- [5] Jessica CE Irving, Sanne Cottaar, and Vedran Lekić. Seismically determined elastic parameters for earths outer core. *Science advances*, 4(6):eaar2538, 2018.
- [6] Renaud Deguen and Philippe Cardin. Thermochemical convection in earth s inner core. *Geophysical Journal International*, 187(3):1101–1118, 2011.
- [7] Geoffrey Ingram Taylor. The motion of a sphere in a rotating liquid. *Proceedings of the Royal Society of London. Series A, Containing Papers of a Mathematical and Physical Character*, 102(715):180–189, 1922.
- [8] Sabrina Sanchez, Alexandre Fournier, Katia J Pinheiro, and Julien Aubert. A mean-field babcock-leighton solar dynamo model with long-term variability. *Anais da Academia Brasileira de Ciências*, 86(1):11–26, 2014.
- [9] Walter M Elsasser. Induction effects in terrestrial magnetism part i. theory. *Physical Review*, 69(3-4):106, 1946.
- [10] Walter M Elsasser. Induction effects in terrestrial magnetism part ii. the secular variation. *Physical Review*, 70(3-4):202, 1946.
- [11] George Keith Batchelor. On the spontaneous magnetic field in a conducting liquid in turbulent motion. *Proceedings of the Royal Society of London. Series A. Mathematical and Physical Sciences*, 201(1066):405–416, 1950.

- [12] Edward Bullard and H Gellman. Homogeneous dynamos and terrestrial magnetism. *Philosophical Transactions of the Royal Society of London. Series A, Mathematical and Physical Sciences*, pages 213–278, 1954.
- [13] Gary A Glatzmaiers and Paul H Roberts. A three-dimensional self-consistent computer simulation of a geomagnetic field reversal. *Nature*, 377(6546):203–209, 1995.
- [14] Akira Kageyama, Tetsuya Sato, and Complexity Simulation Groupa). Computer simulation of a magnetohydrodynamic dynamo. ii. *Physics of Plasmas*, 2(5):1421–1431, 1995.
- [15] Johannes Wicht and Sabrina Sanchez. Advances in geodynamo modelling. *Geophysical & Astrophysical Fluid Dynamics*, 113(1-2):2–50, 2019.
- [16] Gary A Glatzmaier. Numerical simulations of stellar convective dynamos. i. the model and method. *Journal of Computational Physics*, 55(3):461–484, 1984.
- [17] Thomas C. Clune, JR Elliott, MS Miesch, J Toomre, and Gary A. Glatzmaier. Computational aspects of a code to study rotating turbulent convection in spherical shells. *Parallel Computing*, 25(4):361–380, 1999.
- [18] U. Christensen and J. Wicht. *Numerical dynamo simulations*.
- [19] Hiroaki Matsui, Eric Heien, Julien Aubert, Jonathan M Aurnou, Margaret Avery, Ben Brown, Bruce A Buffett, Friedrich Busse, Ulrich R Christensen, Christopher J Davies, et al. Performance benchmarks for a next generation numerical dynamo model. *Geochemistry, Geophysics, Geosystems*, 17(5):1586–1607, 2016.
- [20] Alan Thomson. Geomagnetism review 2019. 2020.
- [21] INTERMAGNET. Magnetic observatories (map). <https://www.intermagnet.org/imos/imomap-eng.php>, 2019. Accessed: 2021-09-01.
- [22] Alexandre Fournier, Julien Aubert, and Erwan Thébault. A candidate secular variation model for igrf-12 based on swarm data and inverse geodynamo modelling. *Earth, Planets and Space*, 67(1):1–17, 2015.
- [23] Adam M Dziewonski and Don L Anderson. Preliminary reference earth model. *Physics of the earth and planetary interiors*, 25(4):297–356, 1981.
- [24] Catherine G Constable and Steven C Constable. Satellite magnetic field measurements: applications in studying the deep earth. *The State of the Planet: Frontiers and Challenges in Geophysics*, 150:147–159, 2004.
- [25] John A Tarduno, Rory D Cottrell, William J Davis, Francis Nimmo, and Richard K Bono. A hadean to paleoarchean geodynamo recorded by single zircon crystals. *Science*, 349(6247):521–524, 2015.

- [26] Monika Korte and CG Constable. Spatial and temporal resolution of millennial scale geomagnetic field models. *Advances in Space Research*, 41(1):57–69, 2008.
- [27] S Sanchez, A Fournier, J Aubert, E Cosme, and Y Gallet. Modelling the archaeomagnetic field under spatial constraints from dynamo simulations: a resolution analysis. *Geophysical Supplements to the Monthly Notices of the Royal Astronomical Society*, 207(2):983–1002, 2016.
- [28] Patrick Alken, Erwan Thébault, Ciarán D Beggan, H Amit, J Aubert, J Baerenzung, TN Bondar, WJ Brown, S Califf, A Chambodut, et al. International geomagnetic reference field: the thirteenth generation. *Earth, Planets and Space*, 73(1):1–25, 2021.
- [29] Weijia Kuang, Zigang Wei, Richard Holme, and Andrew Tangborn. Prediction of geomagnetic field with data assimilation: a candidate secular variation model for igrf-11. *Earth, planets and space*, 62(10):775–785, 2010.
- [30] Sabrina Sanchez, Johannes Wicht, and Julien Bärenzung. Predictions of the geomagnetic secular variation based on the ensemble sequential assimilation of geomagnetic field models by dynamo simulations. *Earth, Planets and Space*, 72(1):1–20, 2020.
- [31] Daniel S Zimmerman, Santiago Andrés Triana, Henri-Claude Nataf, and Daniel P Lathrop. A turbulent, high magnetic reynolds number experimental model of earth’s core. *Journal of Geophysical Research: Solid Earth*, 119(6):4538–4557, 2014.
- [32] Matthew M Adams, Douglas R Stone, Daniel S Zimmerman, and Daniel P Lathrop. Liquid sodium models of the earth’s core. *Progress in Earth and Planetary Science*, 2(1):29, 2015.
- [33] Nicholas L Peffley, AB Cawthorne, and Daniel P Lathrop. Toward a self-generating magnetic dynamo: The role of turbulence. *Physical Review E*, 61(5):5287, 2000.
- [34] Woodrow L Shew and Daniel P Lathrop. Liquid sodium model of geophysical core convection. *Physics of the Earth and Planetary Interiors*, 153(1-3):136–149, 2005.
- [35] Daniel Brito, Thierry Alboussiere, Philippe Cardin, Nadège Gagnière, Dominique Jault, Patrick La Rizza, J-P Masson, H-C Nataf, and Denys Schmitt. Zonal shear and super-rotation in a magnetized spherical couette-flow experiment. *Physical Review E*, 83(6):066310, 2011.
- [36] PA Gilman. Dynamically consistent nonlinear dynamos driven by convection in a rotating spherical shell. ii-dynamos with cycles and strong feedbacks. *The Astrophysical Journal Supplement Series*, 53:243–268, 1983.

- [37] H Matsui, M Adams, D Kelley, SA Triana, D Zimmerman, BA Buffett, and DP Lathrop. Numerical and experimental investigation of shear-driven inertial oscillations in an earth-like geometry. *Physics of the Earth and Planetary Interiors*, 188(3-4):194–202, 2011.
- [38] Hiroaki Matsui and Hiroshi Okuda. Mhd dynamo simulation using the geofem platform verification by the dynamo benchmark test. *International Journal of Computational Fluid Dynamics*, 19(1):15–22.
- [39] Rainer Hollerbach, Elisabeth Canet, and Alexandre Fournier. Spherical couette flow in a dipolar magnetic field. *European Journal of Mechanics-B/Fluids*, 26(6):729–737, 2007.
- [40] Aldo Figueroa, Nathanaël Schaeffer, H-C Nataf, and Denys Schmitt. Modes and instabilities in magnetized spherical couette flow. *Journal of Fluid Mechanics*, 716:445–469, 2013.
- [41] Simon Cabanes, Nathanaël Schaeffer, and Henri-Claude Nataf. Turbulence reduces magnetic diffusivity in a liquid sodium experiment. *Physical review letters*, 113(18):184501, 2014.
- [42] EJ Kaplan, H-C Nataf, and N Schaeffer. Dynamic domains of the derviche tourneur sodium experiment: Simulations of a spherical magnetized couette flow. *Physical Review Fluids*, 3(3):034608, 2018.
- [43] Rainer Hollerbach. Magnetohydrodynamic ekman and stewartson layers in a rotating spherical shell. *Proceedings of the Royal Society of London. Series A: Mathematical and Physical Sciences*, 444(1921):333–346, 1994.
- [44] Emmanuel Dormy, Philippe Cardin, and Dominique Jault. Mhd flow in a slightly differentially rotating spherical shell, with conducting inner core, in a dipolar magnetic field. *Earth and Planetary Science Letters*, 160(1-2):15–30, 1998.
- [45] A Tilgner. Spectral methods for the simulation of incompressible flows in spherical shells. *International journal for numerical methods in fluids*, 30(6):713–724, 1999.
- [46] A Tilgner. Magnetohydrodynamic flow in precessing spherical shells. *Journal of Fluid Mechanics*, 379:303–318, 1999.
- [47] Johannes Wicht. Flow instabilities in the wide-gap spherical couette system. *Journal of fluid mechanics*, 738:184, 2014.
- [48] K Finke and A Tilgner. Simulations of the kinematic dynamo onset of spherical couette flows with smooth and rough boundaries. *Physical Review E*, 86(1):016310, 2012.

- [49] Anthony Robert Mautino. *Inverse Spectral Methods in Acoustic Normal Mode Velocimetry of High Reynolds Number Spherical Couette Flows*. PhD thesis, 2016.
- [50] Daniel S Zimmerman, Santiago Andrés Triana, and Daniel P Lathrop. Bistability in turbulent, rotating spherical couette flow. *Physics of Fluids*, 23(6):065104, 2011.
- [51] Nathanaël Schaeffer, Dominique Jault, H-C Nataf, and Alexandre Fournier. Turbulent geodynamo simulations: a leap towards earths core. *Geophysical Journal International*, 211(1):1–29, 2017.
- [52] Nathanaël Schaeffer. XSHELLS. <https://nschaeff.bitbucket.io/xshells/>, 2018.
- [53] Nathanaël Schaeffer. Efficient spherical harmonic transforms aimed at pseudospectral numerical simulations. *Geochemistry, Geophysics, Geosystems*, 14(3):751–758, 2013.
- [54] John David Jackson. *Classical electrodynamics* third edition. 1962.
- [55] Ikuko Fujii and Adam Schultz. The 3d electromagnetic response of the earth to ring current and auroral oval excitation. *Geophysical Journal International*, 151(3):689–709, 2002.
- [56] Harold Hotelling. Analysis of a complex of statistical variables into principal components. *Journal of educational psychology*, 24(6):417, 1933.
- [57] Ian T Jolliffe. Principal components in regression analysis. In *Principal component analysis*, pages 129–155. Springer, 1986.
- [58] Jeroen Ritsema and Vedran Lekić. Heterogeneity of seismic wave velocity in earth’s mantle. *Annual Review of Earth and Planetary Sciences*, 48:377–401, 2020.
- [59] Edward N Lorenz. Empirical orthogonal functions and statistical weather prediction. 1956.
- [60] RM White, DS Cooley, RC Derby, and FA Seaver. The development of efficient linear statistical operators for the prediction of sea-level pressure. *Journal of Atmospheric Sciences*, 15(5):426–434, 1958.
- [61] John E Kutzbach. Empirical eigenvectors of sea-level pressure, surface temperature and precipitation complexes over north america. *Journal of Applied Meteorology and Climatology*, 6(5):791–802, 1967.
- [62] Solomon Kullback and Richard A Leibler. On information and sufficiency. *The annals of mathematical statistics*, 22(1):79–86, 1951.

- [63] Solomon Kullback. *Information theory and statistics*. Courier Corporation, 1997.
- [64] Jianhua Lin. Divergence measures based on the shannon entropy. *IEEE Transactions on Information theory*, 37(1):145–151, 1991.
- [65] Soheil Kolouri, Phillip E Pope, Charles E Martin, and Gustavo K Rohde. Sliced wasserstein auto-encoders. In *International Conference on Learning Representations*, 2018.
- [66] Alison L Gibbs and Francis Edward Su. On choosing and bounding probability metrics. *International statistical review*, 70(3):419–435, 2002.
- [67] Leonid Wasserstein. 5(3):64–73, 1969.
- [68] SS Vallender. Calculation of the wasserstein distance between probability distributions on the line. *Theory of Probability & Its Applications*, 18(4):784–786, 1974.
- [69] L.V. Kantorovich and G.Sh Rubinshteĭn. On a space of completely additive functions. *Vestnik Leningradskogo Universiteta, Matematika, Mekhanika, Astronomija*, 13:52–59, 01 1958.
- [70] Yossi Rubner, Carlo Tomasi, and Leonidas J Guibas. The earth mover’s distance as a metric for image retrieval. *International journal of computer vision*, 40(2):99–121, 2000.
- [71] Jaideep Pathak, Zhixin Lu, Brian R Hunt, Michelle Girvan, and Edward Ott. Using Machine Learning to Replicate Chaotic Attractors and Calculate Lyapunov Exponents from Data. *Chaos: An Interdisciplinary Journal of Nonlinear Science*, 27(12):121102, 2017.
- [72] Mantas Lukoševičius and Herbert Jaeger. Reservoir Computing Approaches to Recurrent Neural Network Training. *Computer Science Review*, 3(3):127–149, 2009.
- [73] Herbert Jaeger and Harald Haas. Harnessing Nonlinearity: Predicting Chaotic Systems and Saving Energy in Wireless Communication. *science*, 304(5667):78–80, 2004.
- [74] Sepp Hochreiter and Jürgen Schmidhuber. Long short-term memory. *Neural computation*, 9(8):1735–1780, 1997.
- [75] Nathan Halko, Per-Gunnar Martinsson, Yoel Shkolnisky, and Mark Tygert. An algorithm for the principal component analysis of large data sets. *SIAM Journal on Scientific computing*, 33(5):2580–2594, 2011.

- [76] Alexandre Fournier, Céline Eymin, and Thierry Alboussière. A case for variational geomagnetic data assimilation: insights from a one-dimensional, nonlinear, and sparsely observed mhd system. *Nonlinear processes in Geophysics*, 14(2):163–180, 2007.
- [77] Weijia Kuang, Andrew Tangborn, Weiyuan Jiang, Don Liu, Zhibin Sun, Jeremy Bloxham, and Zigang Wei. Mosst-das: the first generation geomagnetic data assimilation framework. *Commun. Comput. Phys*, 3(1):85–108, 2008.
- [78] S Sanchez, Johannes Wicht, J Bärenzung, and M Holschneider. Sequential assimilation of geomagnetic observations: perspectives for the reconstruction and prediction of core dynamics. *Geophysical Journal International*, 217(2):1434–1450, 2019.
- [79] G Hulot, F Lhuillier, and J Aubert. Earth’s dynamo limit of predictability. *Geophysical Research Letters*, 37(6), 2010.
- [80] Brian R Hunt, Eric J Kostelich, and Istvan Szunyogh. Efficient data assimilation for spatiotemporal chaos: A local ensemble transform kalman filter. *Physica D: Nonlinear Phenomena*, 230(1):112–126, 2007.
- [81] Thomas Bolton and Laure Zanna. Applications of deep learning to ocean data inference and subgrid parameterization. *Journal of Advances in Modeling Earth Systems*, 11(1):376–399, 2019.